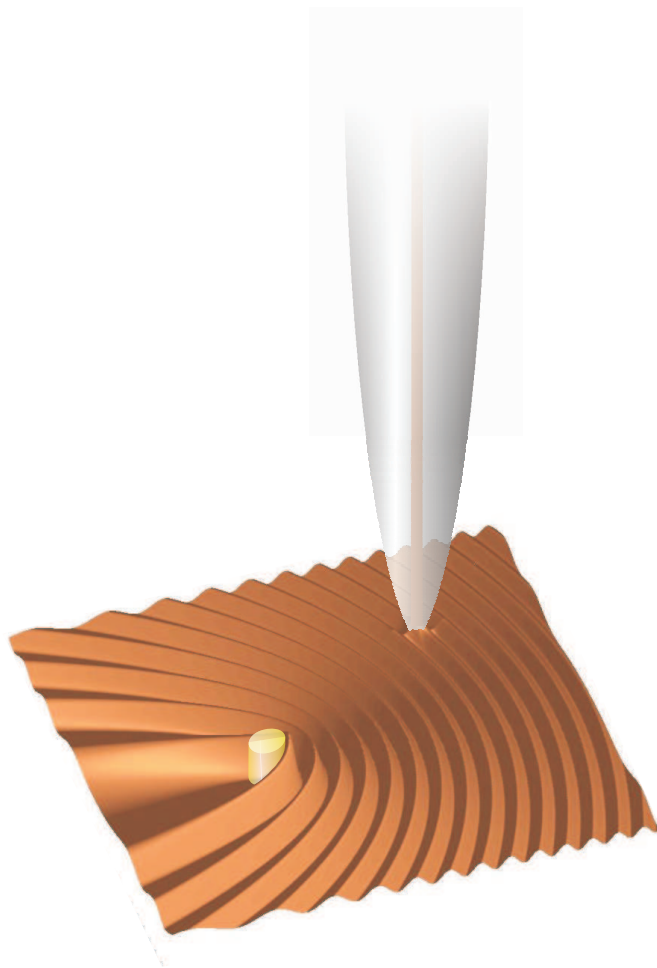


**Scanning Near-Field Microscopy of Surface
Plasmon Polariton Scattering in Structures
of Gold Nano-Particles**



Title: Scanning Near-Field Microscopy of Surface Plasmon Polariton Scattering in Structures of Gold Nano-Particles

Project Period: 2nd of February - 9th of June, 2004

Semester:

F10

Student:

Carsten Marquart

Supervisor:

Sergey Bozhevolnyi

Number of Copies: 5

Number of Pages: 88

Appendices: 5

SYNOPSIS:

Based on a scanning near-field optical microscopy apparatus, elastic scattering of surface plasmon polaritons, being excited via the Kretschmann coupling scheme, is investigated. The excitation sources include focused and parallel light from a He-Ne and a Ti:Sapphire (725 to 890nm) laser.

Prior to scattering investigations, the surface plasmon polariton intensity profile from a focused excitation beam is studied in detail and its behavior is modelled.

The samples consist of 45 to 80nm thick silver and gold films. The gold films contain deposited gold nano-particles arranged as either single scatterers, line arrays or periodic surface plasmon band gap structures with straight channels of missing particles.

Modelling of the field intensity distribution is made by means of a multiple scattering dipole approach treating the individual particles as point-like scatterers.

PREFACE

This report has been composed at the Institute of Physics at Aalborg University in the F10-period from the 2nd of February to the 9th of June, 2004. It is the third and concluding report of the *The Marquart's Microscopy Series*, including preceding reports named *Second Harmonic Scanning Optical Microscopy of Poly Para-Phenylene Nanofibers*, spring 2003 and *Scanning Near-Field Microscopy of Surface Plasmon Polaritons*, fall 2004, which was worked out in collaboration with Stud. Ing. Claus Kejser. This present project is a direct continuation of the second report, and some of the theory described during that time is incorporated into this report in the form of appendices.

In each chapter, references to the applied literature, possibly including the relevant pages, are listed. Specific references are usually stated within the chapter. The references and possible corresponding pages are denoted by surrounding brackets, such as [35][pages 21 to 32]. Vectors are denoted by bold format, for instance \mathbf{E} . Matrices are indicated by a double arrow, as \overleftrightarrow{M} . References to equations are shown with surrounding parentheses, for instance (1.3). Any simulations shown in this report have been performed using the programming tool Matlab 6,5.

Thanks are dedicated to Prof. Dr. Sergey I. Bozhevolnyi, Aalborg Universitet, for immediate and relevant supervising in times of need and to Ph.D. Valentyn Volkov, Aalborg Universitet, for significant contribution to the mounting of experimental arrangements. Additional thanks are directed to Ph.D.-student Peter Kjær Kristensen and laboratory technician Kim Houtved Jensen, Aalborg Universitet, for evaporation of silver films, to Dr. Carsten Henkel, Universität Potsdam, for inspiring comments on optimization of computation procedures and to Stud. Ing. Claus Kejser, Aalborg University, for relevant discussions on modelling of light propagation in photonic band gap structures. Finally, the author greatly appreciate the proofreading and support by Annette Høj Nielsen.

Carsten Marquart

CONTENTS

1	Introduction	7
2	Focusing	15
2.1	Modelling	16
2.2	Beam Waist Dispersion and Propagation Lengths	19
2.3	Oscillations	21
3	Elastic Scattering	27
3.1	Self-consistent Model	27
3.2	Micro-optical Devices	32
3.3	Simple Structures	36
3.4	Surface Plasmon Polariton Band Gap Structures	39
3.4.1	Optimization of Computation	39
3.4.2	Triangular Structures	42
3.4.3	Quadratic Structures	47
3.4.4	Waveguide Structures	53
4	Conclusion	57
A	Surface Plasmon Polaritons	59
B	Evanescent Fields	67
C	Excitation of Surface Plasmon Polaritons	71
D	Physics of Attenuated Total Reflection	75
E	Reflectivity From a Three Layer System	83

CHAPTER 1

INTRODUCTION

Surface plasmon polaritons (SPPs) are, as the name partly indicates, electromagnetic excitations coupled to electron plasma oscillations, which have the unique property of propagating along a metal-dielectric interface as quasi-two-dimensional interface waves. Due to their electromagnetic nature, SPPs can reflect, diffract and interfere [1].

This offers new technological perspectives in a broad range of branches. For instance, SPPs can be applied to efficiently channel light using scatterers in subwavelength structures [2, 3, 4]. Eventually, this could lead to miniaturized photonic circuits with length scales much smaller than currently achievable.

Another branch which makes use of the properties of SPPs is the field of bio-photonics. By using SPPs to concentrate light in subwavelength structures, such as a metallic beak, it is possible to locally create a massive signal enhancement. This may be used to detect vibrational modes of a single molecule[5], also known as surface enhanced Raman spectroscopy.

Other areas of science, in which SPPs are of interest include magneto-optic data storage, microscopy and solar cells. [6]

Fundamentals of Surface Plasmon Polaritons

The following briefly summarizes the important properties of SPPs. Appendix A can be consulted for a far more detailed description. In addition, evanescent fields, associated with SPPs, are shortly studied in general, see appendix B.

A preliminary observation which must be made prior to the description of the nature of SPPs, is to consider the electrons of the host material, a conductor. The conducting electrons are, to a certain extent, considered to be capable of moving freely within the material. In the case of a local influence on the electrons, longitudinal oscillations of electrons, plasma oscillations, are being created. A plasmon is a quantum of the plasma oscillation. The electron plasma frequency at metal-air interface lies in the optical range and has the relation

$$\omega_{sp} = \frac{\omega_p}{\sqrt{2}}, \quad (1.1)$$

where ω_p is the natural frequency of bulk electron plasma oscillations.

Surface plasmons are collective excitations of the electrons at the interface between a conductor and an insulator. This leads to oscillatory longitudinal motion of the electrons along the x-direction with a dispersion relation β , see figure 1.1A for an illustration of this. An evanescent field in the z-direction is produced by the electrons, whose alternating surface charge densities build up the field. The evanescent field distribution across the

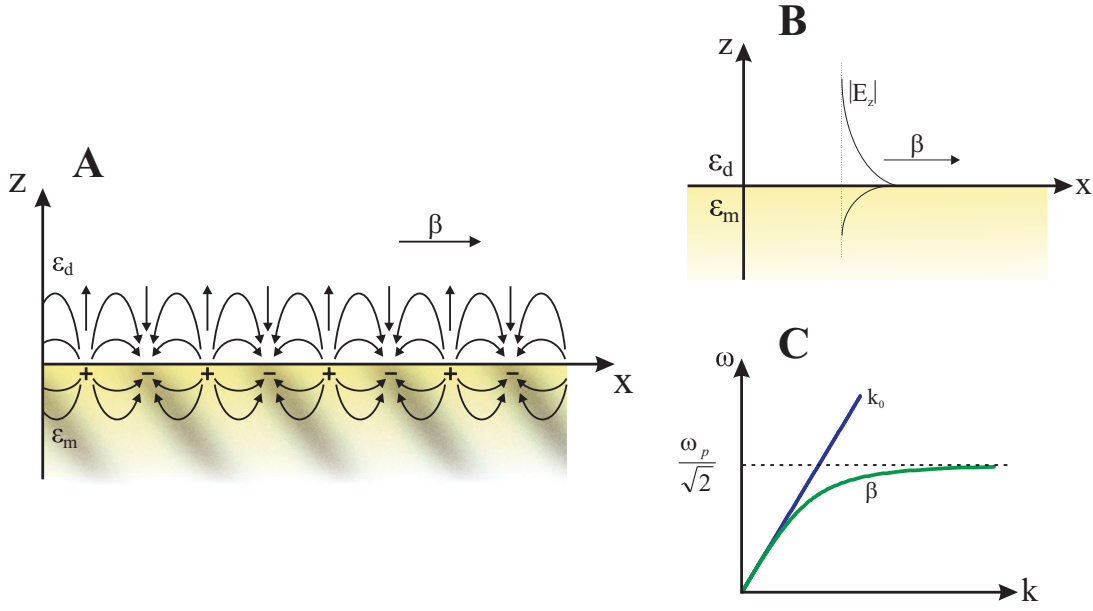


Figure 1.1: *A: longitudinal charge fluctuations caused by collective excitations of electrons at the interface between two semi-infinite media of metal and dielectric. B: the evanescent fields constituted by the propagating SPPs decay exponentially into both media. C: the non intersecting dispersion lines for vacuum (blue line) and SPPs (green line).*

boundary is sketched in figure 1.1B. Only p-polarized surface oscillations exist, since the associated field E_y is continuous across the boundary and therefore it produces no surface charge.

It is a natural idea to couple surface plasmons with light waves, since the dispersion line of light in vacuum lies close to that of the SPPs, see figure 1.1C. In the case of coupling between the surface plasma oscillations and the photons, this resonant excitation will produce a surface plasmon polariton. Hence, the word "polariton" reflects this hybrid nature, i.e. a constitution of light and surface plasmons.

The SPP dispersion relation may be derived through the use of Maxwell's equations and the boundary conditions, yielding the expression

$$\beta = \frac{k_0}{2\pi} \sqrt{\frac{\epsilon_m \epsilon_d}{\epsilon_m + \epsilon_d}} = \frac{k_0}{2\pi} \sqrt{\frac{\epsilon_m}{\epsilon_m + 1}} \quad \text{for } \epsilon_d = 1.$$

The dielectric medium during this entire work is air, thus justifying the above simplification of β . Note that the dispersion relation is a complex function with $\beta = \beta' + i\beta''$. Therefore β' is the wave vector, which is related to the SPP wavelength

$$\lambda_{SPP} = \frac{2\pi}{\beta'}$$

and β'' is the amplitude damping term. The propagation length, i.e. the distance at

which the SPP intensity is at $\frac{1}{e}$ of its initial value is, then reads

$$L_{SPP} = \frac{1}{2\beta''}. \quad (1.2)$$

The propagation length seems to increase significantly for excitation wavelengths in the infrared range as shown in figure 1.2C. The dielectric constants are similarly sketched in

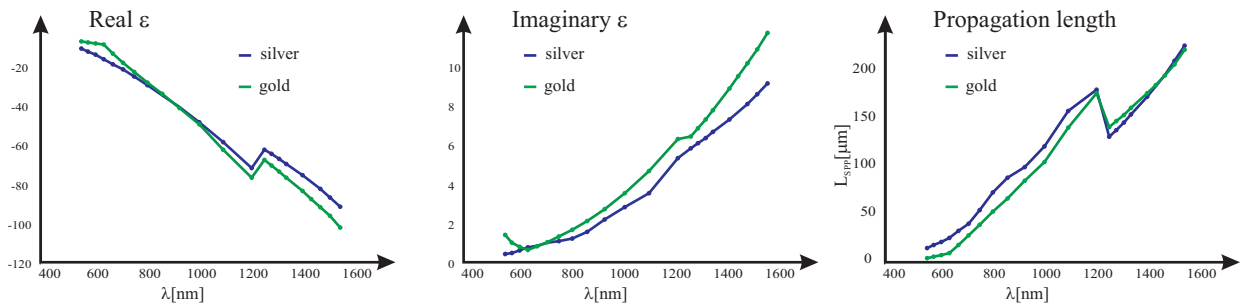


Figure 1.2: *Real (A) and imaginary (B) values of the dielectric functions of silver and gold and the corresponding propagation lengths (C).*

figures 1.2A and 1.2B [12] for silver and gold. The sudden jump in these values at around 1200nm is due to two different series of measurements. Henceforward, all calculations involving the dielectric constants of silver and gold are based on these sets of data or the interpolated values in between, which are demonstrated by the connecting lines.

Excitation of Surface Plasmon Polaritons

As the dispersion lines of figure 1.1C are non intersecting SPPs can not be generated by any direct illumination of the metal surface, except in the case of surface defects whose presence are omitted in this current picture. Therefore, an alternative approach must be made. SPP excitation is made possible by means of a coupling scheme known as the Kretschmann configuration, illustrated in figure 1.3A. The formalism associated with this is thoroughly described in appendix C. The main idea with the Kretschmann configuration is to enhance the wave vector of the applied light, via the dispersion of the prism, in order to couple with the surface plasmons. This illustrated by the dispersion relations in figure 1.3B. The prism dispersion line intersects that of the surface plasmon. The propagation of the surface plasmon is along the x-direction, so in order to conserve momentum, coupling requires that the x-component of the wave vector of the applied light should match the surface plasmon wave vector. This implies that within a broad range of frequencies, SPP excitation is always possible and the efficiency of it depends on the incident angle of the applied light.

The measured reflectivity from the Kretschmann prism can give an indication of the extent of SPP excitation. This is due to the fact that SPPs being excited on a thin film have the possibility to decay back into the prism, often referred to as the back-scattered

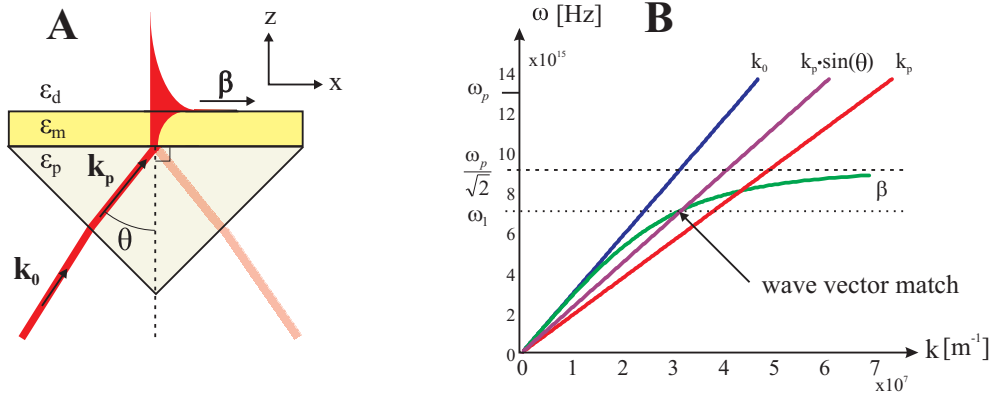


Figure 1.3: *Coupling of light with surface plasmons may be achieved using the Kretschmann coupling scheme (A), which is a prism with the metal film coating. B: the dispersion line of light within the prism (red line) intersects that of the surface plasmon (green line) unlike the dispersion line of light in vacuum (blue line). The purple line indicates the x-component of the prism wave vector.*

field or radiation damping. The reflected light at the prism-metal interface undergoes a 180° phase change thus interfering destructively with the backscattered field. The net result is a reduction of the reflectivity, usually named attenuated total reflection (ATR). Appendix D provides a careful analysis of this situation.

A quantitative description of the reflectivity is given by Fresnel's equations for a three layer, prism(p)-metal(m)-air, system

$$R = \left| \frac{r_{p,m} + r_{m,d} e^{i2k_{z,m}d}}{1 + r_{p,m} r_{m,air} e^{i2k_{z,m}d}} \right|^2. \quad (1.3)$$

See appendix E for a derivation of this expression. For a given three layer system a certain incident angle yields a minimum in the reflectivity. Figure 1.4 illustrates a performed ATR measurement, from a silver film, which exhibits this behavior. Hence, the angle of maximum excitation efficiency is found by monitoring the reflectivity from the sample.

For a certain value of the thickness it is possible to have zero reflectivity or total ATR. This is the case for silver and gold at thicknesses of approximately 45nm and 53nm respectively. In addition, at these values of the thickness the back-scattered damping is shown to equal the internal damping of SPPs in the metal. This implies that the propagation length in this case is half that of a metal layer of semi-infinite thickness expressed in (1.2). Hence, in order to experimentally increase the propagation length the thickness should be larger, but only slightly, since a very thick layer will decrease the excitation efficiency significantly.

Samples

The samples investigated during this project are sketched in figure 1.5. The silver films have been made by thermal evaporation in a pressurized chamber of 10^{-9} mbar. The gold

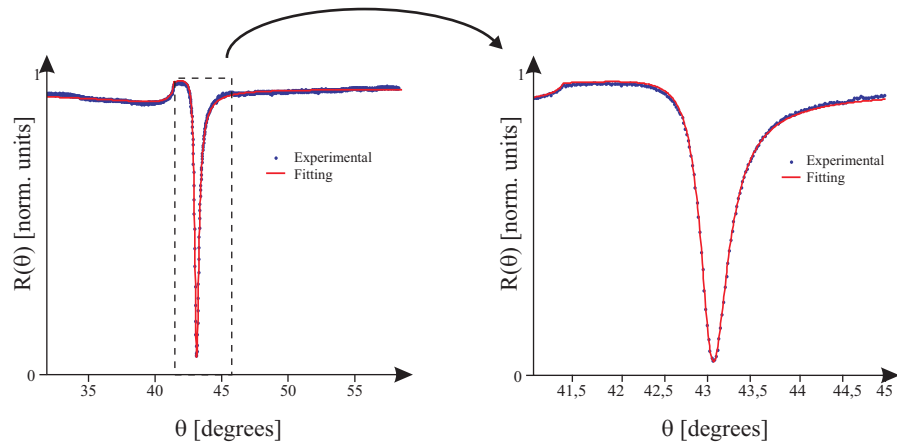


Figure 1.4: Measured reflectivity (blue line) of a 45nm thick silver film. The red line is the fitting curve based on (1.3).

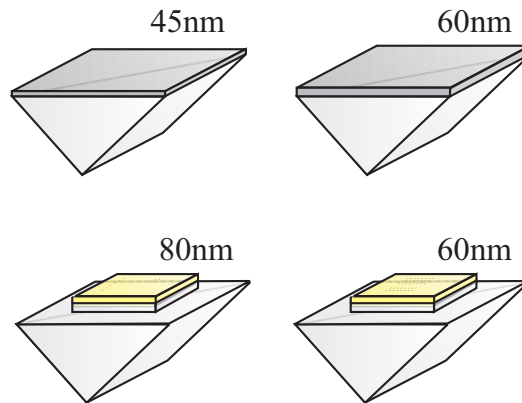


Figure 1.5: The two silver coated prisms have been made by thermal evaporation. The gold coated glass substrates are "glued" to the prism by immersion oil.

films have similarly been made by thermal evaporation, the nano-patterning has then been made by electron beam lithography on a resist layer on the film, evaporation of a second layer, and lift-off [3]. This process is sketched in figure 1.6. The result is either

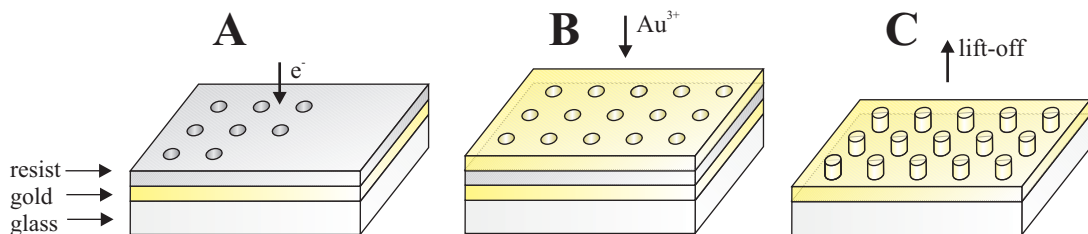


Figure 1.6: A focused electron beam draws a pattern of holes in the resist layer covering the gold film which has been vaporized on a glass substrate (A). Evaporation of a second gold layer fills in the holes (B). Removal of the resist layer and the superfluous top gold layer reveals a gold film covered with gold nano-particles (C).

simple patterns consisting of gold nano-particles with 100nm in diameter and 70nm in height or two dimensional periodic arrays, surface plasmon polariton band gap structures (SPPBG), with filling factors ranging from 0,20 to 0,32.

Scanning Near-Field Microscopy

The SPP propagation at the surface of these samples are studied with an experimental setup known as the scanning near-field (optical) microscopy (SNOM) apparatus. The operational principle is somewhat similar to that of atomic force microscopy and scanning tunnelling microscopy. Whereas the probe of the AFM apparatus typically is a microcantilever, the probe for SNOM is the tip of an optical fibre. In both techniques feedback mechanisms enables the mounted piezo-electric elements to maintain the tip at a constant force roughly at the surface. The uncoated sharp fibre tip, in close proximity to the surface, acts as a scatterer picking up scattered components, which are lead, as fibre modes, through the fibre to a detection source. The probe thus maps the SPP near-field intensity at a given area at the sample plane. The tip can, within certain approximations be considered as a non perturbing probe of the electric-field density [8].

The experimental setup is sketched in figure 1.7. The laser beam is guided through a

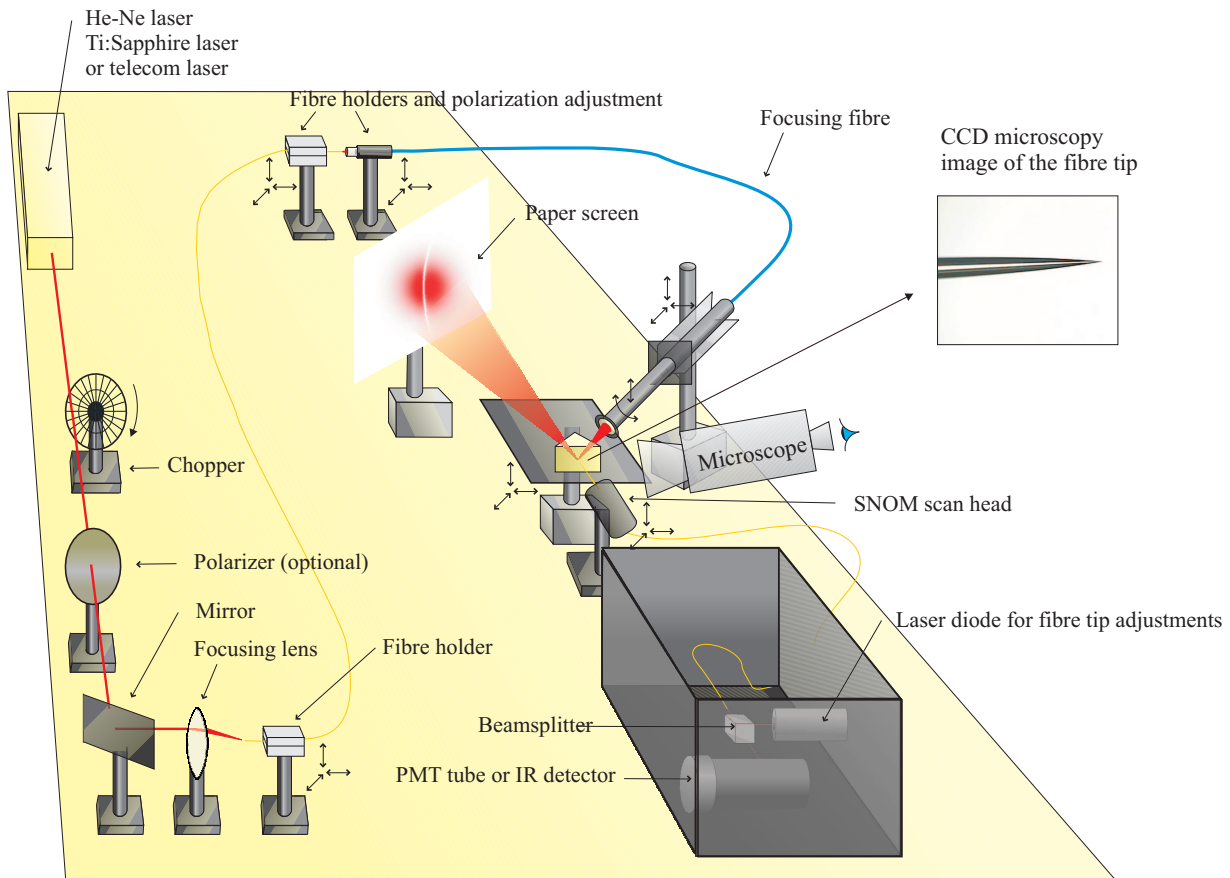


Figure 1.7: *The experimental setup for SNOM measurements using a focused excitation source. The table is vibration damped.*

chopper, giving the light a certain pulserate to which the lockin amplifier is synchronized so that signals with this pulserate are amplified and signals at other frequencies are rejected. The polarizer may be used to decrease the intensity. Subsequently, the light is guided into a fiber, which focuses the beam onto the surface. The focal length of the focuser is 9.8mm with a numerical aperture of approximately 0,25. Measurements have shown a spot size in air of roughly $6 \mu\text{m}$ at a wavelength of 810nm. Polarization adjustments are possible by twisting of the fibres at a connection joint. The optical signal is collected by the scanning fibre tip and guided to the detection source, analyzed by the lockin amplifier and then stored on the computer.

The shown experimental setup is for the case of a focusing excitation source. The focusing arrangement may be replaced by a mirror arrangement for a parallel excitation beam. In this case the beam will be weakly focused by a lens with a focal length of 50cm giving a spot size of approximately $300\mu\text{m}$. This size is sufficiently large to provide a uniform illumination intensity throughout the entire scan area, since the scanning range is limited to $60 \times 60\mu\text{m}$ by the piezo elements of the scan head.

Presentation of images, either experimental or simulated, are made based on the template of figure 1.8. For both simulated and experimental data, the resolution is indicated and

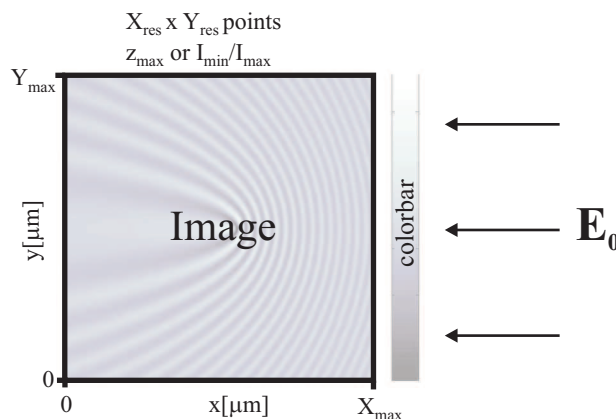


Figure 1.8: *Template for the presentation of data.*

the topographical depth or optical signal contrast are shown by either values or colorbars. In all images the incident light enters from the right unless stated otherwise.

Outline

Initially, measurements of focused excitation on planar, defect free, surfaces will be presented. A model for describing the obtained SPP intensity profile is presented, and throughout this process the deviations of the profile from the ideal case are analyzed and modelled leading to suggestions to the source of these behaviors. The experiences gained from these investigations thus serves as basis for further studies of SPP propagation from a focused excitation beam.

Subsequently, the scattered SPP field in simple structures of gold nano-particles are stud-

ied by SNOM. The modelling of these images, and of images in general throughout the rest of the report, are made by means of a multiple scattering dipole approach, where the scattered field from all nano-particles are summed yielding a resulting field intensity distribution. As a motivation, the modelling study leads to a section describing modelled SPP field distribution in possible realizable micro-optical components.

Next, modelling of SPPBG structures are carried out, starting with triangular structures where previous works serve for comparison and moving on to quadratic structures, which are also measured by SNOM. Specifically, the band gap in the SPPBG structures is studied in detail.

Ultimately, the efficiency of SPP waveguides, in terms of lines of missing nano-particles in the SPPBG structures, are investigated by SNOM.

CHAPTER 2

FOCUSING

Local excitation of SPPs may be convenient for various reasons. For instance, investigation of SPP fields without the continuous excitation from the source at the area of interest may be studied by SPPs propagating from a locally excited area at a nearby place on the sample. Other interests in this may include the need to have large excitation intensities at certain areas.

In order to achieve excitation of SPPs locally, a focuser is applied. Prior to applying this in the measurements of SPPs in nano-structures, the intensity profile on a flat surface is investigated. The reason to this is to become acquainted with the intensity profile and to explain, eventually solve, possible unexpected behaviors. Then, the future investigations with the use of local excitation will be based on better knowledge of the excitation source.

The intensity profile has been demonstrated experimentally by numerous scans at different wavelengths and for various samples with either silver or gold layers. In addition, the effects of changing polarizations and incident angle of the focuser have been investigated. See figure 2.1 for an explanation to how SPP excitation and the focuser incident angle are monitored. Naturally, SPP excitation using s-polarized light is impossible from an ideal

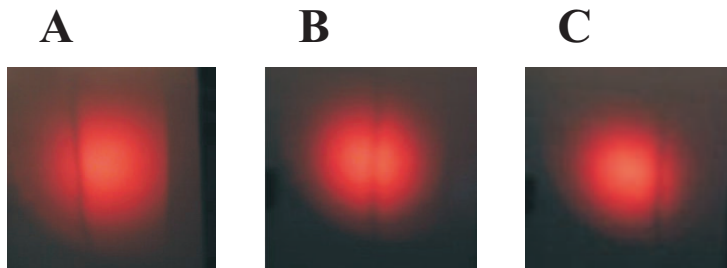


Figure 2.1: *The reflection image from a focused beam at the prism-metal interface clearly shows the presence of SPP excitation. As the field components of the focuser span over an angular range more than tenfold larger than that of the SPP excitation peak, recall figure 1.4, ATR will appear in the reflection image in the form of a dark stripe. The three digital photographs show reflection images in the case of a small incident angle (A) to larger angles (B) and (C). These three cases are henceforward denoted as left, middle and right excitation.*

point of view. However, the measurement of penetrating light at s-polarization can give a fair indication of the location of the illumination area if some of the field components, outside the TIR range, penetrate the metal film.

2.1 Modelling

A starting point for modelling is to define the illumination area. The focusing beam impinges the prism surface almost perpendicularly, so the cross sectional shape of the beam is assumed to be remained within the prism, and only the prism dispersion is taken into account involving. This leads to increased focal length and decreased focal spot beam waist with a factor of approximately the refractive index of the prism. Based on this, it seems reasonable to state that the illumination area at the prism metal interface is an oblong gaussian distribution with a beam waist in the y-direction at the focal point, see figure 2.2A, of approximately $w_y = \frac{w_0}{n_p}$. The center of the focused beam is incident on

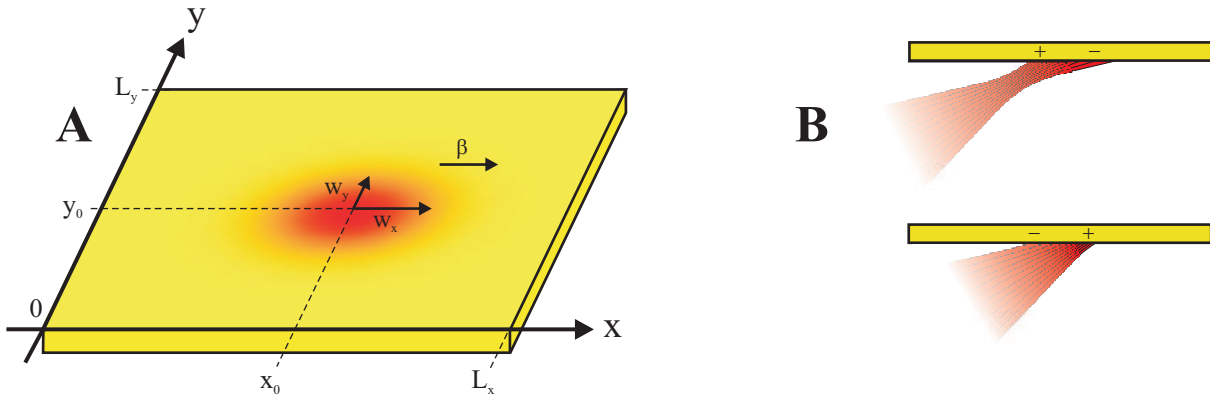


Figure 2.2: The gaussian illumination distribution at the focal spot (A) is longer in the x-direction than in the y-direction. B: When the beam is focused before (lower image) or after (upper image) the focal point, an asymmetric distribution may occur. For illustration purposes, the incident angle is exaggerated in this sketch.

the prism-metal interface at an angle of approximately 45° , so an obvious estimate of the beam waist along the x-direction is $w_x \approx w_y\sqrt{2}$. In the subsequent sections, the values of the beam waists are often written as the product of a decimal value and the square root of two, for instance $w = 3,4\sqrt{2}\mu\text{m}$. The reason to this is that the beam waist measured in an intensity profile must be multiplied by $\sqrt{2}$ to correspond to the beam waist in the amplitude profile, which is often used in the modelling. It is important not to confuse this conversion with the relationship between w_x and w_y just mentioned above.

In the case of non ideal focusing, an asymmetric intensity distribution may occur, see figure 2.2B. The possible presence of these uneven distributions are not being taken into account.

In this modelling, the angular dependent SPP excitation efficiency is omitted. Hence, the excitation efficiency at a certain point is assumed to be directly proportional to the Gaussian amplitude distribution. Additionally, it is assumed that the wave vector of excited SPPs exhibits no y-components. Based on this, the field distribution of SPPs at

the instant of excitation is gaussian on the form

$$g(x, y) = A(x_0, y_0) e^{-\left(\frac{x-x_0}{w_x}\right)^2} e^{-\left(\frac{y-y_0}{w_y}\right)^2} e^{i\beta x}.$$

As SPPs, formed at the beginning of the illumination area, propagate throughout the area of the applied field distribution, the amplitude of the SPP field is continuously being amplified. Therefore, a calculation of the field SPP field at a certain point must take the previously excited SPPs into account. Additionally, the constant decay throughout the entire process should be included. This leads to the following expression of the SPP field

$$E(x, y) = A(x_0, y_0) K_0 e^{-\left(\frac{y-y_0}{w_y}\right)^2} e^{i\beta' x} \int_0^x e^{-\left(\frac{x-x_0}{w_x}\right)^2} e^{-\beta'' dx} dx$$

where K_0 is a normalization constant. For computational purposes, the field is expressed in a similar summational form

$$E(x, y) = K_1 e^{-\left(\frac{y-y_0}{w_y}\right)^2} e^{i\beta' x} \sum_{n=\Delta x}^{N=x} A(n\Delta x, y_0), \quad (2.1)$$

with

$$A(n\Delta x, y_0) = A((n-1)\Delta x, y_0) + e^{-\left(\frac{n\Delta x-x_0}{w_x}\right)^2} e^{-\beta'' \Delta x}.$$

$A((N-1)\Delta x, y_0)$ is found from the result of the calculation of $E(x-\Delta x, y)$ which similarly requires the value $A((N-2)\Delta x, y)$ found from the calculation of $E(x-2\Delta x, y)$ and so on. In summary, a calculation of $E(x_1, y)$ requires calculation of the amplitude of all x-values (in steps of Δx) lower than x_1 until a lower limit, in these calculations for $x=0$, in which $A(0, y) = 0$. Figure 2.3 shows the result of such a calculation of $E(x, y_1)$ by the intensity distribution along the x-direction for an arbitrary value of the y-coordinate. Based on the previously mentioned assumption that SPP propagation occurs only along

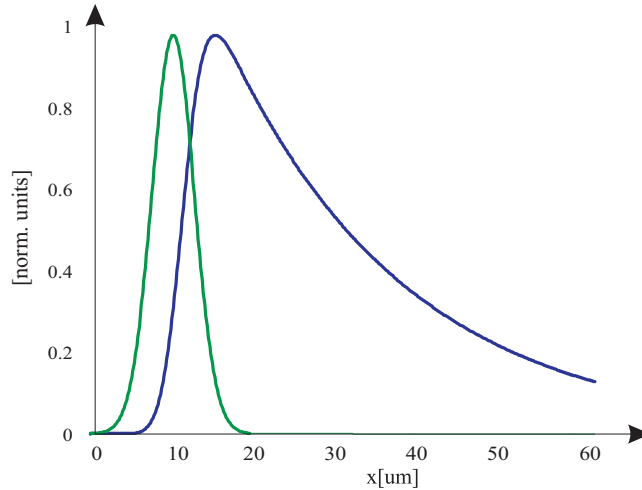


Figure 2.3: Normalized intensity graphs of the source (green graph) and the SPPs (blue graph). The calculation is performed for a semi-infinite layer of silver at 633nm.

the x-direction, and as seen through the modelling expression, it is realized that the

shape of the cross section along the y-direction is constant for all x-values. Therefore, it is only necessary to rigorously calculate the SPP field for one y-value, and then refer to the gaussian distribution function in order to obtain the intensity distribution along both directions.

The two profiles of figure 2.3 do not have peak values at the same point. This demonstrates that the SPP field is continuously being built up, even as the illumination intensity is decreasing. In figure 2.4, experimental images show the opposite relationship between these profiles. The reason to this can be due to the intensity of the propagating components

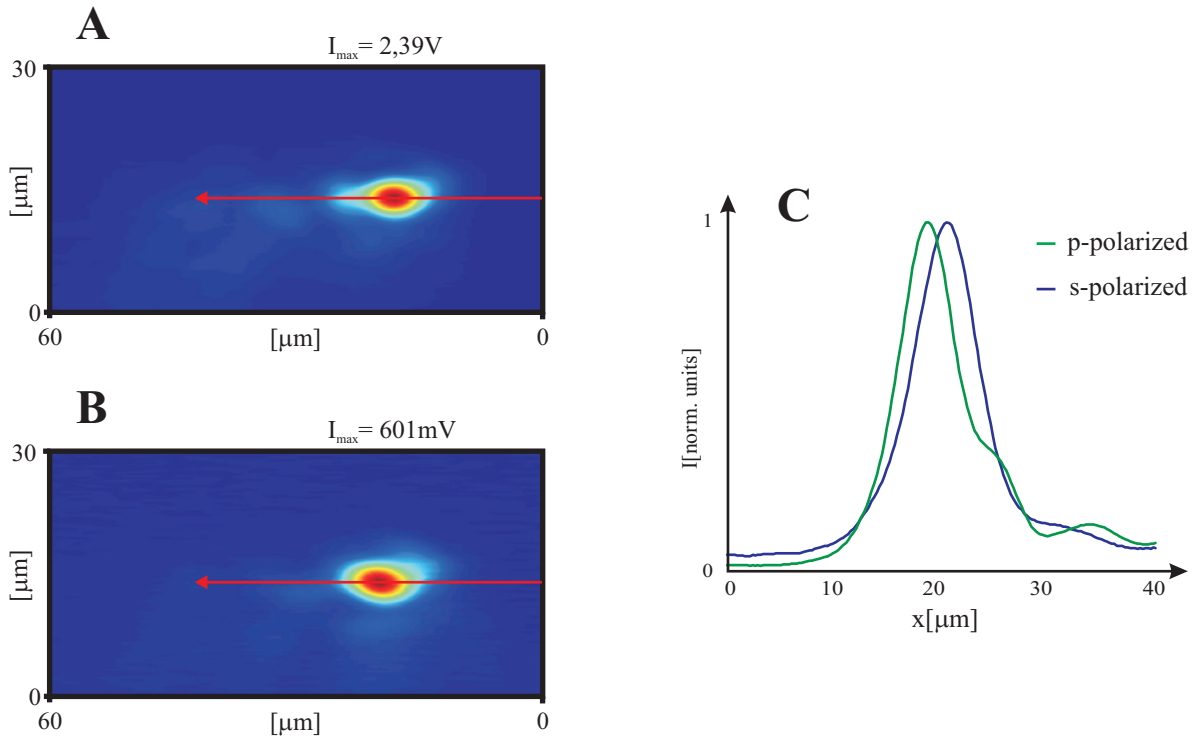


Figure 2.4: Two consecutive measurements performed with p-polarization (A) and s-polarization (B) on a 60nm thick silver layer with 633nm source wavelength. The incident angle of the focuser is rather steep, corresponding to left excitation, in order to achieve sufficient intensity for s-polarization. Nevertheless, the peak intensity ratio is still approximately 4. The intensity profiles (C) exhibit a clear difference in the point of the peak value for s- and p-polarization, respectively.

which might not be directly related to the illumination area. Conservation of momentum indicates that the propagation directions of these lie close to the horizontal plane, which suggests that propagating components may impinge and couple into the fibre only after the tip has passed the illumination area. This distance dependency may thus be larger than the distance of the building of the SPP intensity. However, similar measurements for longer wavelengths could, due to the weaker damping, yield larger building distances demonstrating the effect.

2.2 Beam Waist Dispersion and Propagation Lengths

Two of the profile scans are shown in figures 2.5 and 2.6 using middle excitation. The

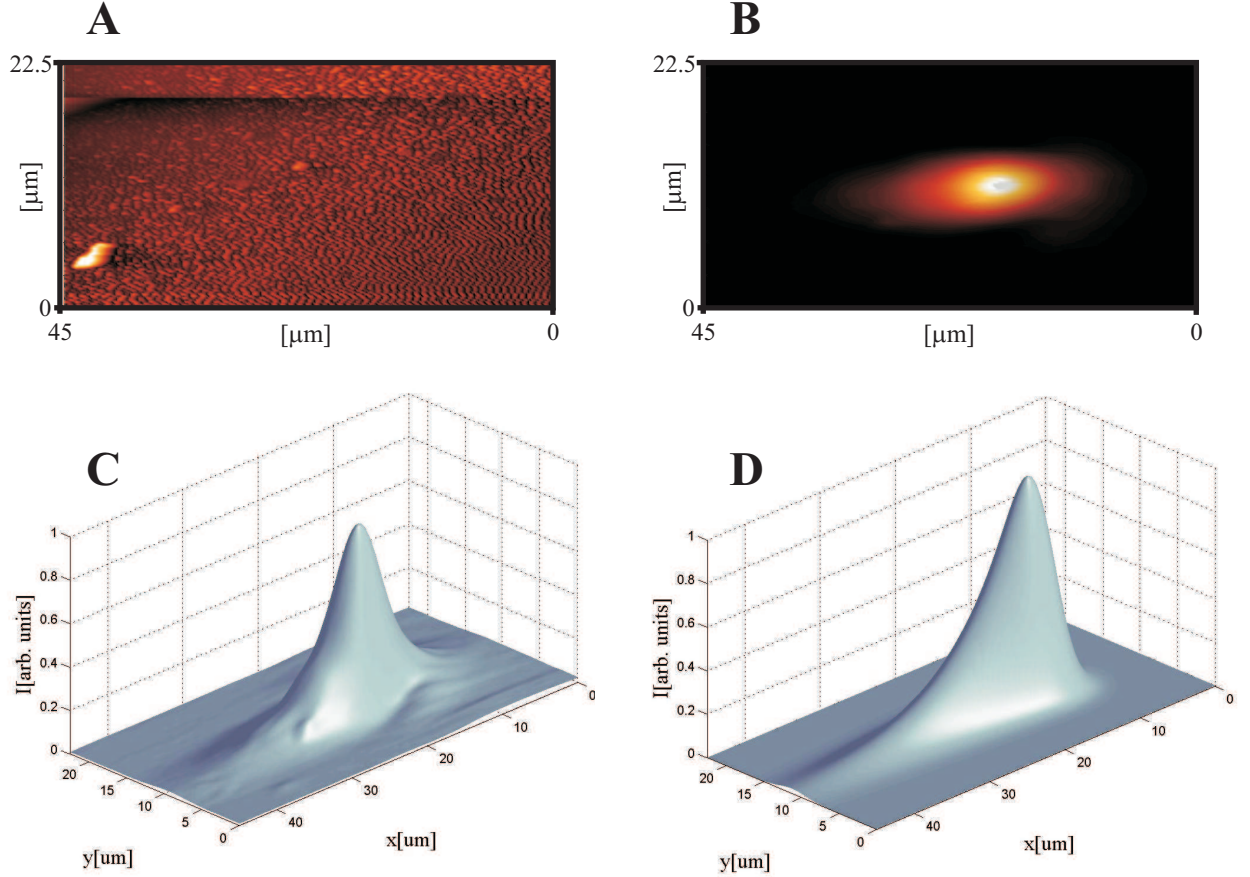


Figure 2.5: *Topographical (A) and near-field (B) measurements of local SPP excitation at the surface of a 50nm thick gold layer. The source wavelength is 633nm and the image resolution is 0.18μm. C: The 3D presentation of the optical signal. D: Modelling of the near-field intensity distribution using $w_y = 2.5\sqrt{2}\mu\text{m}$ and $\epsilon = -9,60 + 1,01i$.*

value of the beam waist, along the optical axis, used in the modelling of the intensity profiles, have been estimated based on a cross section profile measurement of the optical image at the peak value.

Consider the 3D representations of experimental and simulated data in figures 2.6C and 2.6D - the shape of the intensity profiles at the end of the profile, for $x = 45\mu\text{m}$, clearly seem to differ. The gaussian profile of the experimental image is both broader and of lower peak value than that of the simulated.

The reason to the broad profile could stem from the approximation, introduced previously in this chapter, that SPPs are propagating in the exact same direction. When the beam is not parallel, as it is the case with the focuser, it is easy to imagine the gaussian profile being spread out, starting from the excitation point, along the propagation direction, due

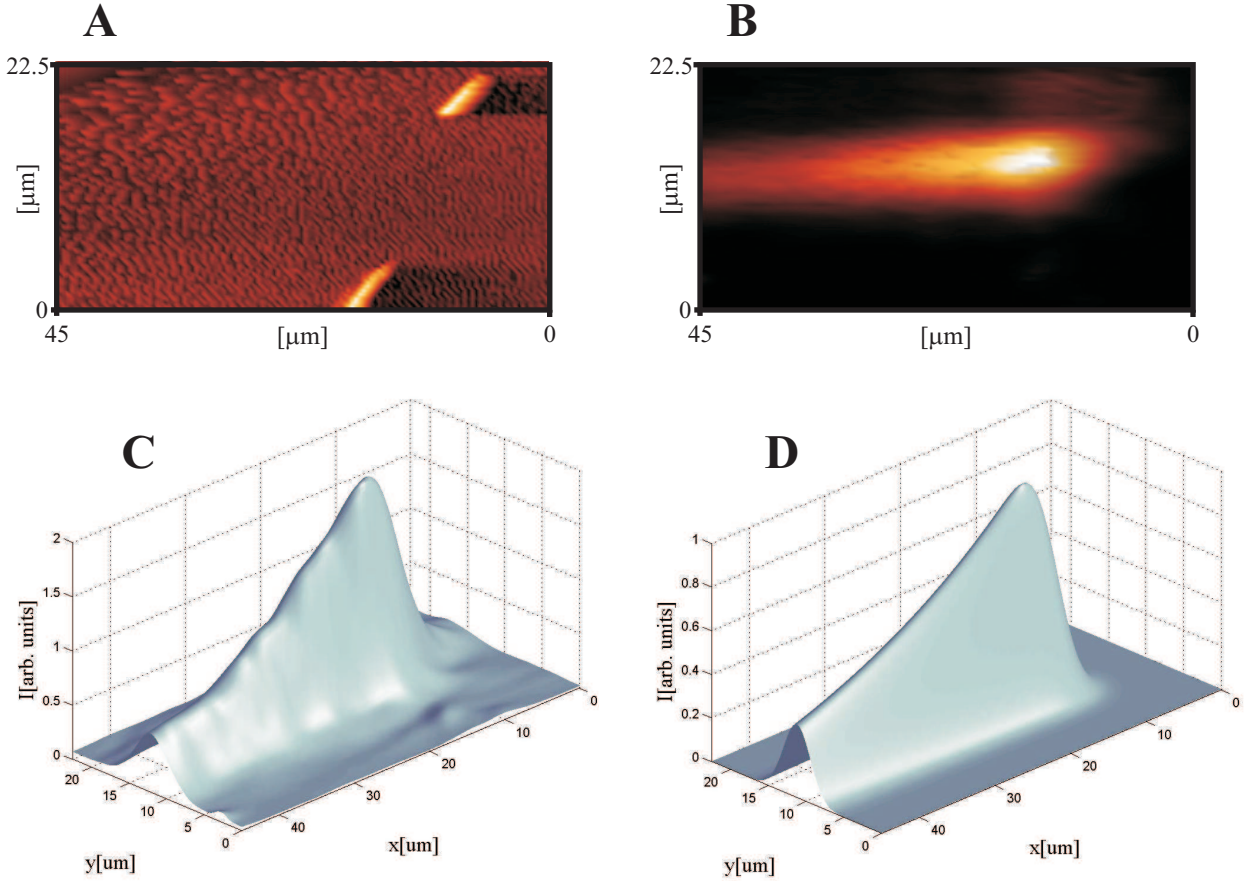


Figure 2.6: *Topographical (A) and near-field (B) measurements of local SPP excitation at the surface of a 50nm thick gold layer. The source wavelength is 727nm and the image resolution is 0.35μm. C: The 3D presentation of the optical signal. D: Modelling of the near-field intensity distribution using $w_y = 3.0\sqrt{2}\mu\text{m}$ and $\epsilon = -18,6 + 1,41i$.*

to SPPs with wave vectors made up by different values of the y-component. This theory is supported by beam waist measurements of the optical signals in figures 2.5B and 2.6B. For this purpose, the construction of an image analyzing procedure, measuring interpolated values of the beam waists starting at the peak value and moving along the propagation direction, has been carried out. The results are shown in figure 2.7A. Although the graphs exhibit oscillatory behaviors, the width of the beam seems to be generally increasing. The consequence of this would obviously be a broader gaussian cross section with a lower peak value. In addition to this, it should be mentioned that a similar feature which may cause beam waist dispersion is inelastic scattering in the surface plane.

As far as the peak value is concerned, a decrease in the propagation length of the experimental image could similarly affect this. Figure 2.7B shows decaying profiles along the x-direction after the illumination area for each of the scans of figures 2.5 and 2.6. From the corresponding exponential fitting curves, the propagation lengths are found. These show to be slightly smaller than the calculated values of $7,86\mu\text{m}$ and $26,3\mu\text{m}$ of 633nm and 727nm, respectively. Additional damping in terms of radiation damping, described

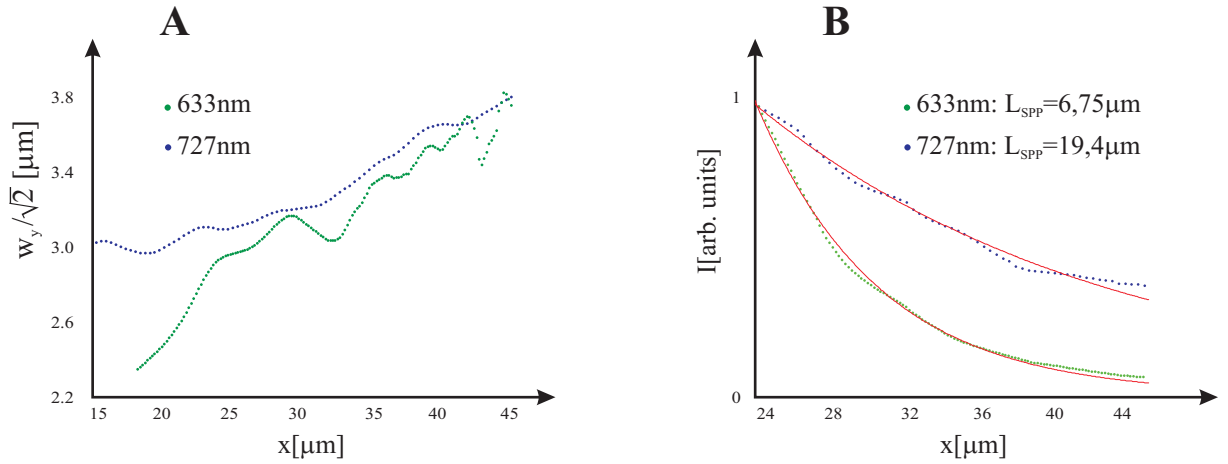


Figure 2.7: *A: Calculated beam waists of the optical signals of figures 2.5B and 2.6B. B: Measured and fitted propagation lengths based on the decaying profile after the illumination area.*

in detail in appendix D, and a small contribution in terms of possible inelastic scattering from nano-sized protrusions may be taken into account, thus justifying the lowering of the peak value. It should be borne in mind that beam waist dispersion may similarly cause a lowering of the peak value.

Based on these considerations, an attempt to improve the model is made. The last cross section of normalized representations of the measured and simulated intensity, figures 2.6C and 2.6D, respectively, are integrated and compared. The summed intensity of the experimental image is, as expected, lower than the modelled one. This shows that, at least in this comparison, a slight additional decay should be introduced in order to fit the model to the experimental image. The additional decay is expected due to back scattering, which is possible even for a "thick" layer of 80nm. The broadening of the gaussian distribution is made up for by considering the beam waist dispersion graphs in figure 2.7A. A rough estimate of the beam waist along the x-direction is presented in the graph of figure 2.8A. This is applied in the modelling of the experimental scan of figure 2.6C and gives a slight improved resemblance.

2.3 Oscillations

Although the shape of the modelled and experimental intensity profiles are quite similar, oscillations along the propagation direction are quite noticeable. This may be due to the presence of penetrating, propagating components interfering with the near-field components in the fibre, see figure 2.9A. The sketch in figure 2.9B illustrates the angular range where these propagating components are expected, so the amount of propagating components may depend on the incident angle of the focuser. Additional factors responsible for propagating components may include layer thickness and film material which have an effect on the amount of transmittance through the film. Finally, the fibre tip may be shaped in a manner which picks up the propagating signal more efficiently than

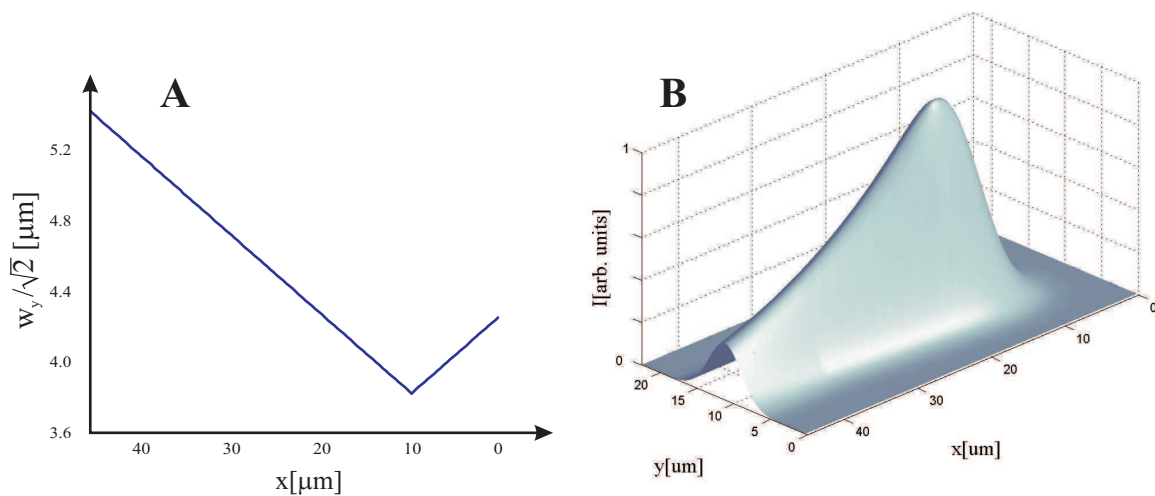


Figure 2.8: *By allowing a dispersion in the beam waist (A) and by introducing an additional decay, the modelling of figure 2.6D has been slightly improved (B). The decay has been introduced in terms of an additional damping term of the value $0,44i$ in the dispersion relation, giving a total of $\epsilon = -18,6 + 1,85i$.*

the SPP signal leading to large interference effects. Figures 2.9C and 2.9D show a scan which exhibits large interference effects. There has been a clear decrease in this effect as investigations have moved from the 45nm silver film to the 60nm silver film. This seems reasonable, as a thinner layer transmits applied light outside the TIR range more easily. The assumption needs further considerations to be fully justified: One may argue that a thicker layer leads to less SPP excitation thus cancelling the effect of a lower propagating field. However, it should be mentioned that a thicker layer in fact can cause a larger SPP field. At first, this seems contradictory, but further analysis of this situation implies that a thicker layer also leads to less backscattered damping - the field is being built up over a larger distance, exhibiting a larger peak value.

Taking fully account of the propagating components in the modelling of the SPP field requires elaborate considerations of the shape of the fibre tip, the angular distribution of the transmitted light, etc. Hence, another approximation is introduced. All the propagating components are assumed to originate from the illumination area, which seems fair in the case of an ideally flat surface. In addition, these are assumed to propagate in the same direction. Therefore, the intensity profile of propagating components along the x-direction is assumed to be an exponentially decaying function starting at the point corresponding to the peak value in the SPP intensity. In order for this function to be continuous, it is increased in a gaussian-like manner before the point of the peak value. The function resembles the SPP profile of figure 2.3, but its exponent and peak value are allowed to be used as a fitting parameters.

The interference between propagating components and the SPP field is possible due to the relationship $k_0 \cos(\theta) < \beta'$, where θ is the angle between the surface and the direction of k_0 . The length of the oscillations are many times larger than the light wavelength,

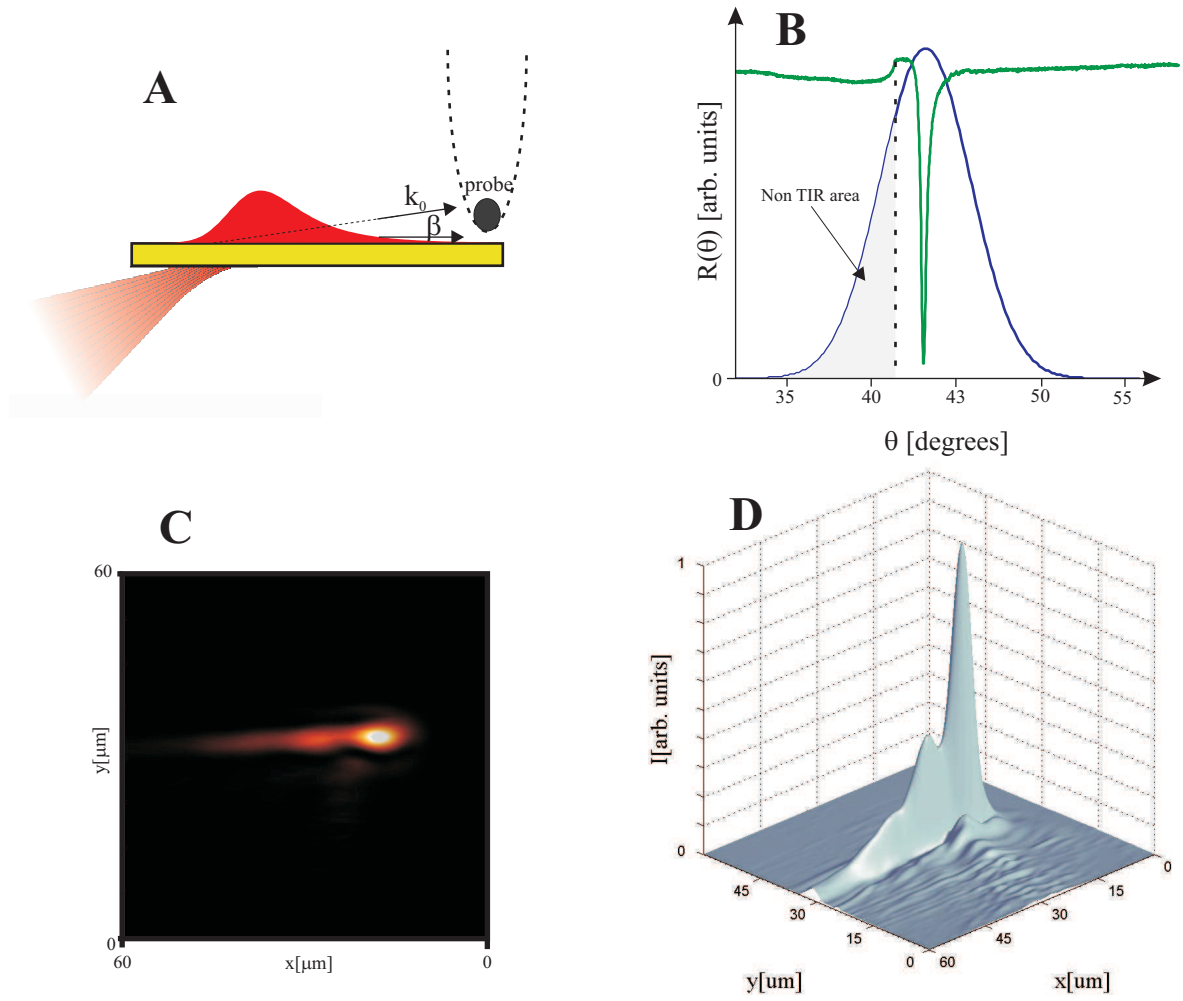


Figure 2.9: Illustration of the influence of propagating components on the detected signal (A). The graphs of the ATR Reflectivity and the gaussian distribution for "middle excitation" (B) give an indication of the amount of components, in the illumination area, which are allowed to propagate. The 2D (C) and 3D (D) representations of a near-field measurement of an intensity profile, on a 45nm thick silver layer with 633nm source wavelength, show a profound effect of the claimed interfering propagating components.

so this fits with the relatively close magnitudes of the two wave vectors. For instance, the ratio between these for SPPs at a silver surface with 633nm source wavelength is 0,968. Any additional decrease in this ratio can be justified by introducing a small angle. The calculation of the SPP field, taking propagating components into account, is then expressed as

$$E_{osc}(x, y) = E(x, y)(1 + A_{prop}e^{i(k_0 \cos(\theta)x + \phi)}),$$

where $E(x, y)$ is the calculation described in (2.1) and A_{prop} is the amplitude profile of the propagating components. The ratio $A_{prop,max}/A_{max}$ is thus a factor describing the extent of interference, which is applied in the modelling process. The origin of the propagating components is assumed to be known, however, the parameter ϕ allows for possible phase

delays.

The modelling of the oscillations has been performed on two of the previous shown scans, see figure 2.10.

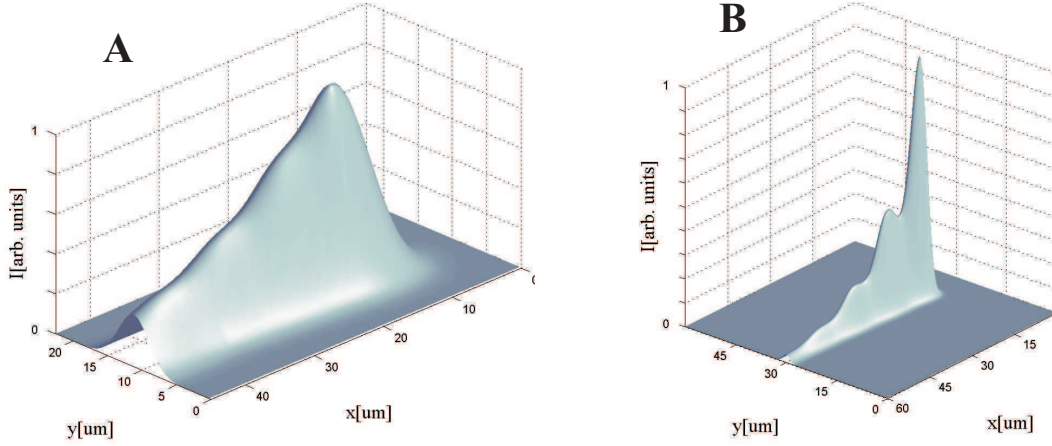


Figure 2.10: In figure **A** and **B**, respectively, the measured SPP fields of figures 2.6C and 2.9D have been modelled with the oscillations taken into account. The applied parameters for **A** are: $\theta = 19^\circ$, $A_{prop,max}/A_{max} = 0,012$, $\phi = 0,5$ and $w_y = 4,0\mu m$. For **B** these are: $\theta = 11^\circ$, $A_{prop,max}/A_{max} = 0,15$, $\phi = 0,4$ and $w_y = 2,0\mu m$.

Concluding Remarks

By modelling the intensity profile based on performed measurements, many of the behaviors, which at first seem unexpected, are explained. When knowing the source of these behaviors, it is possible to perform more well qualified tasks in order to avoid these side effects and obtain a more ideal intensity profile.

Based on the analysis of the influence of propagating components, it is strongly suggested to use a coated fibre tip in order to reduce these interference effects.

However, an alternative way to meet this problem, while maintaining a bare fibre tip and tight focusing, is to perform the SPP excitation at the angle of the largest gradient in the gaussian intensity distribution, $I_g(x) = e^{-\frac{x^2}{w^2}}$. The reason to this is to have the intensity of the propagating components as low as possible compared to that of the SPP excitation. Mathematically, this is expressed as the value x_0 to which the tangent to $I_g(x)$ has the largest slope. This is found to be the value of x which solves the equation

$$\begin{aligned} \frac{d^2 I_g(x)}{dI_g(x)^2} &= 0 \Rightarrow \\ x_0 &= \pm \frac{w}{\sqrt{2}}. \end{aligned}$$

Applying this value to $I_g(x)$ indicates that the SPP excitation stripe should be in a range where the intensity is approximately $e^{-\frac{1}{2}}I_g(0)$, or 61% of $I_g(0)$ where $I_g(0)$ is the maximum intensity in the middle of the distribution.

On the other hand, it has been demonstrated by [9] on thin silver films with thicknesses in the same range as in this work, that intensity profiles with no observed interference effects can be obtained using a bare fibre tip. However, for these measurements, focusing was obtained by applying a beam expander (20X) followed by a best form laser lens with a focal length of 19,0 cm. It has not been possible, from this information, to derive the very angular range of the arc of components for comparison, but the cross sections showed practically no beam waist dispersion. This could indicate a smaller angular range than that of the focusing fibre. An applied focusing beam with a small angular range at incident angle close to SPP resonance may lead to less propagating components and increased SPP excitation efficiency thus reducing the interference effects.

CHAPTER 3

ELASTIC SCATTERING

There are several possible ways in which SPPs propagating at a metal surface may change their current nature and direction. For instance, SPPs may decay due to either interaction with the phonons of the metal or by radiating back into the coupling media contributing to ATR as mentioned previously. Now, suppose the surface is different from a perfectly flat one with protrusions along the surface. These may interact with the SPPs in mainly two ways: on one hand, the SPPs can be scattered out of the surface plane, inelastic scattering, thus leaving the coupling system as regular photons. On the other, hand SPPs may undergo elastic scattering, which refers to scattering in directions still confined to the surface plane. This project deals with investigations of the near-field, which is strongly confined to the surface plane, so only the latter type of scattering is considered.

A common denominator of the samples investigated throughout this project is the presence of artificially made scatterers. The consequence of this presence is an interference pattern due to interaction of the applied field with the scattered and with a contrast comparable to the efficiency of the scatterer. In structures of multiple scatterers located close to each other, for instance in a surface plasmon polariton band gap structure, an additional contribution to the interference pattern is the effect of interaction between multiple scattered fields. Consideration of the extent of this contribution is made by comparing the SPP propagation length (1.2) with the elastic scattering mean free path related as

$$l \sim \frac{R^2}{\sigma},$$

where R is the average scatterer separation distance and σ is the total elastic scattering cross section of the scatterer. These considerations imply that, if l becomes increasingly large compared to L_{SPP} , the effect of multiple scattering in the interference pattern increases.

3.1 *Self-consistent Model*

The calculation of the scattered field from a single scatterer of a particular shape is in general quite complicated and requires extensive theoretical considerations [13] which goes far beyond the framework of this project. Hence, the individual scatterers are treated as isotropic pointlike dipolar scatterers. Modelling of the interference pattern using this multiple scattering dipole approach is realized by means of a self-consistent model [14]. This model is based on some assumptions. First, the scattering is elastic and primarily in the surface plane as mentioned above. Secondly, the SPP scattered by an individual defect corresponds to the interference between the incoming SPP with a plane phase front and the scattered SPP with a cylindrical phase front. These assumptions are justified by experimental investigations showing exponential, evanescent, signal decay at increased

tip-surface distances and parabolic interference fringes with SPP scattering by individual defects [15].

The cylindrical waves of scattered SPPs, the cylindrical surface polaritons (CSP) [16], can be described by the Hankel function of the first kind, whose analytical expression is the sum of two Bessel functions

$$\begin{aligned} H_n^{(\nu)}(x) &= J_n(x) + iY_n(x), \quad \text{with} & (3.1) \\ J_n(x) &= x^n \sum_{m=0}^{\infty} \frac{(-1)^m x^{2m}}{2^{2m+n} m!(n+m)!} \quad \text{and} \\ Y_n(x) &= \frac{1}{\sin n\pi} [J_n(x) \cos n\pi - J_{-n}(x)]. \end{aligned}$$

The superscript ν and the subscript n indicate the kind and the angular number, respectively. In the case of a CSP, $\nu = 1$, $n = 0$ and the argument is $\beta|\mathbf{r}|$. Surface plots of the real and imaginary values of this function with the value of the dispersion relation β corresponding to SPPs excited at 740nm on gold are shown in figure 3.1. Due to the

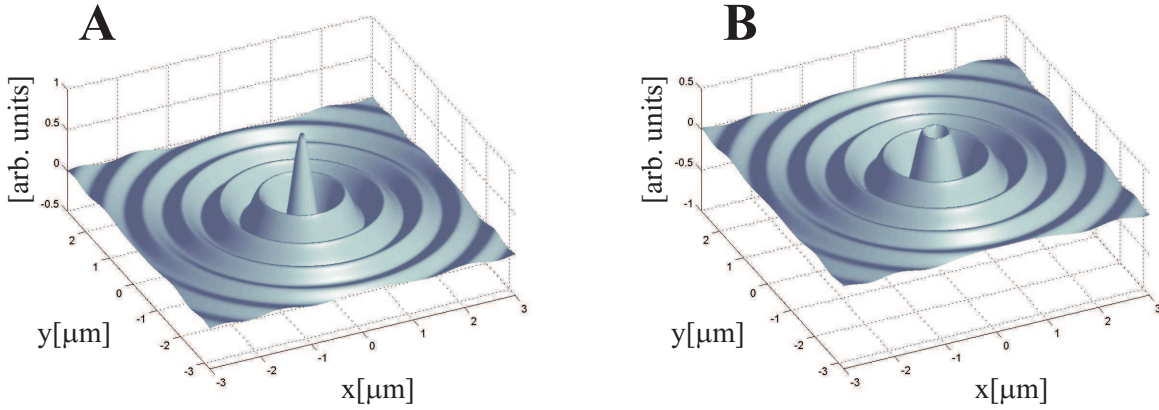


Figure 3.1: Surface plots of the real (**A**) and imaginary (**B**) parts of the $H_0^{(1)}$ function.

singularity at origo, the Hankel function exhibits values which are unreal from a physical point of view when the argument is sufficiently small. In order to avoid any of these irregularities, the Hankel function can be assigned a constant value within an area corresponding to the size of the scatterer - in this case, nano-particles or cylinders with a radius of 100nm.

Far-Field Approximation

The far-field approximation of the Hankel function reads

$$H_0^{(1)}(\beta|\mathbf{r}|) = \sqrt{\frac{2}{\pi}} e^{-i\frac{\pi}{4}} \frac{e^{i\beta|\mathbf{r}|}}{\sqrt{\beta|\mathbf{r}|}} \quad \text{for } |\mathbf{r}| \rightarrow \infty. \quad (3.2)$$

This is applicable for positions of \mathbf{r} which are different than at the immediate vicinity of the scatterer, see figure 3.2. Only at positions very close to zero, for $|\mathbf{r}| < 100\text{nm}$,

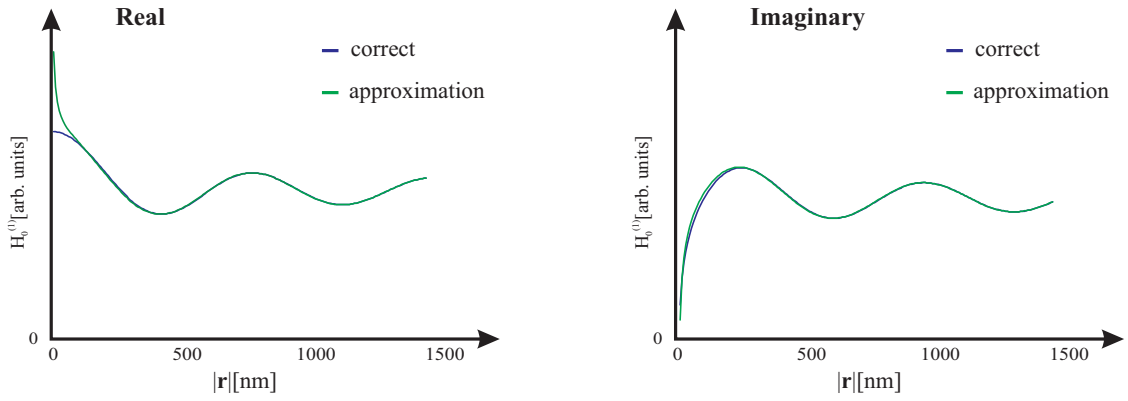


Figure 3.2: Line plots of real and imaginary parts of the $H_0^{(1)}$ function shown for the correct expression in (3.1) and for the far field approximation in (3.2).

the approximation is considered useless. However, in either case, for positions below this limit, the function will be assigned the aforementioned constant value, so the far-field approximation is considered useful for any calculation of scattered fields.

Since the damping of the host media is closely related to the CSP (or SPP) propagation length, the Hankel function similarly depend on this. Consequently, increased damping leads to increased decay of the Hankel function. Figure 3.3 illustrates the CSP scattered field at three extents of damping. Based on these observations, the scattering may be

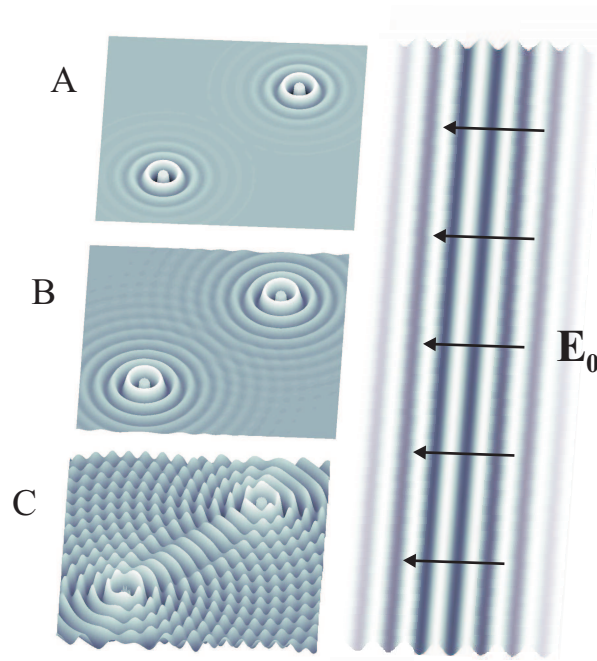


Figure 3.3: The scattered CSP fields from two scatterers in the case of large (A), middle (B) and low (C) damping.

categorized into three types:

- Single scattering, for $L_{SPP} < l$
- Double scattering, for $2l > L_{SPP} > l$
- Multiple scattering, for $L_{SPP} \gg l$

In single scattering, the image is formed by only the incoming field being scattered at each of the scatter sites. In double scattering there is an additional contribution to the field being scattered due to the presence of other scattered fields originating from nearby scatterers. If the separation distance is decreased further, part of the field to be scattered at an individual site may come from the very same scatterer due to the possibility of backscattering (*not* to be confused with backscattered fields, radiation damping) - the field is self-consistent. These different cases are taken into account in the modelling.

Omitting the exponential decay of the SPP field into the neighbor medium, the field, at an arbitrary surface point \mathbf{r} different from that of the scatterers, is expressed as

$$E(\mathbf{r}) = E_0(\mathbf{r}) + \sum_{j=1}^N \alpha_j E(\mathbf{r}_j) G(\mathbf{r}, \mathbf{r}_j), \quad (3.3)$$

where the j index indicates the scatter number. \mathbf{r}_j and α_j denote the position and effective polarizability of the j th scatterer, respectively. The Green's function reads

$$G(\mathbf{r}, \mathbf{r}_j) = \frac{i}{4} H_0^{(1)}(\beta|\mathbf{r} - \mathbf{r}_j|). \quad (3.4)$$

Clearly, the field is calculated by considering individual contributions from each of the scattered fields in agreement with the above description. The calculation of the field at the sites of the scatterers $E(\mathbf{r}_j)$ may be simplified according to the type of scattering:

- Single scattering: $E(\mathbf{r}_j) = E_0(\mathbf{r}_j)$
- Double scattering: $E(\mathbf{r}_j) = E_0(\mathbf{r}_j) + \sum_{l=1, l \neq j}^N \alpha_l E_0(\mathbf{r}_l) G(\mathbf{r}_j, \mathbf{r}_l)$
- Multiple scattering: $E(\mathbf{r}_j) = E_0(\mathbf{r}_j) + \sum_{l=1, l \neq j}^N \alpha_l E(\mathbf{r}_l) G(\mathbf{r}_j, \mathbf{r}_l)$

For single and double scattering the fields are calculated in a straightforward sequential manner. However, the calculation of the fields of multiple scattering involves a system of N homogeneous linear equations leading to a matrix formulation

$$\begin{aligned} \mathbf{E}^T &= \mathbf{E}_0^T + \mathbf{E}^T \overleftrightarrow{G}_\alpha \Rightarrow \\ \mathbf{E}^T &= \mathbf{E}_0^T (\overleftrightarrow{1} - \overleftrightarrow{G}_\alpha)^{-1}, \end{aligned} \quad (3.5)$$

where \mathbf{E}_0^T and \mathbf{E}^T are row vectors containing N elements of the applied and the self-consistent field, and $\overleftrightarrow{G}_\alpha$ is a $N \times N$ matrix containing elements on the form $G_{\alpha,ij} = \alpha_j G(i, j)$. Therefore, the calculation of the self-consistent fields seems more difficult.

At first, the concept of categorizing different types of scattering has been used to illustrate the scattering processes. Secondly, the approximations of single and double scattering can be used to ease calculations as just demonstrated. However, the calculation of the self-consistent fields can be solved by aid of a regular PC which, at this time, easily solves systems with $N \sim 1000$ within few minutes. This involves the simplification that every situation of scattering, regardless of the relationship between L_{SPP} and l , will be treated as multiple scattering.

Polarizability

The effective polarizability enters into the self-consistent model in a direct relation to the scattering strength. The following section serves to give estimates of the range of allowed values of α .

A first approach is to consider the scattered power versus the incident field related as

$$P_{sc} = I_0\sigma.$$

Since this is treated as a two-dimensional case, the units of I_0 and σ are power per length and length, respectively. All scattered field components at a distance $|\mathbf{r}|$ from the scatterer originate from the same instantaneous scattering process, so the scattered power is then expressed as a sum of these components

$$\sigma I_0 = \int_0^{2\pi} (|E_{sc}(\mathbf{r})|^2 + I_0(\mathbf{r}))|\mathbf{r}|d\varphi,$$

where the position \mathbf{r} belongs to the circumference of a circle centered at the scatterer in origo. I_0 is a plane wave, so the integration of this yields zero. The scattered field is assumed, from (3.3), to be $\alpha E(\mathbf{r})G(\mathbf{r},0)$. Using the far-field approximation for the scattered field gives the result

$$\begin{aligned} \sigma I_0 &= \int_0^{2\pi} |\alpha|^2 |E_0|^2 \frac{1}{8\pi\beta|\mathbf{r}|} |\mathbf{r}| d\varphi \\ &= |\alpha|^2 I_0 \frac{1}{4\beta}. \end{aligned}$$

The scatterers are nano-sized, so the cross section is assumed much lower than the SPP wavelength:

$$\sigma = \frac{|\alpha|^2}{4\beta} \ll \lambda_{SPP}, \quad \text{with} \quad \beta \approx \frac{2\pi}{\lambda},$$

giving the result $|\alpha| \ll 5$. This provides an indication of a higher limit for the polarizability of subwavelength scatterers.

According to an analytical study of localization of electromagnetic waves in two-dimensional random arrays of dielectric cylinders [11], the self-consistent field equation reads

$$E(\mathbf{r}_j) = E_0(\mathbf{r}_j) + \frac{1}{2} \sum_{l=1, l \neq j}^N G_1(\mathbf{r}_j, \mathbf{r}_l)(e^{i\phi_l} - 1)E(\mathbf{r}_l), \quad (3.6)$$

with the Green's function expressed as

$$G_1(\mathbf{r}_j, \mathbf{r}_l) = \frac{2}{i\pi} K_0(-i\beta|\mathbf{r}_j - \mathbf{r}_l|) = H_0^{(1)}(\beta|\mathbf{r}_j - \mathbf{r}_l|).$$

Substitution of the Green's function of (3.4) into the self-consistent field expression of (3.6) yields

$$E(\mathbf{r}_j) = E_0(\mathbf{r}_j) + \frac{1}{2} \sum_{l=1, l \neq j}^N \frac{4}{i} G(\mathbf{r}_j, \mathbf{r}_l) (e^{i\phi_l} - 1) E(\mathbf{r}_l)$$

thus relating α to a value of $-2i(e^{i\phi_l} - 1)$ where ϕ_l is some arbitrary real number. The maximum value of $|\alpha|$ with this definition is 4 when $\phi_l = \pi$, so it stays within the above estimated range.

The considerations just made have not revealed any means of calculation of α . Henceforward, the effective polarizability is applied as a fitting parameter allowed to have a complex value and to vary within the estimated range. The applied values will be mentioned either as a scalar value or as a phase number ϕ_l .

3.2 *Micro-optical Devices*

The following section reflects some of the ideas regarding applications of elastic SPP scattering, which naturally arise during the modelling process. The ideas are partly inspired by previous works [1, 18].

The devices are common in the sense that the individually scattered fields of each nanoparticle placed in a certain structure add up to give a certain overall enhanced effect. The results of the modelling of the SPP field intensity in these devices may provide a basis and motivation for future experimental investigations.

As previously mentioned, a single circular nano-particle scatterer is assumed to scatter light as cylindrical waves, so no preferred direction of scattering is present. The scatterers may not be perfectly circular, but nevertheless, this assumption seems necessary as further considerations would have to include the unknown and experimentally varying structure of the scatterer. By placing scatterers in line arrays, a common plane wavefront of the scattered light can be achieved, see figure 3.4. From an application point of view, it seems obvious to exploit line arrays to reflect the wavefront of the applied field - to make a mirror effect. The idea has been modelled for a line array, whose inclination compared to the applied field is 45° , $3\mu\text{m}$ in length. The images are shown in figure 3.5. The efficiency of the mirror effect can be increased by applying a larger polarizability. However, suppose the polarizability is constant, since experimentally it may not be easily tuneable. The efficiency can then be increased by a larger concentration of nano-particles per unit length, which is clearly demonstrated by figure 3.5B. The line arrays are far from being perfect mirrors since much of the incident light passes through the structures. This phenomenon can be compensated for by placing additional lines parallel to the first with separation distances that satisfies the Bragg condition, $2d \sin \theta = n\lambda$, where d is

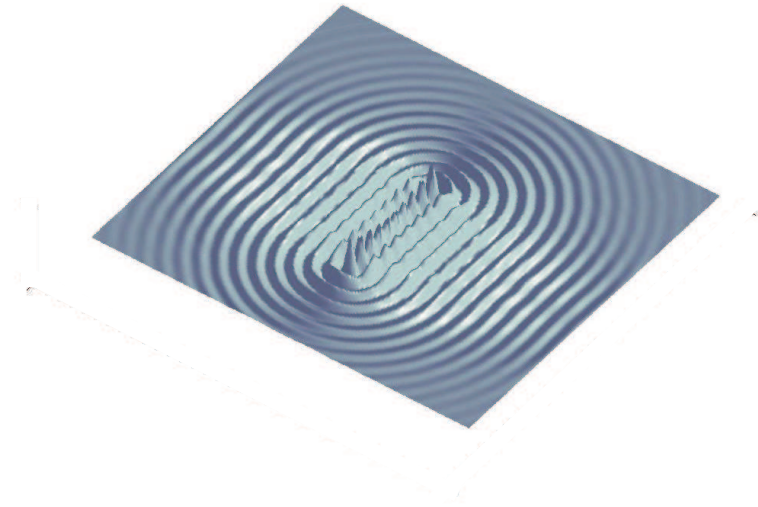


Figure 3.4: In a line array, the CSP response of the scatterers may form a plane wavefront in the direction perpendicular to the line. In this case, shown by the real part of the sum of Hankel functions for 10 nano-particles spaced $0,6 \mu\text{m}$ apart with a source wavelength of 740nm .

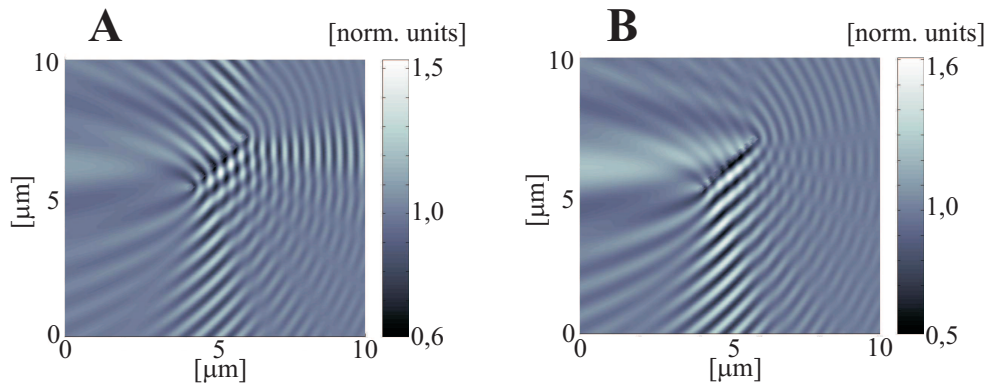


Figure 3.5: Micro mirrors consisting of line arrays of nano-particles with a separation distance of $0,50\mu\text{m}$ (A) and $0,28\mu\text{m}$ (B). The polarizability is set to $0,7$ and the source wavelength is 727nm .

the separation distance, θ is the angle the beam makes with the mirror and n is a whole number.

Modelling of SPPs incident on a Bragg mirror is illustrated in figure 3.6 for a focused intensity profile of the incident SPPs made by a source wavelength of 1550nm , demonstrating the feasibility for telecommunication ranges of light. The propagation length in this range is quite large, $\sim 400\mu\text{m}$, so the decay of the incident field is barely seen. The Bragg mirror has shown to reflect the light most efficiently for a complex polarizability.

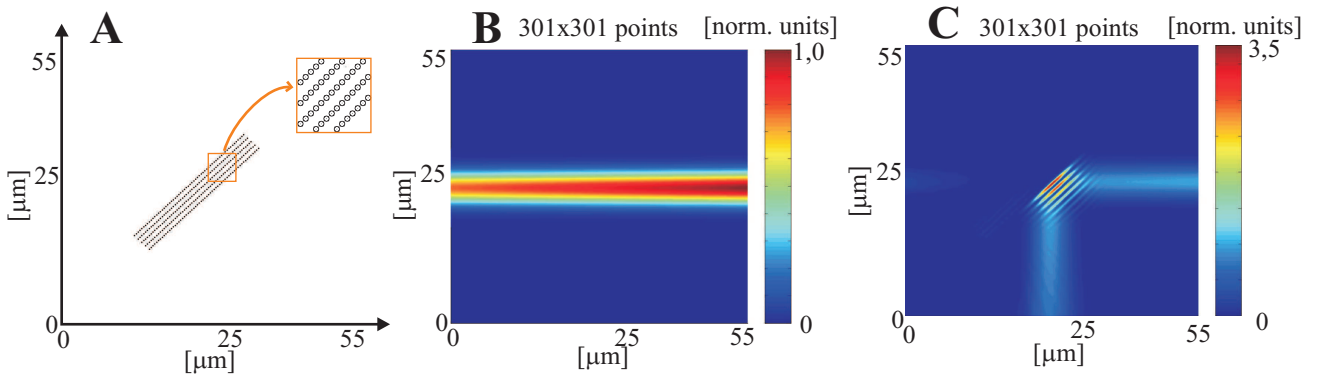


Figure 3.6: The topography (A) of the Bragg mirror consists of 5 parallel lines of nanoparticles, with a polarizability of $\phi_l = 1, 4\pi$, separated by a distance of $0,55\mu\text{m}$. The inclination of the lines is 45° from the horizontal and the separation distance between the layers is $1,10\mu\text{m}$. The incident field has a focused intensity profile with a beam waist of $3,0\sqrt{2}\mu\text{m}$ (B). The Bragg mirror clearly reflects the incident field (C).

The penetration of light through the mirror has been decreased by adding additional lines. Removing some of these would yet again result in transmission through the mirror. This phenomenon may be exploited in the construction of a beam-splitter, see figure 3.7. By

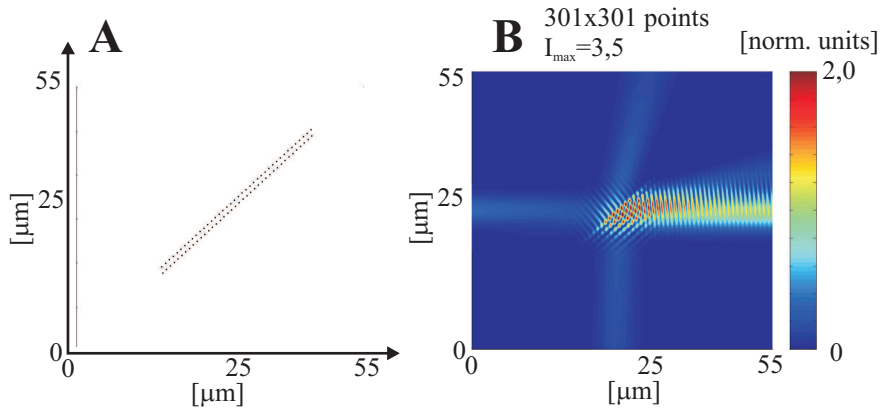


Figure 3.7: The topography (A) of the beam-splitter consists of 2 parallel lines separated by a distance of $1,10\mu\text{m}$, which is the same value for the distance between the nanoparticles. The inclination of the lines is 45° from the horizontal and the applied polarizability is $\phi_l = 1, 4\pi$. The incident field has a focused intensity profile with a beam waist of $3,0\sqrt{2}\mu\text{m}$ (B).

slightly displacing one of the lines along the line direction, the beam-splitter modelling shows an interesting phenomenon, as the beam is split into an additional third part. The maximum of the intensity scale has been lowered in order to bring out the transmitted intensity profiles.

Another micro-optical device, realizable by a certain array structure of nanoparticles, is a focusing micro mirror. The concept is to place the particles along a parabolic curve $(y - y_0)^2 = 4F(x - x_0)$ where the coordinate (x_0, y_0) is located at the bottom of the mirror,

F is the focal length and x is along the optical axis. In principle, this works for the two-dimensional case of SPP propagation in the same way as the three-dimensional case of a parabolic screen of a solar cooker, which concentrates reflected solar light at a cooking pot. Hence, at the point $(x_0 + F, y_0)$ a concentration of light is expected. In figure 3.8, these ideas are tried out for focusing micro mirrors with different dimensions. The focusing

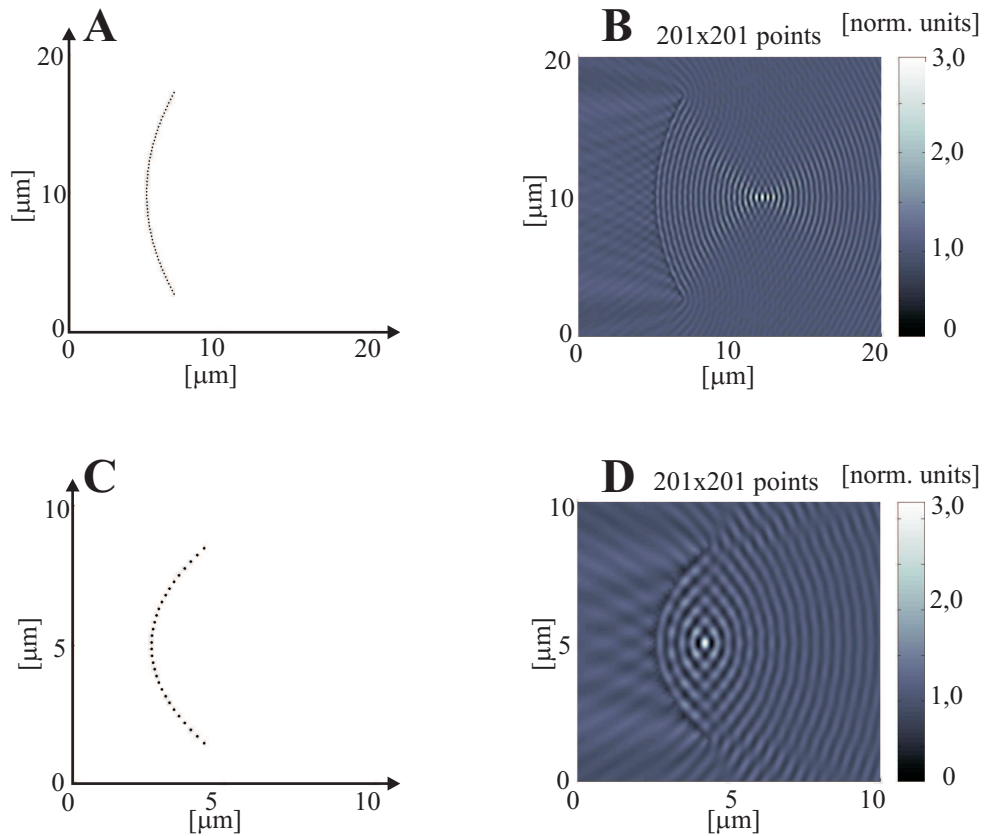


Figure 3.8: *The topographies (A) and (C) and the corresponding field intensity distributions (B) and (D) of two focusing micro mirrors with a parallel beam excitation of 740nm. The polarizability of the scatterers are set to 0,7. The separation distance of the scatterers along the y-direction is 0,25 μm , and the focal lengths are 7,25 μm (A) and 1,75 μm (C).*

leads to an enhancement at the focal point of 3 in each of the two cases, so a mirror in a larger scale with an increased amount of scatterers does not necessarily give larger signal enhancement at the focal point. However, further modelling has shown that with mirrors of similar dimensions, increased scatter density and decreased focal distance contribute to larger signal enhancement at the focal point. For application matters, focusing micro mirrors are interesting in the sense that it gives the possibility to enhance the SPP signal locally in a controllable way. For instance, this feature could be exploited, possibly in connection with a focused excitation source, to further increase the efficiency of surface enhanced Raman spectroscopy.

3.3 Simple Structures

Scattering of SPPs in simple structures of few nano-particles has been investigated. A sketch of the sample is shown in figure 3.9. The nano-particles have shown to scatter

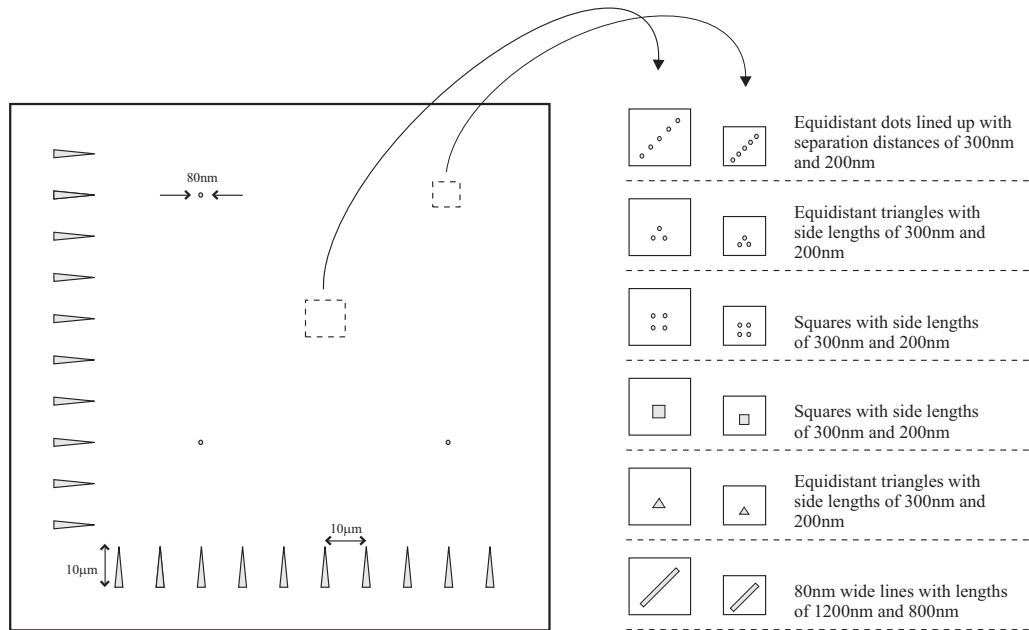


Figure 3.9: Sketch of the various simple structures included on the sample.

light inefficiently compared to other, external, scatterers. An example of this is shown in figure 3.10. It has later been discovered that the fibre tip used in these measurement has

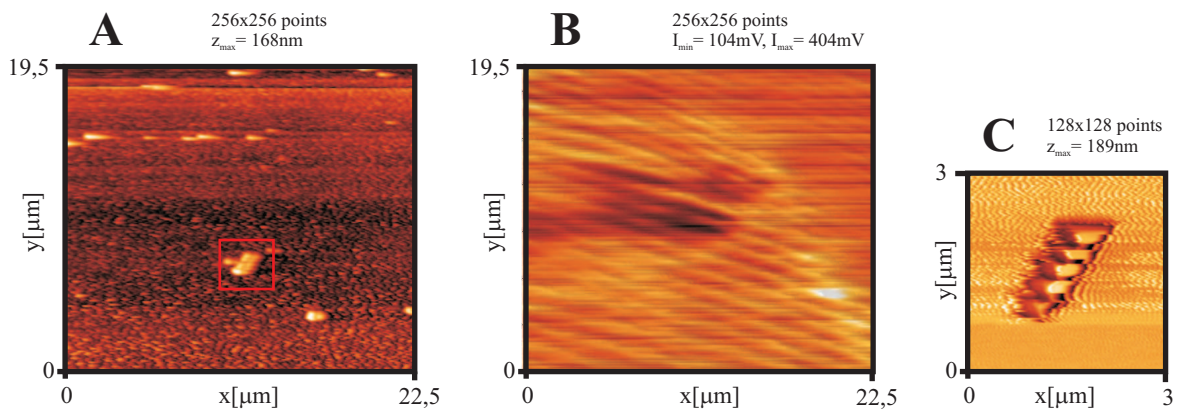


Figure 3.10: Topographical (A) and near-field optical (B) images, with a source wavelength of 727nm, of a line array of 5 nano-particles spaced approximately 0,30µm apart. A zoomed topographical image is shown in figure C.

been severely broken and therefore is unreasonably large. The consequence of this is that the lowest point of the fibre, which scans the topography, is different than the point of the fibre which picks up the optical signal thus causing a displacement between the two signals. However, regardless of a possible signal displacement, the contrast is still quite

large, and it is clearly shown that as far as the scattered field is concerned, the effect of the line array is quite poor. There seems to be an immediate effect in terms of a dark area in the proximity of the scatterer and a shadowing effect along the propagation direction, but the overall image is dominated by an externally scattered field. In general, the images which are believed to have been made with the broken fibre tip show decent topography and signal contrast, so it is likely that the features of these will not change significantly with a sharp fibre tip.

An almost similar effect has been observed elsewhere on the sample, figure 3.11, in a

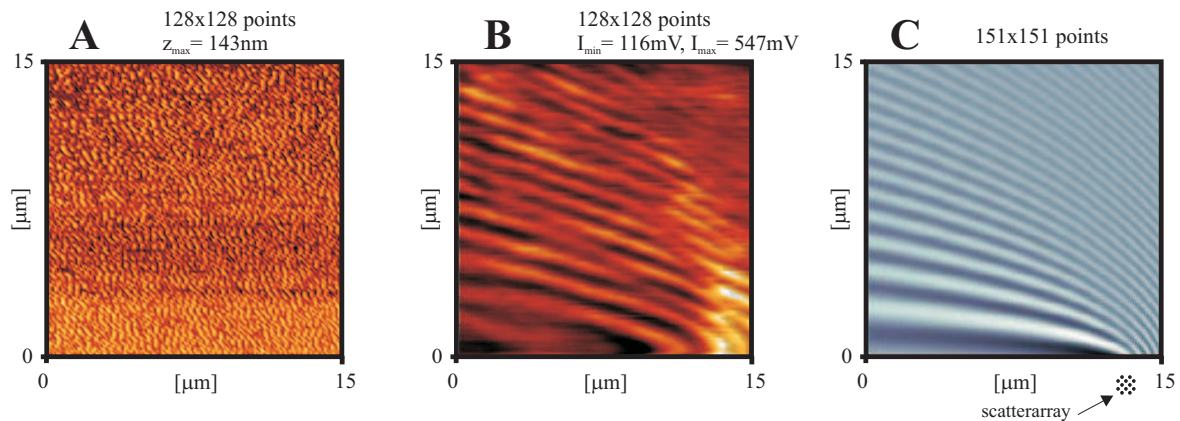


Figure 3.11: *The topographical (A) and near-field optical (B) image, with a source wavelength of 727nm, of a region of no artificially made gold nano-particles, showing the effect of a strongly scattered field from an external scatterer positioned below the image. The modelling of this (C) has been done with an array of micro scatterers with the structure and location shown in the picture.*

location relatively far from any expected artificially made micro scatterers. During the modelling process of this image, it has been assumed that the external scatterer is a defect with a complicated structure, so it has been built up by a bunch of individual scatterers, each with a polarizability of 0,7 as used in previous modelled images. In principle, this gives the approximate same result as a single scatterer with a larger polarizability. Since the topography of the defect is unknown, the defect can be either a complicated structure of weakly scattering individual particles or one large particle with a large scattering efficiency, and hence both ways of modelling seem reasonable.

The weak scattering from the artificial nano-particles permits detailed study of these scattered fields due to the regular presence of stronger scattered fields. However, it is possible to overcome this limitation by performing measurements with local SPP excitation. The focuser is then illuminating an area in front of, and in the immediate vicinity of, the area of the artificial nano-particles, thus preventing SPP scattering from external areas with possible strong scatterers.

Measurements of this kind have been performed on the line array structure whose topography is shown in figure 3.10C. Using a focused excitation beam with a wavelength of 727nm, a scattering effect from the line array is clearly seen, illustrated by the topography and near-field measurements of figures 3.12A and 3.12B, respectively. The intensity

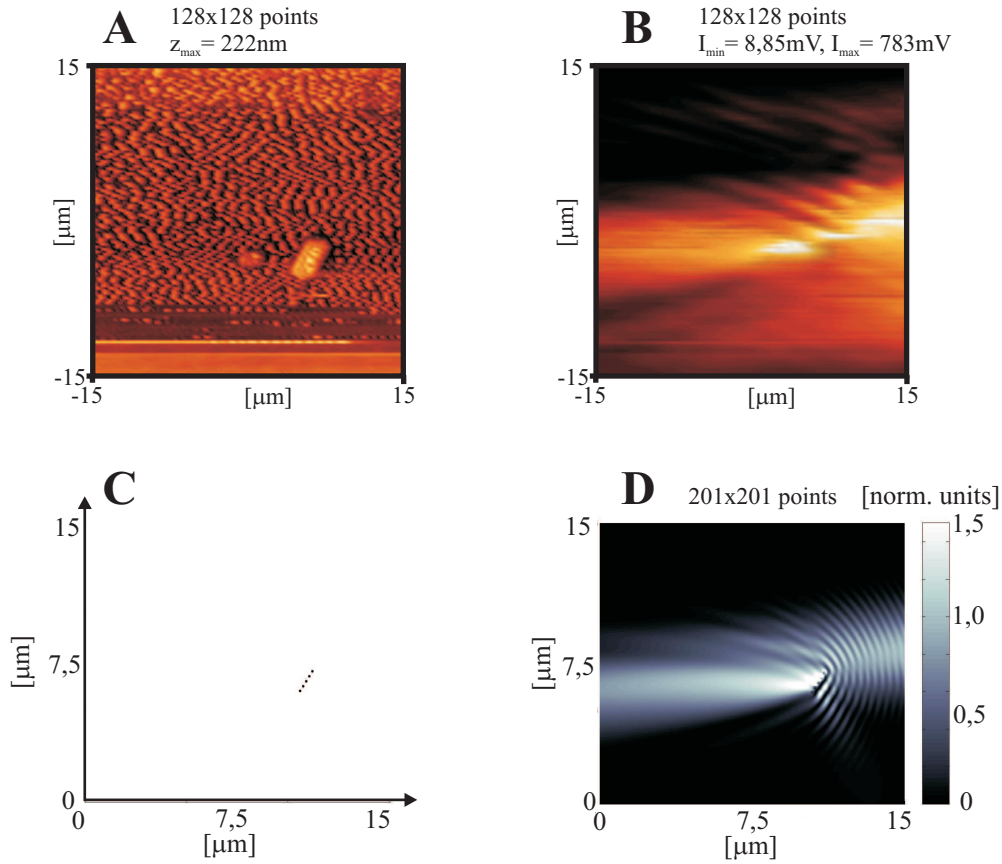


Figure 3.12: *Topographical (A) and near-field (B) measurement of a gaussian distribution of SPPs incident on a line array of nano-particles. The modelled topography (C) and near-field image (D) show a clear resemblance with the experimental result. The phase number of the polarizability has been set to $\phi_l = \pi$, the inclination of the SPP propagation direction is 7° and the beam waist of its gaussian distribution is set to $w = 2,0\sqrt{2}\mu\text{m}$ based on a cross section measurement in the experimental image.*

profile of this measurement indicates that the beam may be improperly focused due to the presence of a large uniform area in the lower half of the image. However, in the upper part the distribution seems gaussian, with a beam waist of approximately $2,0\sqrt{2}\mu\text{m}$. In the modelling of the measurement, figures 3.12C and 3.12D, the incident SPP field is assumed to be an inclined gaussian distribution of this kind. To some extent, it has been possible to reproduce the experimental image through modelling. Strikingly, both images exhibit a spot of large intensity to the immediate left of the line array and above this structure interference fringes with large periods are present. On the other hand, it is similarly clear that interference fringes from back reflection of the structure are only present in the modelled image. Suppose the modelling is reliable and that the reason to the missing interference phenomenon is due to experimental causes. An irregular shape of the tip may then provide an explanation to this, as the irregularity may prevent SPP signal detection from certain directions, in this case SPPs propagating towards the right of the image. This assumption is further supported by the near-field measurements of

figures 3.10B and 3.11B, which lack interference fringes in similar directions from the assumed scatterer. Common to all measurements is the fact that the same fibre tip has been used and that it, therefore, is possible that it has been irregularly shaped during all these measurements.

3.4 Surface Plasmon Polariton Band Gap Structures

The investigation of simple structures of the previous section is now extended to include large periodic arrays of nano-particles making up surface plasmon polariton band gap structures.

In the subsequent sections, SPP propagation in triangular and quadratic structures are investigated by means of modelling and SNOM measurements. The propagation direction with respect to the orientation of the structures is denoted by the special points along the edge of the irreducible Brillouin zone, see figure 3.13. All SNOM measurements of

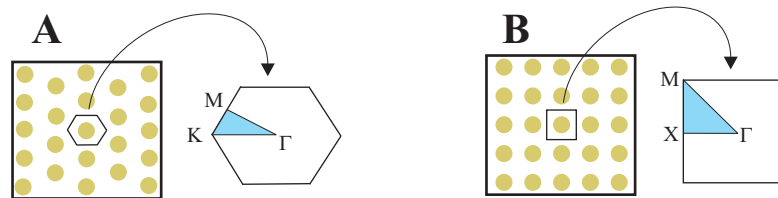


Figure 3.13: *The lattice structures and Brillouin zones of a triangular (A) and quadratic (B) lattice structure. The blue shaded area represents the irreducible Brillouin zone which is the smallest region not divisible by symmetry considerations.*

SPPBG structures with an applied focused beam are performed with "middle excitation".

3.4.1 Optimization of Computation

Calculations of near-field images of many particle structures have shown to require demanding computation power. By analyzing this computation process, reasonable approximations can be introduced in order to greatly enhance the calculation efficiency. These are described and investigated in the following.

The calculation primarily consists of two major processes, one for the computation of the self-consistent fields at the sites of the scatterers and one for the summation of field contributions at each specific location coordinate at the surface plane. These processes are related to the expressions in (3.5) and (3.3), respectively. The flowchart diagram of figure 3.14A illustrates the straightforward way of implementing these processes in a whole. The preliminary calculations include, among other things, the construction of a coordinate array containing the locations of the scatterers and the field component distribution of the incident field. Compared to the other computation processes, these calculations are performed instantly.

As previously mentioned in this chapter, the matrix calculation of the self-consistent

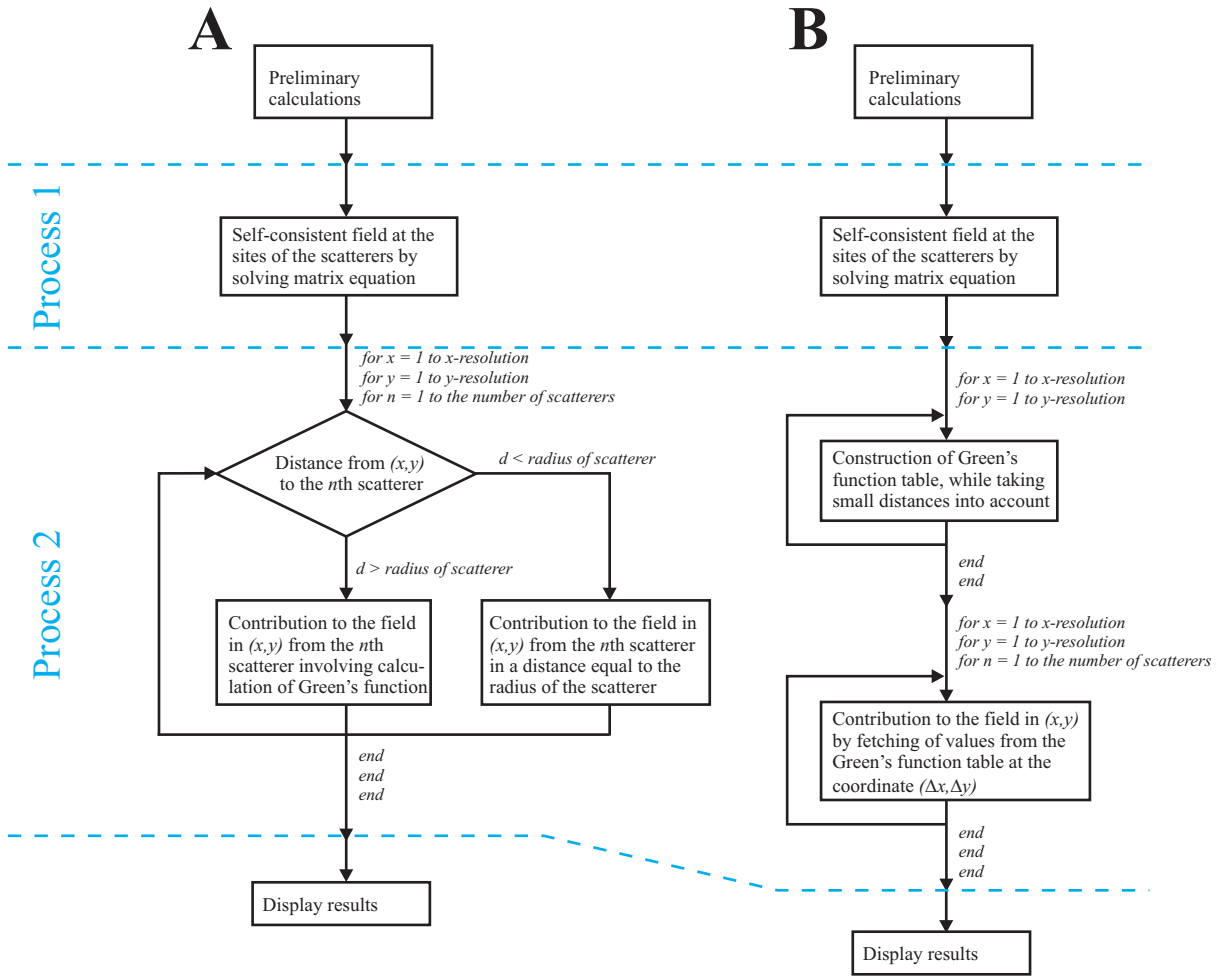


Figure 3.14: Flowcharts demonstrating two different constructions of the computing process. The straightforward program structure (A) involves numerous computations of the Hankel function, whereas an alternative approach (B) avoids this by means of tabulation.

fields is not a demanding process, not even for a considerable amount of scatterers, so optimization of Process 1 is not being thought of.

In Process 2, the field at each surface coordinate is found by the sum of the term $\alpha_j E(\mathbf{r}_j) G(\mathbf{r}, \mathbf{r}_j)$ calculated for each scatterer. The Hankel function, included in the Green's function, is due to its summational form apparently a quite demanding operation for the PC. This operation is performed many times due to its presence in the inner loop, significantly decreasing computation efficiency. For instance, computation of the field intensity with an image resolution of 200×200 points in a structure of 200 scatterers will roughly require 200^3 of these demanding operations. An improvement to this is to replace the Hankel function with the far field approximation shown on page 28 in the computation of the Green's function. This improvement gives a threefold increase in computation efficiency. However, even with this approximation, the bottleneck for faster computation is still aimed at the continuous calculation of the Green's function in the inner loop. Hence, additional approximations are introduced for even further improvements.

The basic approach is to perform tabulation of the Green's function, illustrated by the flowchart sketched in figure 3.14B. Prior to the calculation of the field distribution, a two dimensional array A_G with elements $A_G[n_x, n_y] = \alpha G(C\sqrt{n_x^2 + n_y^2}\beta, 0)$ and dimensions corresponding to the image resolution is constructed. n_x and n_y are positive integer values and C is a conversion factor. For each surface coordinate, the field is then calculated by the sum of individual products of $E(\mathbf{r}_j)$ and $A_G[|\Delta n_x|, |\Delta n_y|]$. $|\Delta n_x|$ and $|\Delta n_y|$ are integer values representing the coordinate distance of the j th scatterer from the surface coordinate along each of the axes. In summary, the computing of the individual field contributions is not made by a rigorous Hankel function operation or by calculation of the large expression for the far-field approximation. Instead, the contribution is computed by fetching a value from the A_G array, at the point corresponding to the rounded coordinate distance between the surface point and the proper scatterer, and thereafter multiplying with $E(\mathbf{r}_j)$, which has been calculated in Process 1 thereby similarly fetching this from an array.

Naturally, exceptions must be introduced for scatterers located outside the image region as this eventually may lead to large distances to the scatter source and thereby attempted fetching of values located at coordinates which are out of range of the A_G array. A possible future solution to this, assuming the external scatterers are placed within a fair vicinity of the image region, could include a sufficient enlargement of the A_G array. This only needs to be made once for each image computation and therefore will not affect overall performance. Still, while doing this, it should always be borne in mind that handling of very large memories may severely affect the computation efficiency.

A performance test of the various computation methods has been carried out. These methods are now summarized as "the straightforward way", "usage of far-field approximation" and "tabulation of the Green's function" denoted as Method A, Method A1 and Method B, respectively. The results are shown in the following table.

Resolution	Number of scatterers	Process 1	Method A	Method A1	Method B
101 × 101	25	40 ms	29 s	9 s	0,75 s
101 × 101	200	1,9 s	3,7 minutes	66 s	2,8 s
201 × 201	50	90 ms	3,7 minutes	68 s	4,6 s
201 × 201	400	11,4 s	30 minutes	9,3 minutes	21 s
801 × 801	200	1,9 s	3,9 hours*	1,2 hours*	10 minutes
801 × 801	1600	8 minutes	31 hours*	9,2 hours*	35 minutes

* *These values have been found by computing only a fraction of the image.*

The computer used as test bench is an Athlon XP 2400+ running at 266MHz bus speed with sufficient, 512MB, DDR PC2700 RAM. It is quite striking that there is more than a tenfold increase in computation efficiency with the use of tabulation methods compared to the other two. Method B is, therefore, by far the preferred choice for future computations. The only possible concern is the inaccurate fetching of values due to the necessity of rounding the coordinate distances between the scatterers and the proper location. In order to investigate this further, test images calculated by the correct and the tabulated method, respectively, are compared, see figure 3.15. Despite a slight difference in the maximum intensity, the images seem indistinguishable, so Method B remains the preferred choice of computation method. Finally, it should be noted that certain conditions may

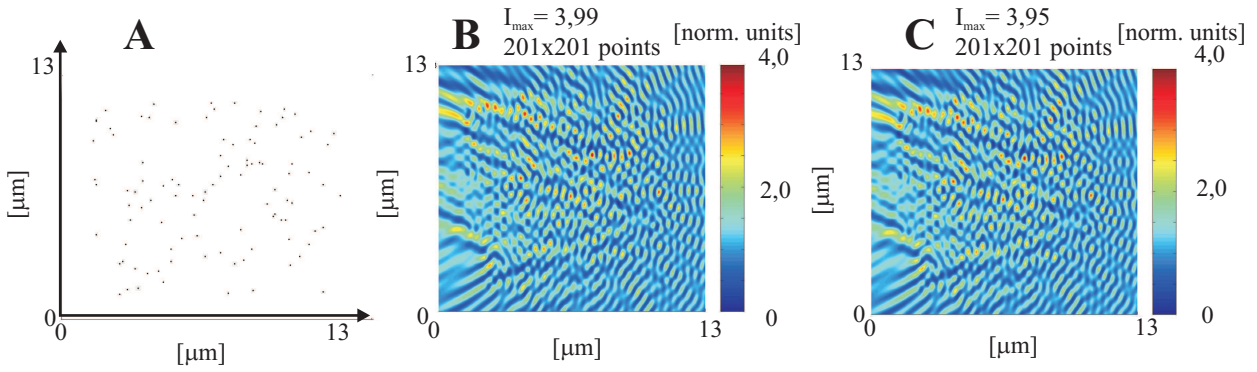


Figure 3.15: *Topography (A) of 100 nano-particles which are randomly distributed. The near-field images have been calculated by means of Method A (B) and by Method B (C). The polarizability is 1 and the source wavelength is 727nm.*

apply for the image modelling in a periodic structure, by which the approximation of Method B significantly affects the result. It is possible that slight deviations from the exact contribution from each scatterer may add up due to the periodicity thus giving an overall large deviation. Small inaccuracies in the argument of the Green's function may affect the result even for a small number of contributions. This situation is imagined if the scatterers involved in the proper calculation are located in an area of locally enhanced self-consistent fields. However, as long as modelled images of symmetric structures exhibit indistinguishable symmetry along the median optical axis this statement is not being taken further into account. In any case, whenever possible, the scatterer coordinates are presented by whole numbers, which for certain common structures, such as triangular lattice arrays, is impossible.

3.4.2 Triangular Structures

Prior to any presentation of experimental images, the modelling is tried out on various types of band gap structures. A previous work of modelling of triangular structures of gold nano-particles [10], using the same self-consistent model, serves as inspiration source for the starting point of the modelling process. Eventually, the procedures carried out in the previous work are compared to alternative approaches and discussed in order to provide a better basis for subsequent SPPBG structure modelling. The structure of investigation is shown in figure 3.16A. A wavelength range of interest in this modelling is the wavelengths lying within the band gap. For these wavelengths, penetration of the incident light through the structure is forbidden. A measure of the extent of the band gap is thus to consider the reflectivity from the structure. A method of doing so includes contrast calculations of the interference fringes in front of the structure, since increased interference between the incident and reflected light involves higher contrasts. In the case of the cross sectional intensity profile of an interference fringe, the contrast is defined as the difference between the peak and bottom intensity divided by their sum. The contrast can be related to the analytical expression

$$|Ae^{ikx} + Be^{-ikx}|^2, \quad (3.7)$$

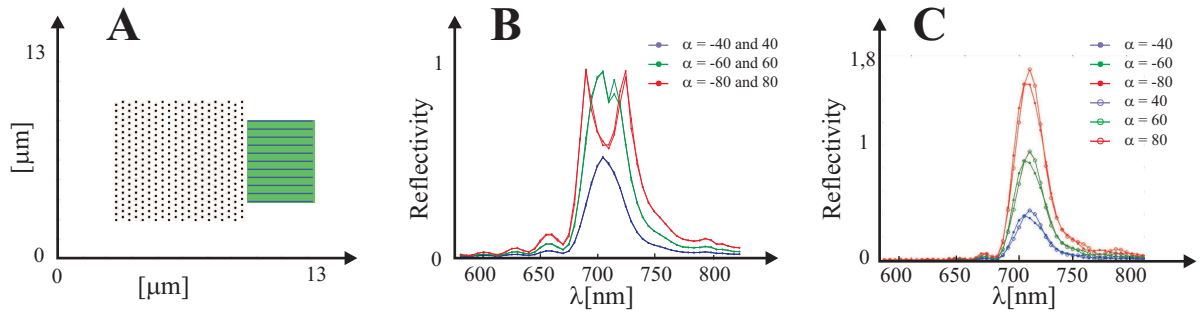


Figure 3.16: Topography (A) of 400 gold nano-particles arranged in a triangular lattice structure oriented for SPP incidence along the ΓK direction and with a lattice constant of 400nm. The blue lines located in front of the structure are contrast lines of which the reflectivity is calculated for various polarizations (B). The green area represents an area of integration applied in an alternative approach to reflectivity calculation, which is shown for similar polarizations (C).

which represents the intensity at a location x containing the incident, amplitude A , and reflected, amplitude B , light. Following the above definition, the maximum and minimum of the intensity is found, and the contrast is eventually expressed as

$$\text{Contrast} = \frac{I_{max} - I_{min}}{I_{max} + I_{min}} = \frac{4AB}{2(A^2 + B^2)}, \quad (3.8)$$

with two solutions to the reflected amplitude

$$B = A \frac{1 - \sqrt{1 - \text{Contrast}^2}}{\text{Contrast}} \quad \text{and} \quad B = A \frac{1 + \sqrt{1 - \text{Contrast}^2}}{\text{Contrast}}. \quad (3.9)$$

The first solution with the subtraction of the two terms in the nominator is valid when $B \leq A$ and is therefore the physically interpretative solution. The 11 blue lines in front of the structure in figure 3.16A represent the cross sections from which the contrasts are calculated and the average reflectivity is found. After many unsuccessful attempts, reflectivity graphs similar to those of the previous work have finally been calculated, see figure 3.16B as well as replica of the previously calculated images, figure 3.17. The reason

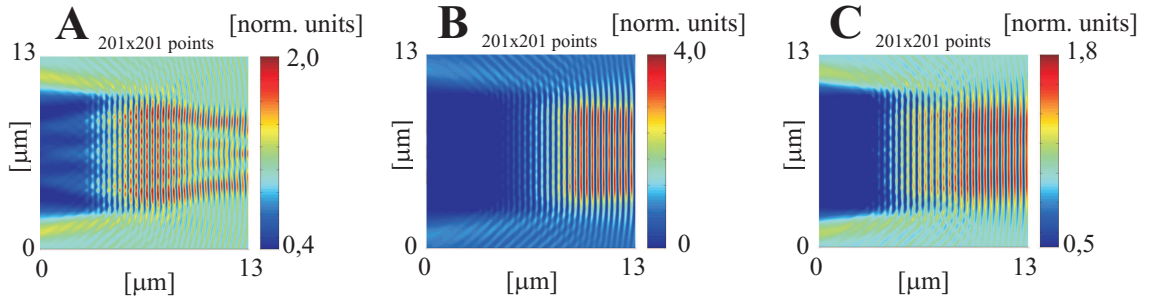


Figure 3.17: The near-field images have been calculated differently than usual with source wavelengths of 670nm (A), 710nm (B) and 750nm (C). The applied dielectric constant is $-24 + 1,6i$, and the polarizability has been set to -60 .

to the experienced troubles is that it eventually has been discovered that the calculation

of the self-consistent fields in [10] are based on the equation $\mathbf{E}_0\mathbf{E}^T = \overleftarrow{u} - \overleftarrow{G}$, omitting α , and not on the supposed expression in (3.5). Based on these revelations, it is assumed that the calculations of the previous work have been carried out somewhat incorrectly which explains the unreasonably large polarizabilities.

An alternative approach to reflectivity calculations of the modelled images is to calculate the average intensity of an area in front of the structure followed by a subtraction of the incident field intensity. Such an area is sketched as the green area in figure 3.16A and the results of reflectivity calculations, performed for the same parameters as with the contrast method, are shown in figure 3.16C. It is clearly demonstrated that the reflectivity exceeds the intensity of the incident field for very large or very small polarizabilities. After some thought, the result is found expected due to the lack of α in the calculation of the self-consistent field and the individual scatterer contributions are then simply increased, proportional to the value of the α parameter. Calculation of the average intensity in an area is a safe measuring method and works well as long as the value of the incident field is known. For this reason, it is contradictory that the graphs for $|\alpha| = 80$ in figures 3.16B and 3.16C are so different. The reason is believed to be found in the choice of the calculation method of the reflectivity, including B . For the meaningless, but yet present, situation where B becomes larger than A , only the second solution of (3.9) is applicable. The calculations behind some of the graphs shown in figure 3.16B, have not taken this into account and are therefore considered incorrect.

Nevertheless, from an experimental point of view, where A is always larger than B , except for possible local bright spots, the contrast method of (3.9) works excellent for analyzing images where the incident field intensity may be unknown. Without further knowledge in advance of the incident intensity, substitution of A , from the difference term in the nominator of (3.8), into the first equation of (3.9) yields an expression which solely depends on measurable quantities

$$B^2 = \left(\frac{I_{max} - I_{min}}{4} \right) \frac{1 - \sqrt{1 - \text{Contrast}^2}}{\text{Contrast}}. \quad (3.10)$$

However, during the modelling and testing phases, unreasonable results leading to a reflectivity larger than 1 may not be discovered until the very images are modelled, if the reflectivity reading is based on (3.10). Based on this, and on the incident field intensity being a known parameter, reflectivity calculations by means of either the intensity difference

$$B = \frac{I_{max} - I_{min}}{4A}$$

or by average intensity reading of an area, are henceforward considered the safe choice.

Reflectivity graphs have been made for the same wavelength range and triangular structure as previously, now using the supposed method of modelling. In addition, the transmittance through the structure is now calculated in a similar manner as the reflectivity, by calculating average intensity in an area immediately after the structure. This is due to the discovery that for certain polarizations, by which the reflectivity exhibits a clear band gap behavior, the average transmittance in some ranges is contradictory large, in

some cases more than unity, which is unreasonable. Based on this, the preferred polarizability is the value for which a band gap is seen both by reflectivity and transmittance calculations and, in addition, these intensities should not be larger than the incident field intensity for any wavelength in the range of investigation. Calculations have shown that these introduced requirements prohibit any phase number values ϕ_l , introduced on page 31, and any positive real values of the polarizability, at least in this case. However, for a small range of negative polarizability values the above requirements are satisfied, see figure 3.18. Based on these calculations, modelled images of the structure for source wavelengths

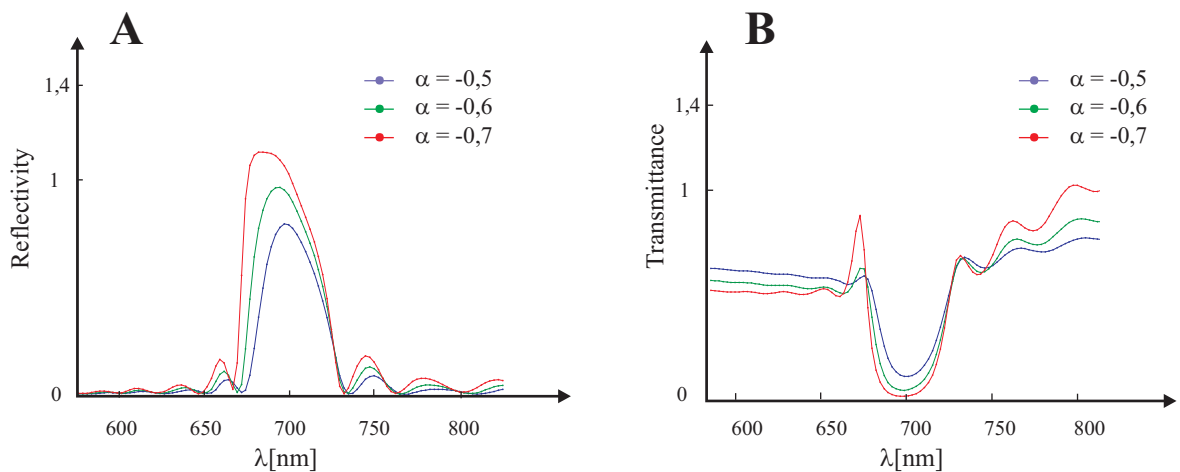


Figure 3.18: Reflectivity (A) and transmittance (B) calculations for small negative values of α indicate the presence of a band gap.

around the band gap are presented in figure 3.19. The calculations reveal a band gap at

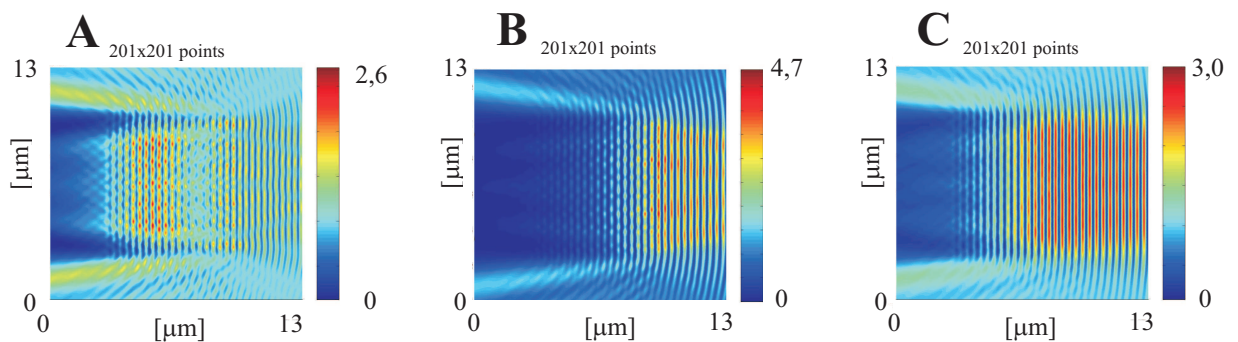


Figure 3.19: Representations of the field intensity distribution for SPP propagation in the structure shown in figure 3.16A. The source wavelengths are 660nm (A), 690nm (B) and 720nm (C) and the polarizability of the scatterers has been set to $-0,6$.

approximately 690nm, close to 710nm found for the incorrect calculations, and these two images are quite similar in appearance except for a slight difference for the interference fringes in front of the structure. Strikingly, the characteristic interference pattern of figure 3.18B, i.e. the uneven intensity distribution along the vertical direction in front of

the structure, shows superior resemblance with previous experimental results of a similar structure presented in [10][page 244], performed with a excitation source wavelength of 782nm, however.

An appearing feature for some wavelengths is the presence of resonances leading to large field intensity distributions within the structure. This is demonstrated by the image in figure 3.18A. Based on the notion of a resonating cavity, it is suggested that the equal dimensions, in terms of the number of scatterers, along the horizontal and vertical directions of the structure, respectively, may cause this behavior. However, investigations show a similar image for a oblong structure, figures 3.20A and 3.20B, so this suspicion is rejected.

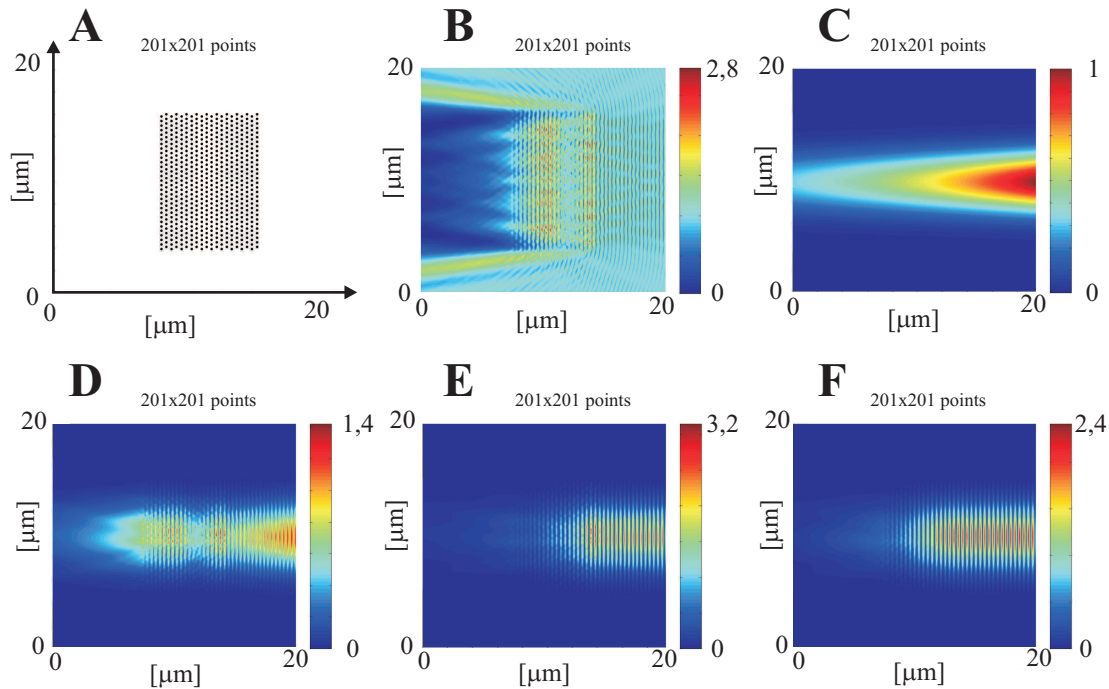


Figure 3.20: *Topography (A) of an triangular structure oriented for SPP incidence along the ΓK direction and with a lattice constant of 400nm. The remaining optical images of this figure correspond to this topography. B: Calculated field intensity distribution with a source wavelength of 660nm. Focused excitation light is applied, shown here (C) for 690nm and with a beam waist of $2,5\sqrt{2}\mu\text{m}$. The field intensity distribution for focused excitation light has been calculated for 660nm (D), 690nm (E) and for 720nm (F).*

Since the previous chapter of this project has dealt with a focused excitation beam, it could be interesting to investigate this by modelling gaussian SPP intensity profiles in these SPPBG structures. This has been tried out for the same wavelengths as for the parallel beam excitation in figure 3.19. The results are shown in figures 3.20C, 3.20D, 3.20E and 3.20F. A comparison of these images with the others of parallel beam excitation reveals reflectivity patterns which are quite similar. A noticeable feature, however, is the decreased maximum intensity for images of the gaussian incident profile. The reason to

this lies in the decay of the excitation beam along the optical axis, which clearly causes lower intensity of the reflected and incident light.

This section is rounded off by a demonstration of the effects of SPPBG structures on large scale images, see figure 3.21. The SPPBG structure of investigation is the same as

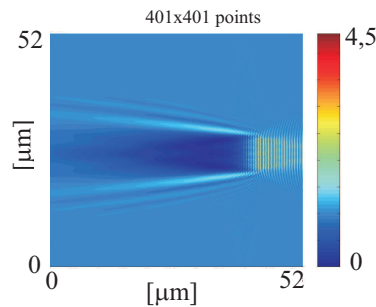


Figure 3.21: *Modelling of the large scale effects on the field intensity distribution by a triangular SPPBG structure, located to the right in the image.*

in figure 3.16A, with an imaging range increased fourfold to $52 \times 52 \mu\text{m}$. In order to better demonstrate the decaying effects, the damping term in the dielectric constant has been doubled. This action may not only be justified for illustrative purposes. For a gold film thickness of around 53nm, an additional decay of backscattered radiation of approximately the same size as the natural decay caused by the ohmic resistance in the metal should be present, see appendix D. Eventually, to the far left of the structure, the intensity distribution is roughly unaffected by the SPPBG structure. This regain in incident field strength should not be, at least in this modelling, related to the situation of a rebuilt SPP field immediately after the structure, as discussed in chapter 2. The particular reason is exactly due to the decay, thereby limited range, of the scattered, perturbing, field.

3.4.3 Quadratic Structures

The experiences gained from modelling of triangular SPPBG structures in the previous section set the scene for modelling of quadratic SPPBG structures. Experimentally obtained images will provide an obvious opportunity in terms of comparison and modelling imitation attempts.

Near-field measurements of SPP propagation on a gold film with gold nano-particles arranged in quadratic array structures, oriented in the ΓX -direction, with an approximate lattice constant of 400nm have been performed for a variety of wavelengths. The sample is sketched in figure 3.22. In comparison, the reflectivity and transmittance from such a structure have been calculated and the field intensity distribution has been modelled, see figure 3.23. The reflectivity calculations reveal jagged curves in contrast with the previous reflectivity representations. It is assumed that the reason is the presence of bright/dark spots in front of the structure of rapidly changing reflectivity patterns, which either lowers or raises the minima and maxima of the interference fringes. In summary, there are pros and cons of both reflectivity calculation methods. Whereas integration of

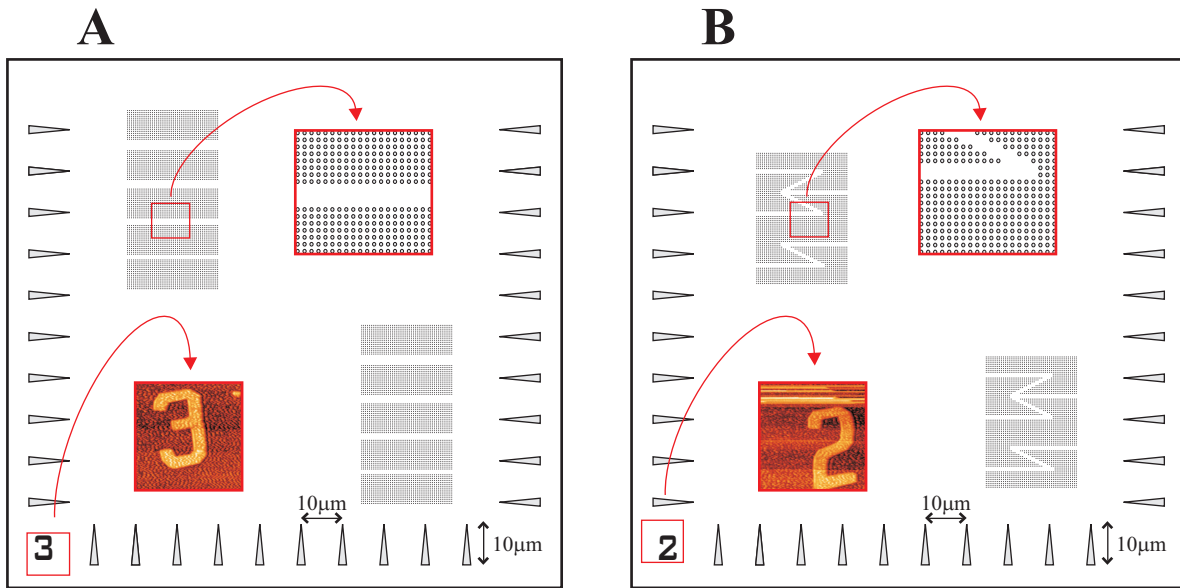


Figure 3.22: Sketch of the two SPPBG structures included on the sample - one with straight (A) and one with curved waveguides (B). Indicators in terms of numbers, shown with two examples of obtained topography measurements, assist in locating areas of interest.

an area in front of the structure is slightly more time consuming, and is reliable only in structures which are sufficiently wide [22], it tends to return more continuous reflectivity representations. The difference may be compensated for by introducing more lines in the contrast measuring method - however, this is done at the possible cost of equalized calculation times.

Experiments

As a first approach, the quadratic structures are investigated experimentally with the purpose of demonstrating the band gap effect. From the previous modelling, it seems that an obvious method of doing so is to measure the maxima and minima of the interference fringes in the expected reflectivity pattern in front of the structure and incorporating this into (3.10). However, in the measurements, clear presence of these interference fringes is missing, rendering the contrast method useless. Instead, the measurable penetration of SPPs into the structure is used, thus relating this to the band gap effect, since reduced transmittance into the structure is expected around the band gap. Based on measurements with focused excitation of varying wavelengths, 13 penetration profiles are at disposal for data analysis. An example of one of these measurements is shown in figure 3.24. For each penetration profile, 11 sub profiles are measured, summed and normalized. Three of these profiles are displayed in figure 3.25A. The sudden large intensity at the area around the edge of the structure may be related to inelastic scattering. Hence, it is attempted to avoid these areas upon the fitting of the profiles. Since only part of the graphs exhibit exponential behavior, the straight lines along the profiles demonstrate the determined valid, exponential, range of values applied for fitting. Using the usual convention for

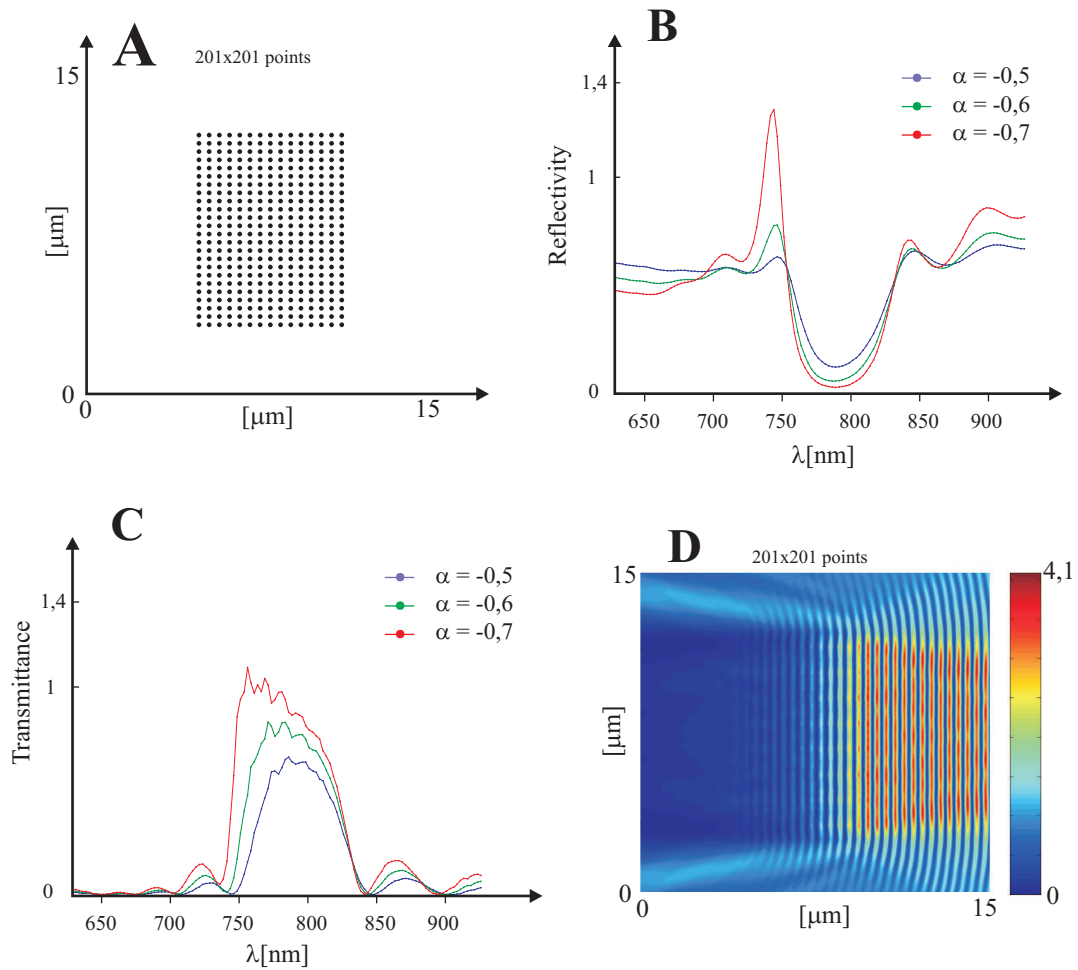


Figure 3.23: The topography of a quadratic array structure (A) applied in the transmittance (B) and reflectivity (C) calculations. Based on these calculations the field intensity distribution at the band gap, with a source wavelength of 790nm and polarizability of the scatterers of $-0,6$, has been modelled (D).

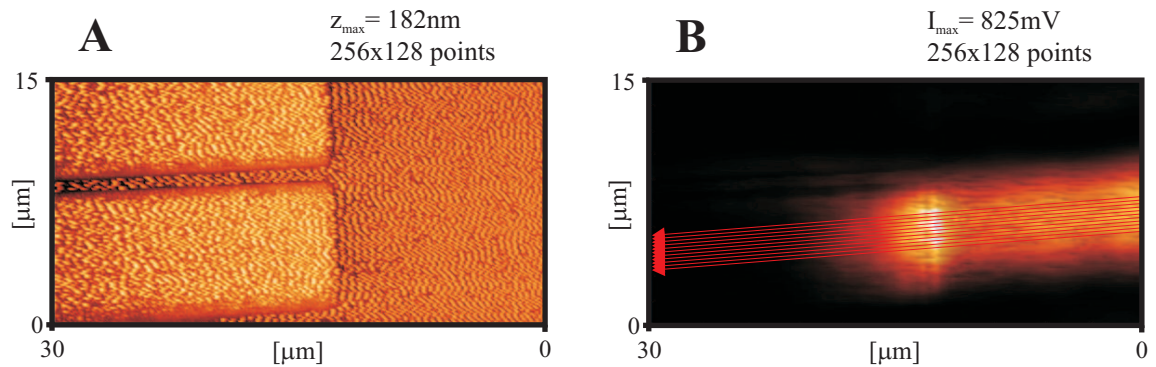


Figure 3.24: Topography (A) and SNOM (B) measurements of a focused profile of SPPs, excited at 842nm, incident on the wall of a quadratic structure. The red arrows denote the penetration profiles.

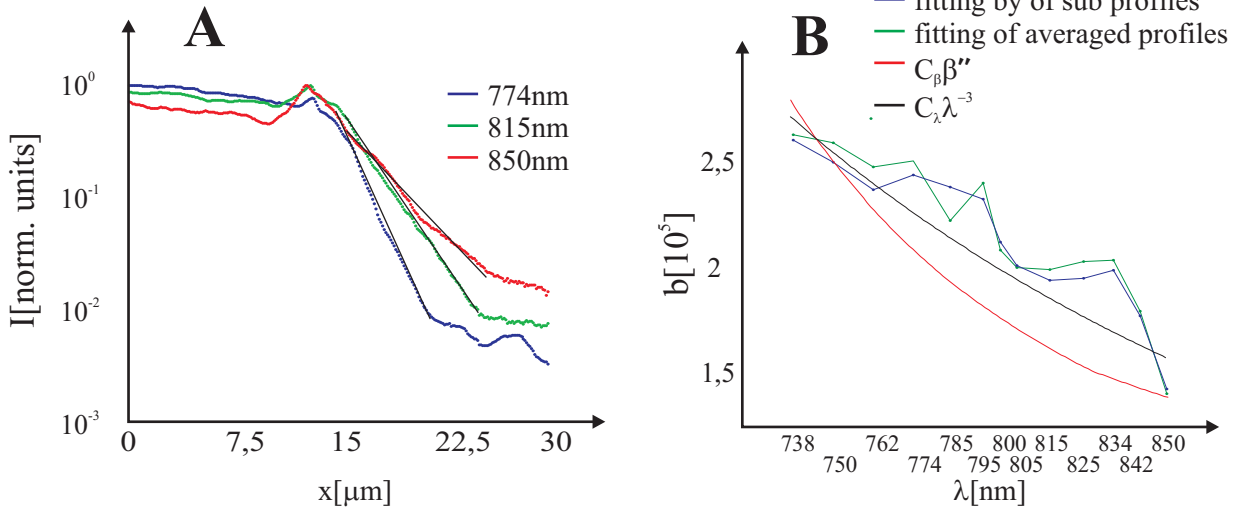


Figure 3.25: *Three averaged intensity profiles (A) of scans similar to that of figure 3.24. Wavelength dependency of the damping term (B) based on two types of fitting procedures of the intensity penetration profiles. The black and red curves denote two dependencies providing explanations to the decaying tendency of b .*

the average intensity attenuation [4], $I(x) = I_0 e^{(-2xb)}$, where b is the damping constant, fittings of the intensity profiles have been performed with I_0 and b as fitting parameters. This procedure has been carried out, by means of an automated fitting procedure, in two different ways. One, which fits each of the 11 individual normalized sub cross sections for each wavelength returning the average value of b , and another which simply fits the average normalized cross section for each wavelength. The reason to this is based on the notion that an increased number of fittings may yield more reliable results. On the other hand, however, an averaged intensity profile is expected to be more smooth than the individual ones. The results of these operations are displayed in figure 3.25B. It is observed that the two ways of fitting yield somewhat similar results expect for a slightly smoother curve in the case of individual fittings of sub intensity profiles.

In relation to this, it should be mentioned that slight deviations in the valid intensity profile range, whose determination is based on human perception, might significantly affect the fitting results. As a consequence of this, it is intended to determine ranges which are small and sufficiently far from observed non-exponential behaviors. For the same reason, one should be careful in ascribing any significance to the two risings along the b -curve. The choice of slightly different ranges of values for intensity profiles at these wavelengths, which could be justified, could yield results of b which, to a certain extent, reduce the risings.

Nevertheless, it is quite clear that the penetration damping is consistently decreased for rising wavelengths. Relating the obtained b term to the localization length $\xi = \frac{1}{b}$ gives ξ -values ranging from approximately 4 to $7\mu\text{m}$. This is comparable with previously obtained results of SPP propagation in tight random arrays of nano-particles [3, 4].

Based on these similarities the following situation is imagined; suppose the large SPP decay within the structure is not related to any resonance condition leading to a band gap effect, as studied theoretically previously. Instead, suppose the damping is entirely related to the multiple deflections in the travelling path of the incident SPP field caused by the large concentration of scatterers. With less internal and/or radiation damping, a SPP quantum will "survive" longer during the multiple scattering process, leading to a larger penetration depth. This diffusion-like idea is supported by the similarity between the fitting values of b and the damping term of freely propagating SPPs, see the red line in figure 3.25B with $C_\beta = 16$.

A similar approach to the explanation of the decaying penetration damping term, or rising localization length, along the wavelength axis, is to consider the scattering cross section, whose wavelength dependence for two dimensional scattering in random media goes as $\sigma \approx \lambda^{-3}$ [2]. This dependence is shown as the black curve in figure 3.25B with $C_\lambda = 1,05 \cdot 10^{-13}$.

As an alternative experimental approach, similar measurements of the quadratic band gap structure with a parallel excitation beam have been performed at three different wavelengths, figure 3.26. As with the previous measurements with a focused excitation beam, a possible contribution to the high intensity areas at the front edge of the structure are ascribed to inelastic scattering. As for the previous case, fitting is performed for the estimated range of values which exhibits exponential behavior. An example of one of the cross sections is shown in figure 3.27. The fitting procedure has been carried out yielding the results shown in the following table.

λ_0	b
727nm	$2,0 \cdot 10^5 \text{m}^{-1}$
795nm	$1,4 \cdot 10^5 \text{m}^{-1}$
850nm	$1,3 \cdot 10^5 \text{m}^{-1}$

The decaying tendency of the penetration damping term b with increasing wavelengths fits nicely to the other results of this section, however, the values are generally smaller. In relation to this it has been noticed that the penetration profiles of these measurements generally exhibit less pure exponential behavior. Since the beam is parallel, all incident field components lie within the TIR range and no propagating components are expected. Instead, a continuous excitation of the SPP field inside the structure, either in between or on top of the scatterers, with a uniform intensity distribution throughout the SPPBG structure, is suggested as the reason to this. Future further investigations of this could involve another fitting procedure, which takes the additional, assumed SPP, field into account. Hence, expressing the measured field along the optical axis x , yields

$$I(x) = |E_{SPP} + E_{ex}|^2 = |Ae^{i\beta x} e^{-bx} + Be^{i(k_1 x + \phi)}|^2,$$

with the incident, amplitude A , and continuously excited, amplitude B , field. k_1 and ϕ may be set to β and 0, respectively, in the case of an assumed additional SPP field.

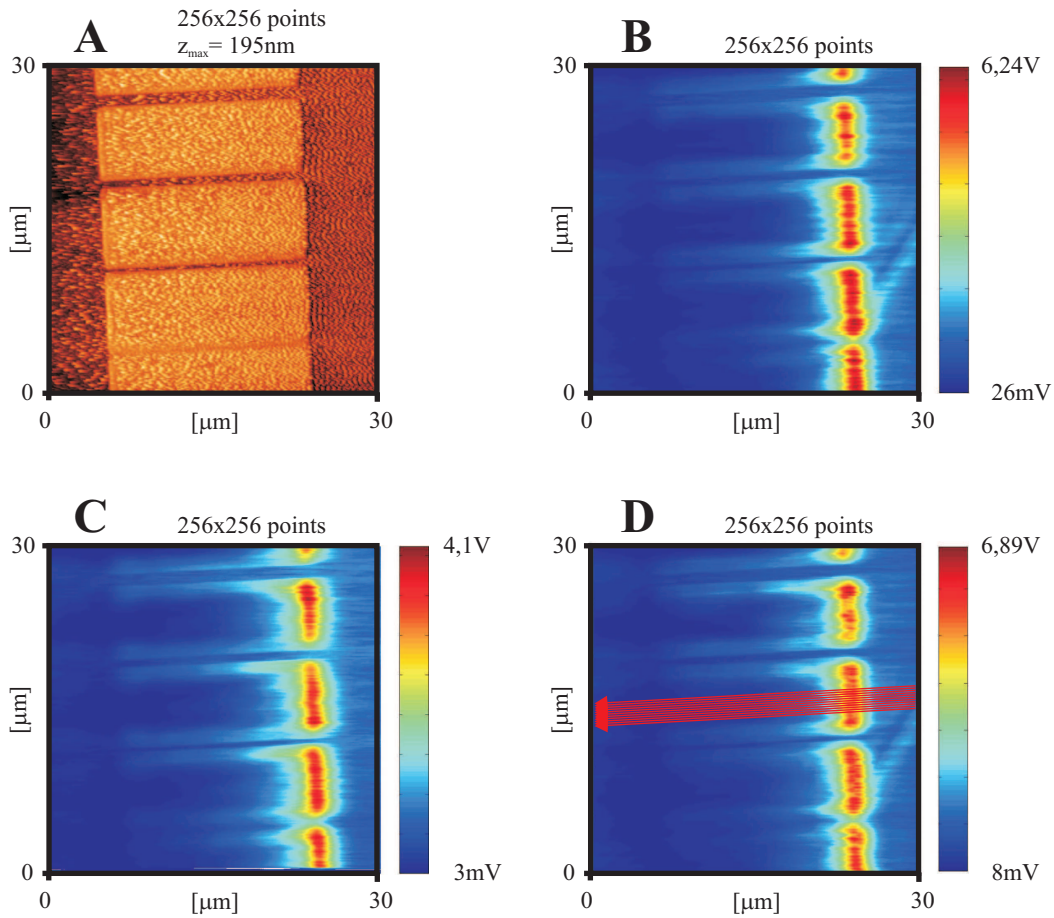


Figure 3.26: Topography (A) of the measured array structure. The field intensity distributions are shown for 727nm (B), 795nm (C) and 850nm (D). The red arrows denote the penetration profile measurement.

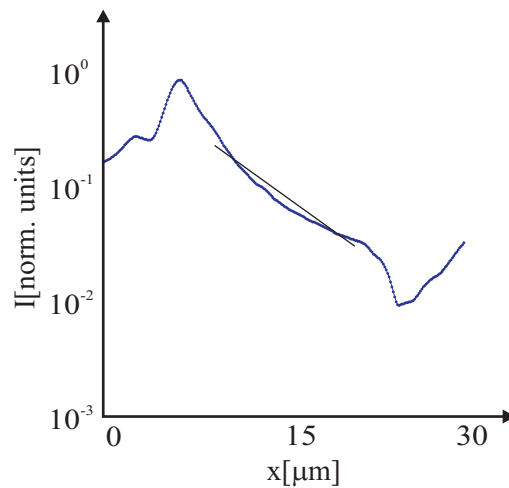


Figure 3.27: Cross sectional penetration profile along the optical axis for the 795nm wavelength scan of figure 3.26C. It is interesting to notice how the field is being rebuilt after the structure at $x = 25\mu\text{m}$.

3.4.4 Waveguide Structures

The results of the scans of figure 3.26 are used to study the waveguiding properties along the channels of missing particles. Generally, the scans exhibit a behavior of strong light confinement along the edges of the channels. A similar behavior has appeared for SPP propagation along lines in a triangular structure of ΓM orientation. During the modelling process, this phenomenon has appeared for relatively many values of the ϕ_l number ranging from $1,2\pi$ to $1,7\pi$. The modelled field intensity distribution for one of these values is shown in figure 3.28. This image shows some resemblance with the experimental in

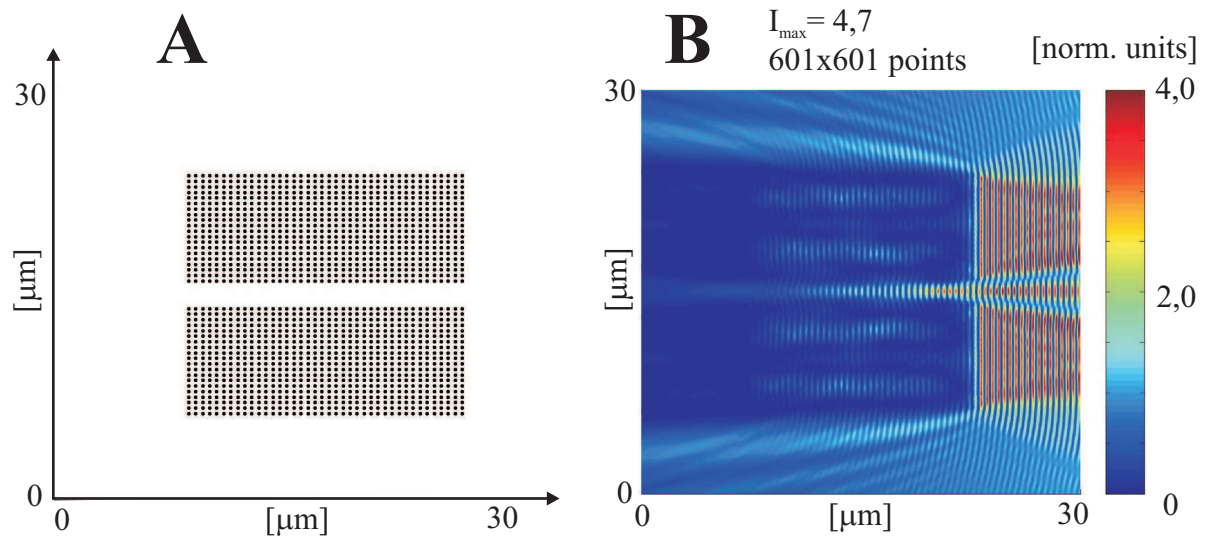


Figure 3.28: *A: Topography of 1600 scatterers arranged in a quadratic SPPBG structure with approximate similar dimensions, lattice constant 400nm, as the structure investigated experimentally, recall the sketch in figure 3.22A. The field intensity distribution (B) at an excitation wavelength of 800 nm has been calculated based on a value of ϕ_l of $1,5\pi$.*

terms of the light confinement along the channel edges albeit the experimental channel lines lie closer to the edge. However, the characteristic interference pattern in front of the structures is not recognized.

Experiments

Further experimental investigations of the light lines along the channel edges have been carried out by performing high resolution SNOM measurements at the end of the widest channel line, see figure 3.29. The image clearly shows light propagation emitted from the channel. In addition, it is interesting to notice the immense restriction of light to the single horizontal rows, adjacent to the channel line, of the hosting SPPBG structure.

Investigations of the waveguiding efficiency, for the various channel widths and excitation wavelengths, have been performed experimentally by measuring vertical cross sections at the end of the structure, see figure 3.30. The width of the four lines range from 2 to 5 missing rows of nano-particles. For all wavelengths, waveguiding along the two widest

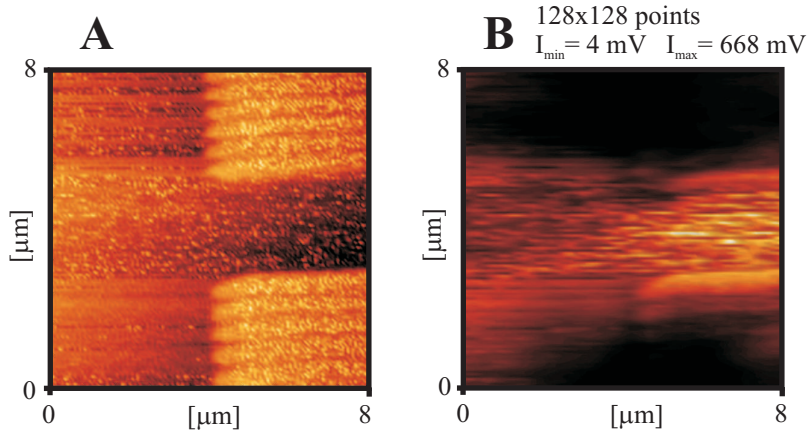


Figure 3.29: Topography (**A**) and near-field (**B**) measurements of the end of the widest channel line.

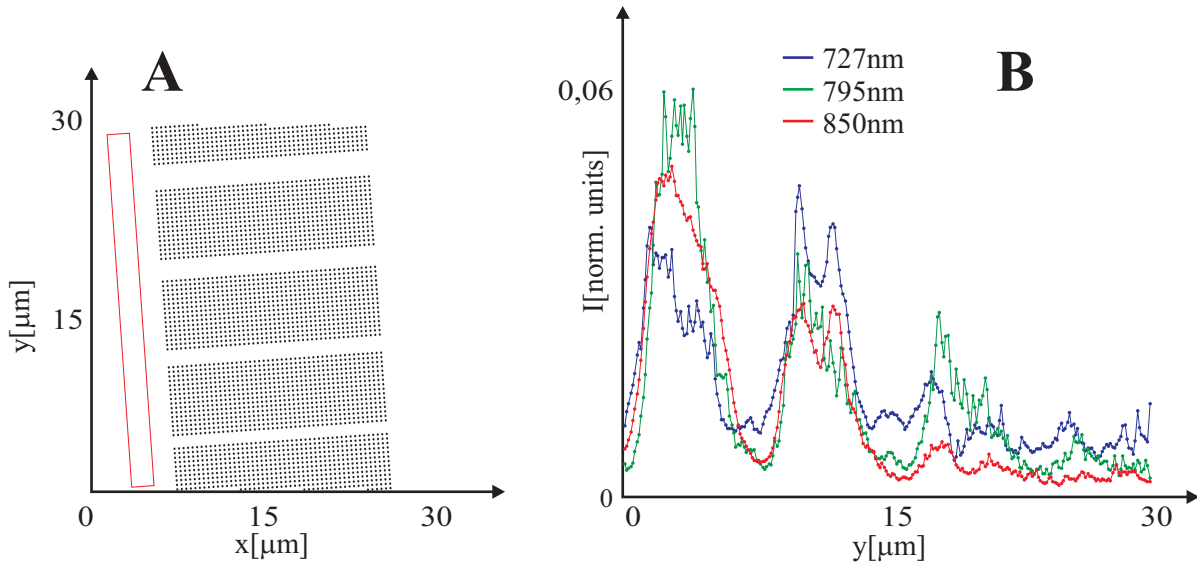


Figure 3.30: **A:** The area, marked by the red square, at the end of the structure maps the measured cross sections. The intensities along the short end of the square are averaged and displayed (**B**). The profiles have been normalized, i.e. the values are divided by the maximum intensity of the corresponding overall scan.

channels is observed as well as inhibited propagation throughout the narrowest line. It is slightly indicated that waveguiding along the line of 3 missing defect rows, only occurs for 795nm.

Concluding Remarks

Modelling of elastic scattering of SPPs has been carried out by employing the multiple scattering dipole approach treating the particles as point-like scatterers. As far as simple structures are concerned, there exists good resemblance between the measured and modelled near-field intensity distributions. However, for larger structures, with small

inter-scatter distances, it has proven difficult to obtain images which bear decent comparison with experimental investigations. The reflectivity and transmittance calculations from the triangular and quadratic structures of figures 3.18 and 3.23, respectively, indicate the presence of a band gap. Based on a consideration of energy conservation, the sum of the reflectivity and transmittance in these measurements must equal the unitary incident intensity, which is not the case. A more precise choice in the value of the polarizability may slightly improve this inconsistency. However, in general, it seems unreasonable that the physical picture may be justified only for a very limited range of α .

Much of the efforts in relation to modelling of SPPBG structures have been concentrated in finding a proper value of the polarizability for each specific situation, i.e. by calculating reflected and transmitted intensity distributions for many α -values, including complex numbers, prior to any image modelling. For this purpose, approximations introduced in the computation process have proven quite helpful, thus reducing computation times and allowing more extensive investigations. It is quite clear that the treatment of the scatterers as point-like is an approximation which may become increasingly unreasonable as the separation distances become comparable to the scatterer dimensions. Further study of the polarizability and its wavelength dependence and of higher harmonics in the SPP field scattered from an individual surface defect [7], could possibly prove helpful in the efforts of improved modelling of SPPBG structures.

From the SNOM measurements of quadratic structures it is observed that, with the range of investigation, no clear local maximum of the damping constant has been found, implying no presence of a band gap. Clearly, the supposed band gap, from the modelling section, at 790nm, is not seen. Instead, the decaying tendency of the graph could indicate a band gap towards the lower end of the investigated spectrum. Investigations with the He-Ne excitation source could extend the range of investigation. However, it should be borne in mind that the theoretical propagation length for light with this wavelength on a semi-infinite gold surface is approximately $7\mu\text{m}$. Taking into account additional radiation damping, the propagation length is lowered even further, so the feasibility of applying He-Ne light is yet questionable.

CONCLUSION

The primary purpose of this project has been to experimentally study the near-field patterns of scattered SPPs by means of SNOM. As a preliminary preparation to this, the shape of the strong SPP field, created from a tightly focused excitation source, has been studied in detail for varying wavelengths. Several phenomena associated with this, such as decreased propagation length, beam waist dispersion and oscillations along the intensity profile, have been explained and modelled showing superior resemblance with the experimental images. The subsequent discussion has led to the suggestion that a coated sharp fibre tip, thicker metal film layer and a lower angular range of incident light components can provide smoother intensity profiles, thus reducing the present side effects.

SPP scattering from simple structures of low dimensional gold nano-particles has shown to be quite weak as confirmed by SNOM measurements with a parallel excitation source. Measured images of the simple structures are dominated by strong external scattering, possibly from larger defects. By applying focused excitation light, the scattered field pattern from a line array of nano-particles has been observed and modelled showing good resemblance between theory and experiments.

For the more extensive SPPBG structures, the applied model for calculation of the SPP field intensity distribution has shown some limitations. Still, calculations of the reflectivity and transmittance have been carried out for SPP propagation in the ΓK - and ΓX -direction in SPPBG structures of triangular and quadratic lattice arrays, respectively, each with a lattice constant of 400nm. The results suggest SPP band gaps at 690nm for the triangular structure and at 790nm for the quadratic structure. Experimental SNOM measurements of SPP propagation on a gold film covered with gold particles, arranged in a quadratic SPPBG structure with similar dimensions as the one investigated by modelling, show a clear wavelength dependency of the SPP penetration into the structure in agreement with similar investigations of random surface plasmon nanostructures. However, in relation to the band gap, the measurements show poor resemblance with the results of the modelling.

Finally, SPP propagation in the same quadratic SPPBG structure along channels, in the form of lines of missing nano-particles, has been investigated experimentally by SNOM for three different wavelengths. The results indicate a strong inhibition of SPP propagation along the narrowest channels whereas for channels of 4 and 5 missing lines, SPP propagation is evident.

APPENDIX A

SURFACE PLASMON POLARITONS

This appendix provides an introduction to the phenomena associated with SPPs. Since the fields of SPPs are evanescent in nature, evanescent fields in a total internal reflection scheme is investigated in general in appendix B. This forms a basis for a description of SPPs, both from a phenomenological and a theoretical perspective. The fundamental properties, which are investigated in the subsequent section, lead to experimental parameters important in the process of creating SPPs. Throughout the writing process of this appendix [6], [19][pages 270 to 273] and [20][pages 1 to 6] are been used in general.

Plasma Oscillations

The basics of understanding the creation of a SPP involves an introduction to the phenomenon known as plasma oscillations.

Consider a metal having free electrons, meaning electrons capable of moving freely between nuclei. If, in addition, these are supposed to be completely unaffected by the nuclei, the electrons are considered to be randomly distributed and to behave as a gas. In relation to this, the corresponding nuclei lattice of positive ions is supposed to be uniformly distributed with a positive charge distribution equal to the average electronic charge distribution but of opposite sign. This positive background charge density is assumed not to fluctuate, since the movement of nuclei in a solid state matter is relatively small compared to that of the electrons. The bonded electrons are omitted in this picture, since these are strongly confined to be near the corresponding nucleus. This model therefore treats a gas composed of ionized species, or free electrons - a plasma.

The electron gas density may vary due to external excitations. If the electronic charge density is reduced locally, the positive nuclei lattice is less screened by the electronic charges. Electron screening means that the positive ion is covered by a cloud of electrons opposing the Coulomb potential, implying that the Coulomb potential of the ion is more significant the less the screening. Due to the strong tendency that charge neutrality must be obtained, the restoring force causes too many electrons to move to the positive region thus overcompensating for the local charge density reduction. The repulsive Coulomb force between the close packed compensating electrons produces motion in the opposite direction and the local electronic charge density is once more reduced. This process repeats itself as longitudinal oscillations of the plasma throughout the matter - thereby the concept of plasma oscillations. Figure A.1 contains an illustration of plasma oscillations.

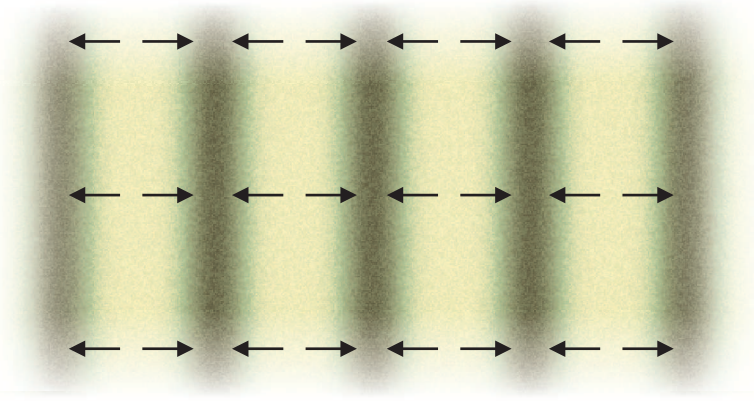


Figure A.1: *Plasma oscillations of an electron gas - the bright and dark colors are related to areas of low and high electron density, respectively. The red arrows indicate the displacement of the electrons.*

Plasmons

The energy of a plasma oscillation is quantized and the quanta are called plasmons in analogy with photons, phonons etc. The energy of plasmons in the bulk of a material is $\hbar\omega_p$, where ω_p is the plasma frequency.

An expression for this frequency can be obtained by applying the equation of motion of a unit volume of the electron gas

$$nm_e \frac{d^2u}{dt^2} = -neE = -ne \frac{neu}{\epsilon_0}, \quad (\text{A.1})$$

where n is the electron concentration and u is the displacement of the electron gas creating the electric field $E = \frac{neu}{\epsilon_0}$ which acts as a restoring force on the gas. The oscillatory movement has the time dependence $e^{-i\omega_p t}$ giving the relation $\frac{d^2u}{dt^2} = -\omega_p^2 u$. Hence, applying this with (A.1), the plasma frequency in a bulk plasma of free electrons is

$$\begin{aligned} -nm_e \omega_p^2 u &= \frac{-n^2 e^2 u}{\epsilon_0} \\ \omega_p &= \sqrt{\frac{ne^2}{m_e \epsilon_0}}. \end{aligned} \quad (\text{A.2})$$

Additionally, (A.1) is applied to calculate the displacement of the electron gas in general

$$u = \frac{eE}{m_e \omega^2},$$

where ω no longer is the plasma frequency, but an arbitrary frequency giving the time dependency of the free electrons. This is now used to calculate the polarization $P(\omega)$

$$P(\omega) = -neu = -\frac{ne^2 E(\omega)}{m_e \omega^2}.$$

The dielectric function for a gas is defined as

$$\begin{aligned}
 \epsilon(\omega) &= 1 + \frac{P(\omega)}{\epsilon_0 E(\omega)} \\
 &= 1 - \frac{ne^2}{\epsilon_0 m_e \omega^2} \\
 &= 1 - \frac{\omega_p^2}{\omega^2}
 \end{aligned} \tag{A.3}$$

In the last rewriting (A.2) is applied.

Surface Plasmon Polaritons

Surface plasmon polaritons are, as the name indicates, related to plasma oscillations confined to the surface of a material containing an electron gas. The additional word "polariton" refers to the coupling between the surface oscillation and an electromagnetic wave.

Optical excitations from s- and p-polarized waves are considered. S-polarized waves are perpendicular to the plane of incidence, that is $E(z) = E_y(z)$. In this case it is not possible to excite SPPs since s-polarized surface oscillations are non-existent due to the tangential electric field being continuous across the surface producing no surface charge [7][page 27].

In figure A.2 the field configuration of SPPs propagating in the x-direction at a metal-air interface is shown. Charge oscillations occur in the x- and z-direction. In the latter case,

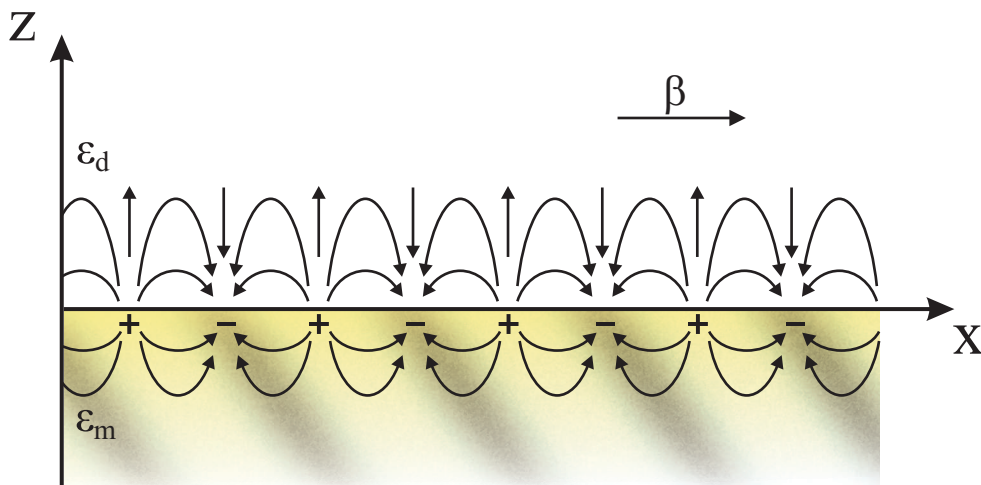


Figure A.2: *The charge fluctuations involved in SPPs propagating on a surface in the x-direction. β is the propagation constant.*

this happens within a small distance of 1\AA . The SPPs propagate along the x-direction. This implies that they consist of a combined transverse (z-direction) and longitudinal

(x-direction) electromagnetic field thereby exhibiting combined electromagnetic wave and surface charge character. This leads to the field components normal to the surface decaying exponentially into both media, see figure A.3 thus effectively confining the SPPs to the surface.

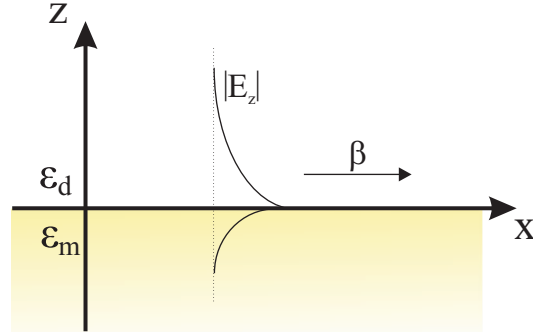


Figure A.3: SPPs propagating in the x-direction. The electric field in the z-direction is decaying exponentially.

The range of eigen frequencies of the longitudinal oscillations of the propagating SPPs is within $\omega = 0$ to $\omega = \frac{\omega_p}{\sqrt{2}}$ [20] [page 1], with a dispersion relation $\omega(k_x)$ slightly different than, and non-intersecting, that of the light. Appendix C treats the theoretical and practical considerations in matching the wave vectors of, and thereby coupling, surface plasma oscillations and photons.

Fundamental Properties

Fundamental properties of the electromagnetic fields of SPPs, such as dispersion relation and propagation, are treated theoretically in this section.

Consider the interface between two semi-infinite media of dielectric air and metal, figure A.2, with the dielectric function $\epsilon_m = \epsilon'_m + i\epsilon''_m$. The aim of the following is to obtain an expression of the wave propagating on the interface between the two media. Through Maxwell's equations the wave equation can be obtained

$$\nabla^2 \mathbf{E} - \frac{\epsilon}{c^2} \frac{\partial^2 \mathbf{E}}{\partial t^2} = 0. \quad (\text{A.4})$$

A solution to this equation is known to be a plane wave on the form $\mathbf{E} = E e^{-i\omega t}$. Applying this solution to (A.4) gives the Helmholtz equation

$$\begin{aligned} \nabla^2 \mathbf{E} + \frac{\omega^2}{c^2} \epsilon \mathbf{E} &= 0 \Rightarrow \\ \frac{\partial^2 \mathbf{E}}{\partial x^2} + \frac{\partial^2 \mathbf{E}}{\partial z^2} + \frac{\omega^2}{c^2} \epsilon \mathbf{E} &= 0. \end{aligned} \quad (\text{A.5})$$

The y-component of the ∇ -operator vanishes because all the considered waves are in the xz-plane. The Helmholtz expression for a field is $\psi(x, z) = \psi(z) e^{i\beta x}$, where β is the

propagation constant. Substitution of this into (A.5) yields

$$-\beta^2\psi(z)e^{i\beta x} + \frac{\partial^2}{\partial z^2}\psi(z)e^{i\beta x} + \varepsilon k_0^2\psi(z)e^{i\beta x} = 0 \Rightarrow \quad (\text{A.6})$$

$$\frac{\partial^2}{\partial z^2}\psi(z) + (\varepsilon k_0^2 - \beta^2)\psi(z) = 0. \quad (\text{A.7})$$

The associated electric field vector of the p-polarized waves are in the xz-plane, implying that the magnetic field is oriented in the y-direction. The attention is turned to this field $H(z) = H_y(z)$ in the analysis. The two boundary conditions for the waves are continuity for $H(z)$ and $\frac{\partial H(z)}{\partial z}$ at the interface $z = 0$. To verify the condition for $\frac{\partial H(z)}{\partial z}$ one of Maxwell's equations is used

$$\begin{aligned} \nabla \times \mathbf{H} &= i\omega\varepsilon\mathbf{E} \Rightarrow \\ E_x(z) &= \frac{i}{\omega\varepsilon} \frac{dH_y(z)}{dz} \quad \text{and} \end{aligned} \quad (\text{A.8})$$

$$E_z(z) = \frac{-i}{\omega\varepsilon} \frac{dH_y(z)}{dx}. \quad (\text{A.9})$$

Since the slope of the x-component of the electric field changes abruptly at $z = 0$, as can be seen in figure A.3, this condition can only be fulfilled if $\varepsilon_m < 0$ and $\varepsilon_d > 0$.

The boundary conditions for $H(z)$ are now verified. If the two media are assumed to have two different relative dielectric constants ε_m and ε_d , (A.7) provides two equations to solve, one for each medium

$$\begin{aligned} \frac{\partial^2 H_m(z)}{\partial z^2} + (\varepsilon_m k_0^2 - \beta^2)H_m(z) &= 0 \quad \text{and} \\ \frac{\partial^2 H_d(z)}{\partial z^2} + (\varepsilon_d k_0^2 - \beta^2)H_d(z) &= 0. \end{aligned}$$

With the exponential decay of the SPPs into each of the media two solutions to these equations are

$$H_m(z) = Ae^{\sqrt{\beta^2 - \varepsilon_m k_0^2} z} \quad \text{and} \quad (\text{A.10})$$

$$H_d(z) = Be^{-\sqrt{\beta^2 - \varepsilon_d k_0^2} z}. \quad (\text{A.11})$$

These magnetic fields are continuous at $z = 0$ provided that $A = B$. (A.8) and (A.9) give the boundary conditions for $\frac{\partial H(z)}{\partial z}$. Differentiation with (A.10) and (A.11) inserted yields

$$\begin{aligned} -\frac{1}{\varepsilon_d} \sqrt{\beta^2 - \varepsilon_d k_0^2} &= \frac{1}{\varepsilon_m} \sqrt{\beta^2 - \varepsilon_m k_0^2} \Rightarrow \\ \beta^2(\varepsilon_d^2 - \varepsilon_m^2) &= k_0^2(\varepsilon_m \varepsilon_d^2 - \varepsilon_d \varepsilon_m^2) \Rightarrow \\ \beta^2 &= k_0^2 \frac{\varepsilon_m \varepsilon_d (\varepsilon_d - \varepsilon_m)}{(\varepsilon_d - \varepsilon_m)(\varepsilon_d + \varepsilon_m)} \Rightarrow \\ \beta &= k_0 \sqrt{\frac{\varepsilon_d \varepsilon_m}{\varepsilon_d + \varepsilon_m}}. \end{aligned} \quad (\text{A.12})$$

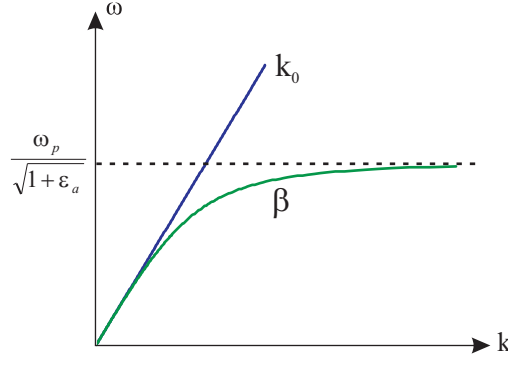


Figure A.4: Dispersion relations for the light in vacuum (blue line) and for SPPs (green line). The maximum frequency allowed for SPPs, shown by the dashed line, is given by $\frac{\omega_p}{\sqrt{1+\varepsilon_d}}$. The two lines are non-intersecting.

This is the dispersion relation for SPPs, and β is the propagation constant. Hereby the necessary boundary conditions are fulfilled, and it is shown that TM-waves, $\varepsilon_m < 0$ and $\varepsilon_d > 0$, are necessary to generate SPPs. Additionally, since β is a propagation constant, (A.12) must be positive. Since ε_m and ε_d are of opposite sign the nominator is negative, and thus the denominator must be negative. Substitution of (A.3) into (A.12) yields

$$\beta = k_0 \sqrt{\frac{\left(1 - \frac{\omega_p^2}{\omega^2}\right) \varepsilon_d}{1 - \frac{\omega_p^2}{\omega^2} + \varepsilon_d}}. \quad (\text{A.13})$$

As mentioned previously the denominator must be negative

$$1 - \frac{\omega_p^2}{\omega^2} + \varepsilon_d < 0 \quad \Rightarrow$$

$$\omega < \frac{\omega_p}{\sqrt{1 + \varepsilon_d}}. \quad (\text{A.14})$$

This expression is depicted in figure A.4, showing the maximum frequency for generating SPPs.

The magnetic field is directed along the y-axis when operating with TM-waves. This field is evanescent and expressed as

$$H(x, z) = H_y e^{i\beta x} e^{\pm \sqrt{\beta^2 - \varepsilon_m k_0^2} z}. \quad (\text{A.15})$$

Since $\beta = k_0 \sqrt{\frac{\varepsilon_m \varepsilon_d}{\varepsilon_m + \varepsilon_d}}$ and $\varepsilon_m = \varepsilon'_m + i\varepsilon''_m$, β will be of the complex form $\beta = \beta' + i\beta''$. Calculation of β' gives

$$\beta' = k_0 \sqrt{\frac{\varepsilon'_m \varepsilon_d}{\varepsilon'_m + \varepsilon_d}} = \frac{2\pi}{\lambda_0} \sqrt{\frac{\varepsilon'_m \varepsilon_d}{\varepsilon'_m + \varepsilon_d}}. \quad (\text{A.16})$$

Expressing β' as a wave vector

$$\beta' = \frac{2\pi}{\lambda_{SP}},$$

where λ_{SPP} is the wavelength of the SPPs, makes it possible to evaluate the SPP wavelength. Combining this expression with (A.16) gives

$$\begin{aligned}\frac{2\pi}{\lambda_{SPP}} &= \frac{2\pi}{\lambda_0} \sqrt{\frac{\varepsilon'_m \varepsilon_d}{\varepsilon'_m + \varepsilon_d}} \Rightarrow \\ \lambda_{SPP} &= \lambda_0 \sqrt{\frac{\varepsilon'_m + \varepsilon_d}{\varepsilon'_m \varepsilon_d}}.\end{aligned}\quad (\text{A.17})$$

The intensity of the magnetic field is the square of the absolute value given by (A.15)

$$|H(x, z)|^2 = H_y^2 e^{-2\beta'' x} e^{2\sqrt{\beta'^2 - \varepsilon'_m k_0^2} z}.\quad (\text{A.18})$$

It is the real part of this expression that describes the intensity. The wave is propagating in the x-direction, and from (A.18) the damping in this direction is $e^{-2\beta''}$. The propagation length L_{SPP} is defined as the distance along the propagation direction, at which the intensity of the SPP is $\frac{1}{e}$ of its initial value. Therefore

$$\begin{aligned}-2\beta'' L_{SPP} &= -1 \Rightarrow \\ L_{SPP} &= \frac{1}{2\beta''}.\end{aligned}\quad (\text{A.19})$$

Where β'' is calculated as

$$\beta'' = \frac{\omega}{c} \left(\frac{\varepsilon'_m \varepsilon_d}{\varepsilon'_m + \varepsilon_d} \right)^{3/2} \frac{\varepsilon''_m}{2(\varepsilon'_m)^2}.\quad (\text{A.20})$$

Similarly the penetration depth is defined as the distance from the surface where the amplitude of the magnetic field has decreased to $\frac{1}{e}$ of its initial value. For metals it is often the case that $|\varepsilon'_m| \gg \varepsilon''_m$. By taking this into consideration when calculating β' and β'' from (A.16) and (A.20) it is possible to state that $\beta' \gg \beta''$. Therefore, only the real parts of β and ε are taken into account when calculating the penetration depth, from (A.10), giving

$$\begin{aligned}-\sqrt{\beta'^2 - \varepsilon'_m k_0^2} d_m &= -1 \Rightarrow \\ d_m &= \frac{1}{\sqrt{\beta'^2 - \varepsilon'_m k_0^2}},\end{aligned}$$

where the negative sign on the left hand side corresponds to all values for z being negative in the metal. Replacing β' with the expression in (A.16) gives

$$\begin{aligned}d_m &= \frac{1}{\sqrt{k_0^2 \frac{\varepsilon'_m \varepsilon_d}{\varepsilon'_m + \varepsilon_d} - \varepsilon'_m k_0^2}} = \frac{1}{k_0 \sqrt{\frac{\varepsilon'_m \varepsilon_d - \varepsilon'_m{}^2 - \varepsilon_d \varepsilon'_m}{\varepsilon'_m + \varepsilon_d}}} \Rightarrow \\ d_m &= \frac{1}{k_0 \sqrt{\frac{-\varepsilon'_m{}^2}{\varepsilon'_m + \varepsilon_d}}} = \frac{\lambda}{2\pi} \sqrt{\frac{\varepsilon'_m + \varepsilon_d}{-\varepsilon'_m{}^2}}.\end{aligned}$$

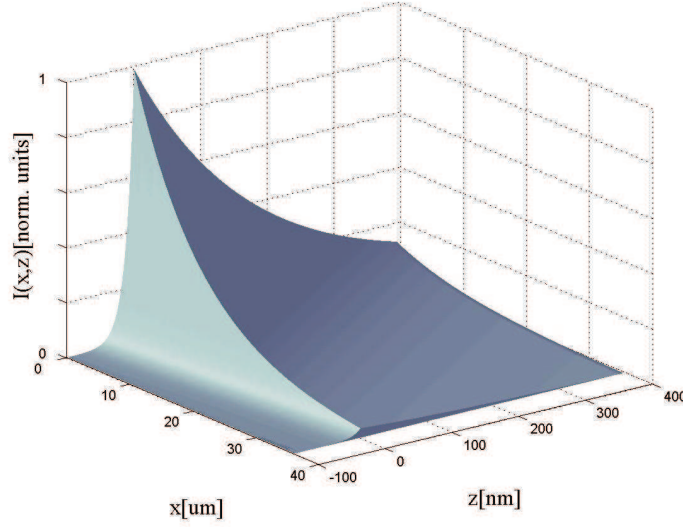


Figure A.5: *Simulation of the intensity distribution of the field from SPPs excited at origo in the (x,z,I) -coordinate system at a silver-air interface with a source wavelength of 633nm. The propagation length in this situation is $L_{SPP} = 21,3\mu\text{m}$.*

Similar calculations can be made for the dielectric medium giving the result

$$d_d = \frac{\lambda}{2\pi} \sqrt{\frac{\epsilon'_m + \epsilon_d}{-\epsilon_d'^2}}. \quad (\text{A.21})$$

The relations mentioned on this and the previous pages are used to determine the values of some fundamental parameters of SPPs, which are important in the understanding of SPP behavior of interfaces of different materials. Additionally, a simulation of the SPP field intensity distribution is carried out as shown in figure A.5. The simulation is based on the intensity of the electric field, expressed as

$$E(x,y) = E_0 e^{i\beta x} e^{-y/d} \quad \text{where} \\ d = d_d \text{ for } y \geq 0 \quad \text{and} \quad d = -d_m \text{ for } y < 0.$$

APPENDIX B

EVANESCENT FIELDS

As it will be explained more carefully throughout this appendix, SPPs are confined to an interface and the belonging electric fields are decaying exponentially into each media. Due to this exponentially decaying nature, the fields are called evanescent, so this section consists of a short description of evanescent fields in general.

The treatment of evanescent fields takes basis in the common situation of a plane wave incident on a flat interface between two homogeneous media, see figure B.1, where the

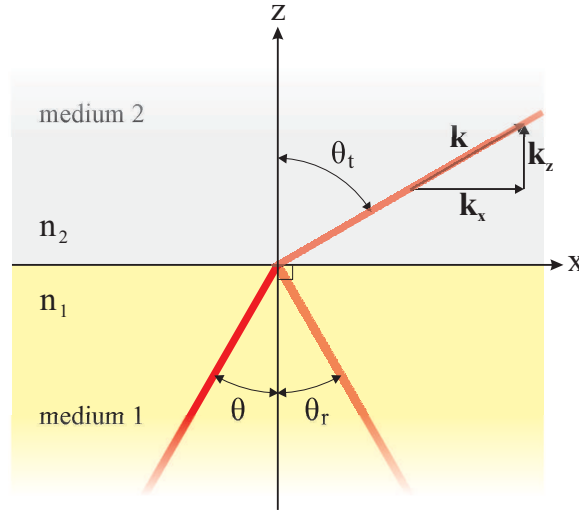


Figure B.1: A plane wave impinging on a flat surface. Since the plane of incidence is the x - z plane, the wave vector \mathbf{k} is described only by a x - and a z -component. The refractive indices are related as $n_1 > n_2$.

refractive indices and the angles are described through the common relationships of

$$\begin{aligned} \theta &= \theta_r \quad \text{and} \\ n_1 \sin \theta &= n_2 \sin \theta_t. \end{aligned} \quad (\text{B.1})$$

If the incident angle is increased considerably, θ_t approaches 90° and the incident angle equals the critical angle given by $\theta(\theta_t = 90^\circ) = \theta_c = \sin^{-1} \frac{n_2}{n_1}$ as seen from (B.1). When the incident angle is beyond the critical angle the interpretation of θ_t as an angle is invalid since

$$\sin(\theta_t) = \frac{n_1}{n_2} \sin(\theta) > 1. \quad (\text{B.2})$$

In this cases there is no propagation of light, or transport of energy, into medium 2 and total internal reflection occurs. Nevertheless, optical fields in medium 2 are present but diminishing evanescently at short distances from the interface along the z -direction. An illustration of this situation is given in figure B.2.

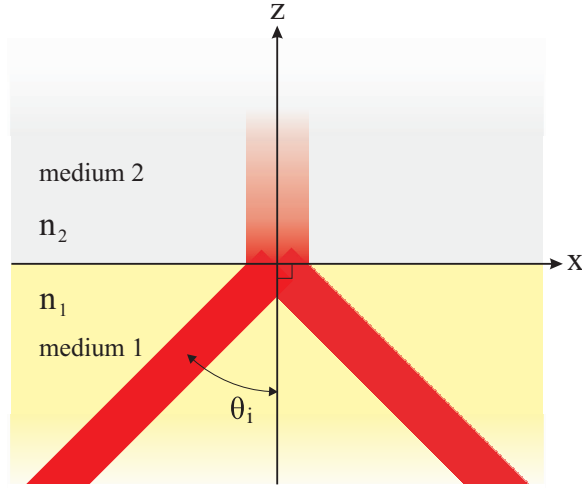


Figure B.2: Total internal reflection from an interface caused by an incident angle equal to or larger than the critical angle. The evanescent field is decaying exponentially into medium 2.

Evanescent Field Strength

The first step in the process of deducing an expression of the evanescent field strength is to find a solution to the wave equation. By applying one of Maxwell's equations this is derived in the two dimensions of the plane of incidence

$$\left(\frac{\partial^2}{\partial x^2} + \frac{\partial^2}{\partial z^2} \right) E - \frac{n^2}{c^2} \frac{\partial^2 E}{\partial t^2} = 0.$$

Substitution of the expression of a monochromatic wave, with the time dependence $e^{i\omega t}$, into this equation yields

$$\left(\frac{\partial^2}{\partial x^2} + \frac{\partial^2}{\partial z^2} \right) E + \left(\frac{\omega n}{c} \right)^2 E = 0. \quad (\text{B.3})$$

A solution to this wave equation is known to be plane wave on the form $E = Ae^{i\mathbf{k}\cdot\mathbf{r}}$. With such a plane wave defined in the coordinate system shown in figure B.1, it is clear that $k_y = 0$. The solution to the field in medium 2 then becomes

$$E(x, z) = Ae^{i(k_x x + k_z z)}. \quad (\text{B.4})$$

By inserting this into (B.3) the dispersion relation is obtained

$$k_x^2 + k_z^2 = \left(\frac{\omega n_2}{c} \right)^2 = k^2. \quad (\text{B.5})$$

Evidently, the following expressions of the x- and z-components of \mathbf{k} are possible by use of Snell's law and the dispersion relation

$$\begin{aligned} k_x &= k \sin \theta_t = \frac{\omega}{c} n_2 \sin \theta_t = \frac{2\pi}{\lambda_0} n_1 \sin \theta \quad \text{and} \\ k_z &= k \cos \theta_t. \end{aligned} \quad (\text{B.6})$$

(B.4) is now rewritten using (B.5)

$$E(x, z) = Ae^{i(k_x x + \sqrt{k^2 - k_x^2} z)}. \quad (\text{B.7})$$

The following two cases are considered:

- Refraction: the situation sketched in figure B.1 where the beam is split into a refracted and a transmitted part.
- Total internal reflection: The situation of figure B.2 showing no transmission.

In the case of refraction, $\sin \theta_t < 1$ and therefore, according to the first two terms in (B.6), $|k_x| < k$. This leads to the optical field strength in medium 2 being expressed as

$$E(x, z) = Ae^{ik_x x} e^{i\sqrt{k^2 - k_x^2} z} = Ae^{i \sin(\theta) x} e^{i \cos(\theta) z}.$$

This field consists of two waves in the x- and z-direction. Their exponents are purely imaginary and therefore they are both oscillating propagating waves and the damping, which characterizes evanescent waves, is not present. Hence, this expression represents an ordinary propagating monochromatic wave.

In the case of total internal reflection, the notion of θ_t as an angle becomes invalid, since, according to Snell's law, $\sin \theta_t > 1$ as shown in (B.2). According to the first two terms in (B.6), $|k_x| \geq k$. This gives two solutions for k_z in (B.7), that is $k_z = \pm i\sqrt{k_x^2 - k^2}$. With these the optical field of medium 2 now becomes

$$E(x, z) = Ae^{ik_x x} e^{\mp \sqrt{k_x^2 - k^2} z}.$$

The physical reasonable solution to k_z has a negative sign for $z \geq 0$, since the z-component otherwise would reach infinity at a growing distance z . In the case of total internal reflection, evanescent waves in the z-direction are achieved.

In order to illustrate the evanescent field distribution, a simulation of the intensity of this field, $I = |E(x, z)|^2$, has been carried out, see figure B.3. As indicated by the figure, evanescent fields are strongly confined to the interface, since these seem to appear mostly within a sub wavelength distance from the interface.

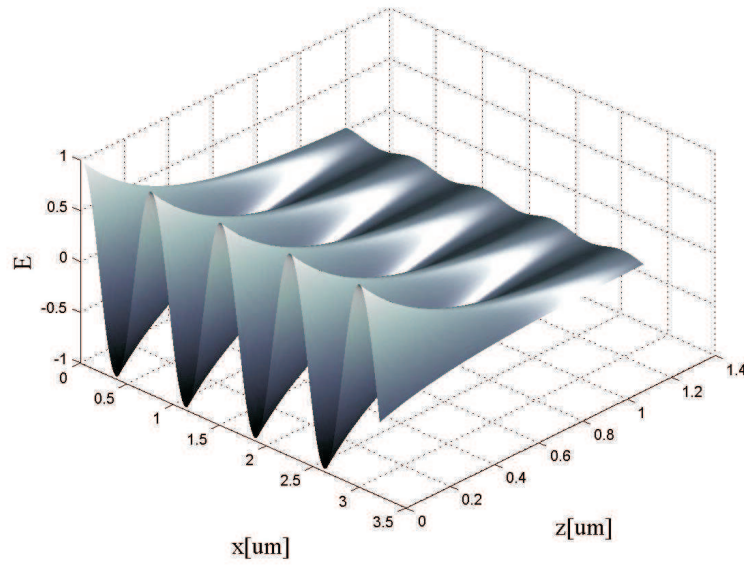


Figure B.3: *Simulation of the evanescent field intensity near an interface. The value k_x has been calculated according to (B.6) and the remaining parameter values are $n_p = 1.5$, $\theta_i = 45^\circ$ and $\lambda_0 = 632,8\text{nm}$.*

APPENDIX C

EXCITATION OF SURFACE PLASMON POLARITONS

In order to monitor excitation of SPPs a phenomenon known as attenuated total reflection (ATR) is applied. As indicated by the name, light impinging an interface is totally reflected but yet attenuated, since some of the photons are converted into SPPs. A setup for generating SPPs using ATR is the Kretschmann configuration shown in figure C.1. In figure A.4 on page 64 it has been demonstrated that the dispersion curves for the light line in vacuum and the SPPs are non-intersecting, indicating that it is not, at first, possible to match the wavevectors of light and surface plasmons. The main idea with the Kretschmann configuration is to enhance the wave vector of the applied light, via the dispersion of the prism, in order to couple with the surface plasmons.

In figure C.2 the dispersion line of vacuum and a prism is compared with the dispersion line of surface plasmons in silver. The dispersion line of the x-component of the prism wave vector matches that of the SPP wave vector at the frequency ω_1 , as both vectors are similar both in magnitude and direction. Hence, in this particular case it is possible to excite SPPs. Simply this means that the incident angle, the frequency of applied light and the refractive index of the prism are adjusting parameters decisive for the possibility of generating SPPs. The correlation between these parameters are investigated in the subsequent text.

The SPPs propagate along the interface between the metal and air. This means that $\varepsilon_d = 1$ in the following. For the dispersion relation (A.12) this gives

$$\beta = k_0 \sqrt{\frac{\varepsilon_m \varepsilon_d}{\varepsilon_m + \varepsilon_d}} = k_0 \sqrt{\frac{\varepsilon}{\varepsilon + 1}}, \quad (\text{C.1})$$

where the dielectric constant for the metal has been simplified to $\varepsilon_m = \varepsilon$. Since the green dispersion curve representing β in figure A.4 is to the right and non-intersecting the blue dispersion line of k_0 a requirement for generation of SPPs is

$$\beta = \sqrt{\frac{\varepsilon}{\varepsilon + 1}} k_0 > k_0 \Rightarrow \varepsilon < -1.$$

This requirement for the value of ε is the case for most metals, but not for glass. This is the reason for the requirement of the thin layer of metal. From figure C.1 the x-component of incident field on the metal layer inside the prism is

$$k_{xp} = k_0 n_p \sin(\theta)$$

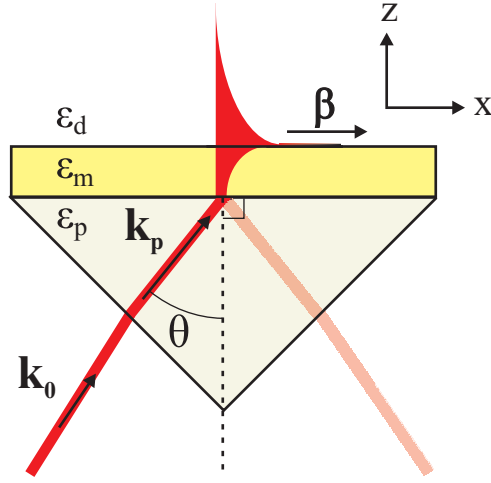


Figure C.1: *The Kretschmann configuration. By using an additional prism metal interface, it is possible to couple photons with the surface plasma oscillations allowing excitation of SPPs.*

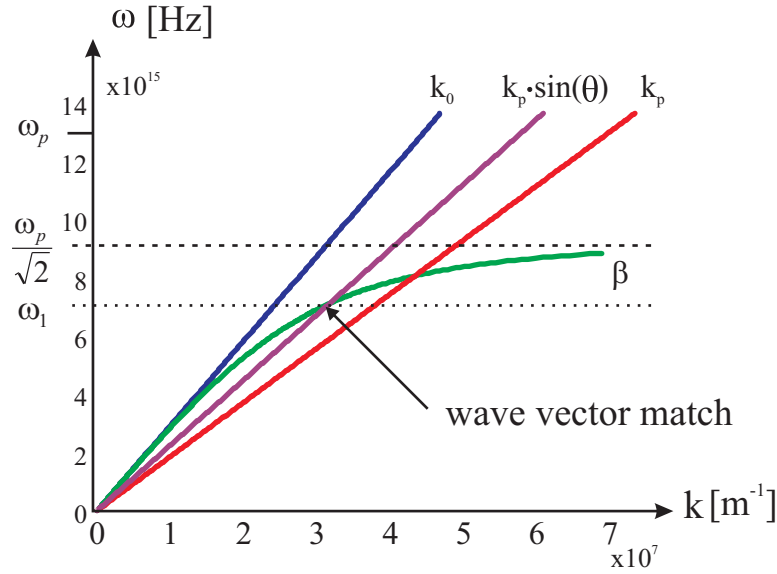


Figure C.2: *The dispersion relation of vacuum (blue line) and a glass prism with $\sqrt{\epsilon_p} = 1.5$ (red line). The corresponding x -components of the vacuum and prism wave vectors are shown as the purple and turquoise lines respectively. The SPP dispersion line has been generated for silver by applying the SPP wave vector expression in (A.13). The plasma frequency is calculated using (A.2) on page 60 with a conduction electron density of $5,85 \cdot 10^{28} \text{m}^{-3}$.*

Where n_p is the refractive index for the prism and k_0 is the wave vector in vacuum. If $k_{xp} < k_0$ it gives

$$\begin{aligned} k_0 n_p \sin(\theta) &< k_0 \Rightarrow \\ n_p \sin(\theta) &< 1. \\ \text{Snell's Law: } n_p \sin(\theta) &= n_{air} \sin(\theta') = \sin(\theta') \end{aligned}$$

This means that Snell's law is valid and the light is transmitted. For $k_x > k_0$ it is similar to show that Snell's law is invalid and TIR is obtained. But for the angle of SPP excitation, at $k_{xp} = \beta$, the reflected light is attenuated corresponding to excitation of SPPs. From (C.1) the following is obtained

$$\begin{aligned} k_0 n_p \sin(\theta) &= k_0 \sqrt{\frac{\varepsilon}{\varepsilon + 1}} \Rightarrow \\ n_p \sin(\theta) &= \sqrt{\frac{\varepsilon}{\varepsilon + 1}}. \end{aligned} \quad (\text{C.2})$$

One way of finding this angle in practice is to measure the reflectivity as a function of the incident angle. An expression for the reflectivity is derived in appendix E by treating the Kretschmann configuration as a three layer system with multiple reflections within the metal film. The expression is

$$R(\theta) = \left| \frac{r_{pm} + r_{mair} e^{2ik_{zm}d}}{1 + r_{pm} r_{mair} e^{2ik_{zm}d}} \right|^2, \quad (\text{C.3})$$

where r_{pm} and r_{mair} are reflection coefficients at the prism-metal and metal-air interface respectively. These are given by [20][page 120]

$$\begin{aligned} r_{pm} &= \frac{\frac{k_{zp}}{\varepsilon_p} - \frac{k_{zm}}{\varepsilon_m}}{\frac{k_{zp}}{\varepsilon_p} + \frac{k_{zm}}{\varepsilon_m}} \quad \text{and} \\ r_{mair} &= \frac{\frac{k_{zm}}{\varepsilon_m} - \frac{k_{zair}}{\varepsilon_{air}}}{\frac{k_{zm}}{\varepsilon_m} + \frac{k_{zair}}{\varepsilon_{air}}}, \end{aligned} \quad (\text{C.4})$$

where the z-component of the wave vector of the proper medium is expressed as

$$k_{z(p,m,air)} = \frac{2\pi}{\lambda_0} \sqrt{\varepsilon_{(p,m,air)} - \varepsilon_0 \sin^2(\theta)}. \quad (\text{C.5})$$

Hence, the angle of minimum reflection in (C.3) will correspond to maximum ATR.

APPENDIX D

PHYSICS OF ATTENUATED TOTAL REFLECTION

Physical explanations to ATR in the Kretschmann configuration are provided in this appendix viewed from two different perspectives; by means of ray tracing and by means of enhancement of the SPP wave vector due to the near presence of the prism medium. These ideas are developed further below.

Ray Tracing Picture

Consider a light ray impinging the prism-metal layer at the incident angle for SPP excitation - it is partly reflected and partly transmitted. The transmitted part traverses the metal layer approaching the metal-air interface and is decaying exponentially along the way due to internal damping in the silver. Subsequently, the remaining light induces SPP excitations at the metal-air interface. At this instant, the reflected light at the prism-metal interface continues and leaves the Kretschmann configuration.

The near presence of the prism medium causes some of the SPPs to radiate light back into the prism, backscattered light. This radiation is in antiphase with the reflected light at the prism-metal interface. The backscattered light then interferes destructively with the reflected light, but the backscattered amplitude A_{back} is initially quite low compared to the reflected amplitude A_r and ATR is unnoticeable. However, as the SPPs propagate along the surface the SPP amplitude is being built up to a stable level due to a continuous supply of excitation light giving an increased A_{back} and thereby increased ATR. As the thickness of the metal layer is decreased, the internal damping of the transmitted part traversing the metal layer is decreased and naturally the degree of excitation of SPPs is increased. This contributes to an increase in A_{back} and at a certain thickness the backscattered and the reflected light even compensate each other. This is the situation of total ATR and thereby maximum SPP excitation efficiency. In principle, since no energy is leaving the system, everything is eventually transferred into heat in the metal film at total ATR. A further decrease in the thickness leads to a larger A_{back} which is then not fully compensated by the smaller A_r giving a non-zero reflectivity from the sample.

SPP Wave Vector Enhancement

The SPP wave vector in the interface between two semi-infinite media has been derived previously in this chapter, (A.13) on page 64. This is not the case with the Kretschmann configuration, which deals with a metal layer of finite thickness. In this explanation total internal reflection is assumed at the prism-metal interface. The generated evanescent

wave in this interface excites SPPs at the metal-air layer as long as the thickness of the metal film is relatively small. At a small thickness the evanescent light wave is capable of influencing the SPP wave vector adding an additional term to it

$$\beta_{Kretschmann} = \beta + \Delta\beta.$$

The real part of $\Delta\beta$ causes a displacement of the resonance position compared to β . As demonstrated previously in this chapter, in the case of an interface between two semi-infinite media, the damping of the SPP is given by β'' , whereas in the present situation the total damping amounts to

$$\Gamma_{total} = \beta'' + \Delta\beta'' = \Gamma_i + \Gamma_{back},$$

showing that an additional backscattered damping is present in the Kretschmann configuration. Calculations performed in [20][Appendix II] yield a reflectivity relation expressed in terms of the internal and backscattered damping

$$R = 1 - \frac{4\Gamma_i\Gamma_{back}}{(k_{xp} - (\beta + \Delta\beta))^2 + (\Gamma_i + \Gamma_{back})^2}. \quad (D.1)$$

The value of Γ_{back} needed to provide minimum reflectivity of R in the resonance case, where $k_{xp} = \beta + \Delta\beta$, can be found by means of differentiation of (D.1)

$$\begin{aligned} \frac{dR}{d\Gamma_{back}} &= \frac{4\Gamma_i(\Gamma_i + \Gamma_{back})^2 - (2\Gamma_i + 2\Gamma_{back})4\Gamma_i\Gamma_{back}}{(\Gamma_i + \Gamma_{back})^4} = 0 \Rightarrow \\ \Gamma_{back} &= \Gamma_i. \end{aligned} \quad (D.2)$$

The thickness of the metal layer may be adjusted thereby changing the value of Γ_{back} implying that a certain thickness gives total ATR thus fulfilling the condition in (D.2). In relation to this it should be mentioned that the propagation length of SPPs in this resonance case is halved by comparison with the relation in (A.19) on page 65

$$\begin{aligned} \text{semi-infinite media : } L_{SPP} &= \frac{1}{2\beta''} = \frac{1}{2\Gamma_i} \quad \text{and} \\ \text{Total ATR : } L_{SPP,ATR} &= \frac{1}{2(\Gamma_i + \Gamma_{back})} = \frac{1}{2}L_{SPP}. \end{aligned} \quad (D.3)$$

In addition to the physical explanation, the effects of changing parameters of the expression in (C.3) are henceforward studied in detail, explained and demonstrated through simulations.

Thickness

The effect of a changing thickness parameter is illustrated in figure D.1 using five different values of the metal layer thickness. This seems to be a powerful parameter strongly responsible for the degree of maximum ATR and the shape of the graph. As mentioned in the previous section total ATR is only possible at a certain thickness d_{min} which, in

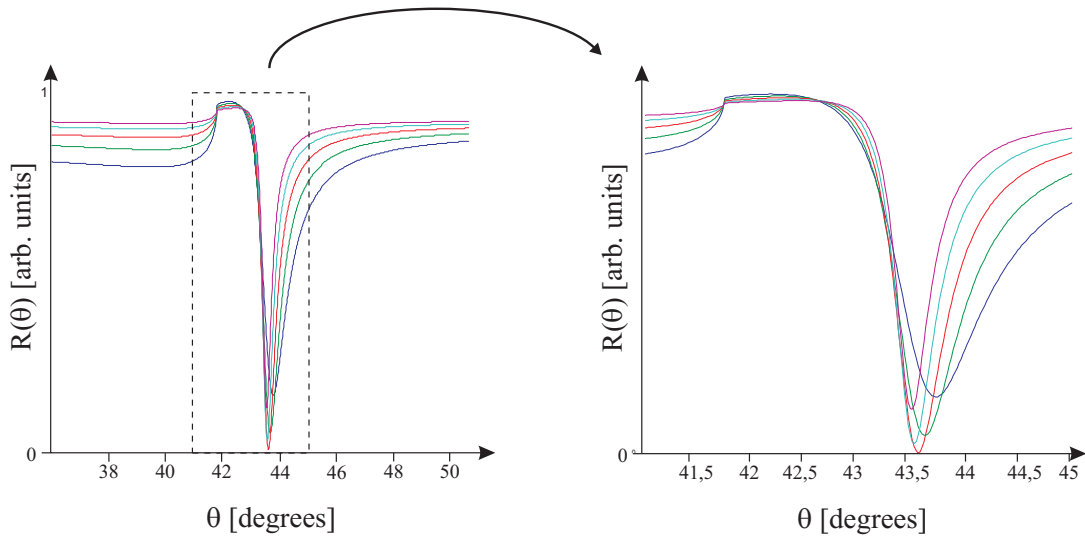


Figure D.1: Simulation of reflectivity using different thicknesses of the silver layer. The applied parameters are $\varepsilon_{Ag} = -16 + 1.1i$, $n_p = 1,5$ and $\lambda_0 = 632,8nm$. The applied thickness value is increasing from $d_{Ag} = 35nm$ (blue line) in intervals of 5nm up to $d_{Ag} = 55nm$ (purple line).

addition, is shown by this simulation. The half-width of the reflection minimum curve is increased by decreasing thickness. The reason is obvious when considering the fraction of (D.1). As the thickness becomes small, Γ_{back} increases. This makes the term $(\Gamma_i + \Gamma_{back})^2$ increasingly dominant compared to $(k_{xp} - (\beta + \Delta\beta))^2$. The latter term is a function of θ , so a relatively broad range of θ angles, around the reflection minimum, gives low reflectivity and thereby a large half-width. In the opposite case, when the thickness is large, the denominator term $(\Gamma_i + \Gamma_{back})^2 \rightarrow \Gamma_i^2$ and the fraction becomes increasingly sensitive to changes in the term $(k_{xp} - (\beta + \Delta\beta))^2$. Consequently the half-width of the reflection minimum in this case becomes small.

It is observed that the minimum of the reflection curves is displaced to the right with decreasing thickness. The reason to this is found in the real part of $\Delta\beta$. As the thickness is decreased, the SPP comes closer to the evanescent wave at the prism-metal interface and its wave vector is therefore increasingly influenced. At small thicknesses $\Delta\beta'$ is increased and the k_{xp} wave vector has to be enhanced to obtain resonance. This is done by increasing the incident angle, thus displacing the reflection minimum to the right along the angle axis.

In order to further evaluate the certain values of d_{min} , the minimum reflection of two samples, with a silver layer and a gold layer respectively, is calculated at various thicknesses in the interval from 1nm to 100nm, see figure D.2. For the sample of silver layer ATR occurs at 45nm whereas for the gold sample this happens at 53nm. This information is of great importance if one wants to construct an ATR coupler with reflection minimum near zero.

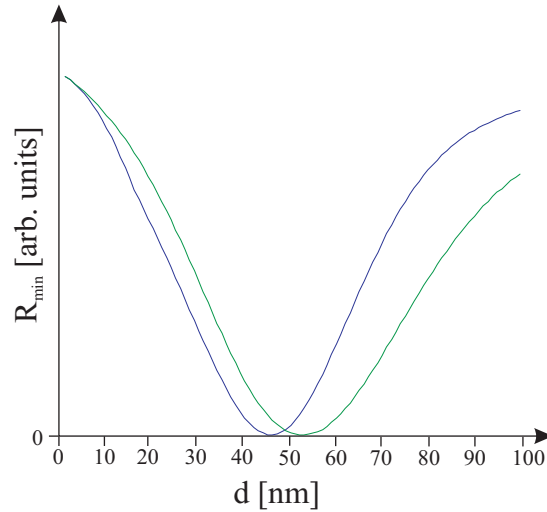


Figure D.2: Calculated reflection minima from a sample with a silver layer (blue) and a gold layer (green) at various thicknesses. The thickness parameter is increased in steps of 1nm.

Refractive Index of the Prism

Suppose one takes account of an offset error in the angular measurement, this merely shifts the reflectivity graph to one of the sides not affecting the tendency of the graph. Similarly, this is the case for a change, within a reasonable range, of the refractive index of the prism, which is illustrated in figure D.3. The reason to this is rather obvious. As mentioned on page 71 the dispersion of the prism is used to enhance the wave vector of the applied light, in order to couple with SPPs. Therefore, the larger the refractive index of the prism the larger the wave vector k_p and hence a smaller incident angle at the prism-metal interface is needed to enhance the value of the x-component of k_p to the value of the SPP wave vector.

Dielectric Constant of the Metal

The effect of changes in the real and imaginary part of the dielectric constant of the metal are illustrated in figure D.4. An increase in the real part of ϵ_m seems to broaden the peak and shift the incident angle of maximum ATR. This peak is similarly broadened when increasing the imaginary part, but in addition, the amount of maximum obtainable ATR seems strongly dependent on this parameter. The explanation to the shift in the reflection minima is found by considering the SPP dispersion relation, (A.16) on page 64

$$\beta' = k_0 \sqrt{\frac{\epsilon'_m}{\epsilon'_m + 1}}.$$

An increase in ϵ'_m causes an increase in β' . For instance, the SPP dispersion at the blue line, $\beta' = k_0 \sqrt{\frac{-14}{-13}}$ is larger than the dispersion at the purple line, $\beta' = k_0 \sqrt{\frac{-18}{-17}}$. In the case of $\Delta\beta'$ this value is similarly increased with increasing ϵ'_m . This is verified by

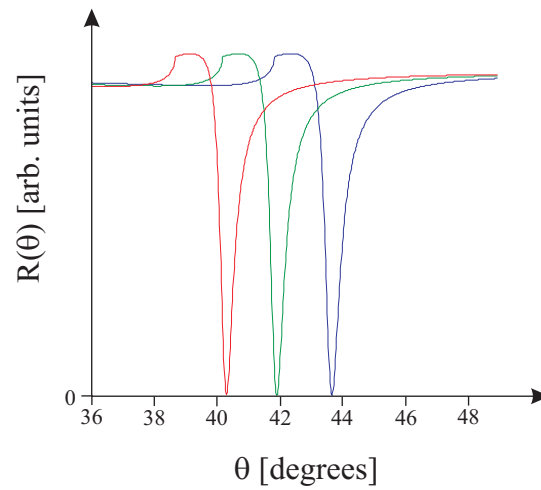


Figure D.3: Reflection curves in the case of 3 different values of the refractive index. These are 1,5 (blue), 1,55 (green) and 1,6 (red). The laser wavelength and the thickness and dielectric constant of the silver layer are $\lambda_0 = 632,8\text{nm}$, $d=45\text{nm}$ and $\epsilon_m = -16 + 1.1i$.

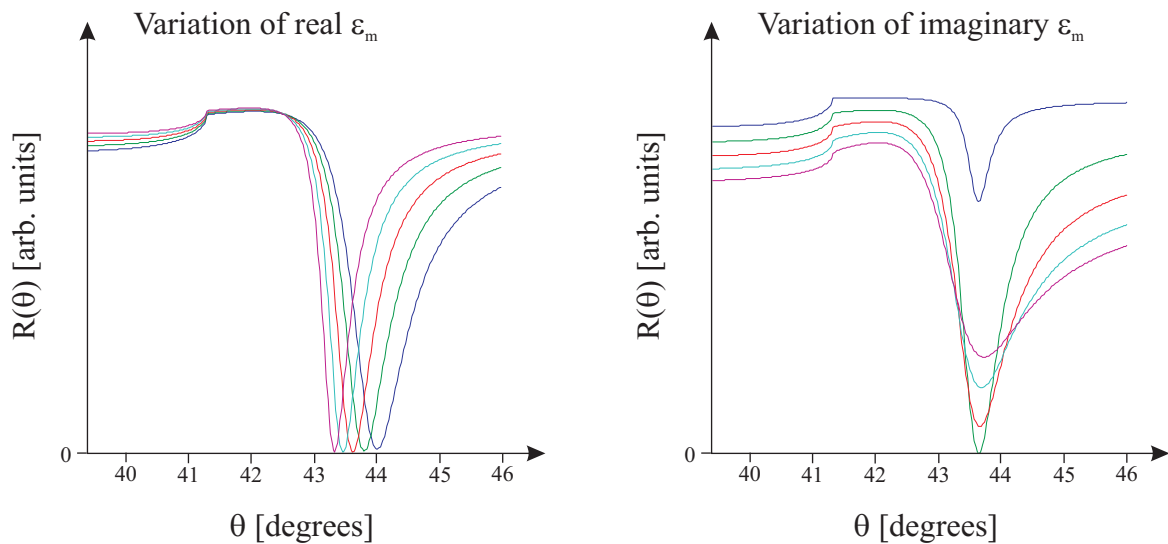


Figure D.4: Reflection curves of various values of the real (left graph) and imaginary (right graph) value of the dielectric constant of the metal. In the left graph the values are decreased from $\epsilon_m = -14 + 1.1i$ (blue) in steps of 1 to $\epsilon_m = -18 + 1.1i$ (purple). The right graph represents increasing dielectric values going from $\epsilon_m = -16 + 0.1i$ (blue) in steps of $1i$ to $\epsilon_m = -16 + 4.1i$ (purple). The remaining parameters are $n_p = 1,5$, $d = 45\text{nm}$ and $\lambda_0 = 632,8\text{nm}$.

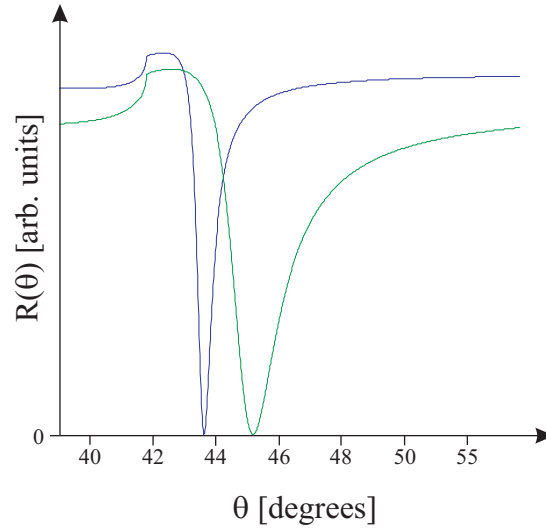


Figure D.5: Reflection curves for silver and gold at optimal thicknesses of 45nm and 53nm respectively. Total ATR of gold occurs at an incident angle of $45,2^\circ$.

considering the expression $\Delta\beta = k \cdot r_{pm}\beta$, which is a simplification of a longer expression provided by [20][page 12], where an increase in ε'_m causes an increase in both the constant k and β . This implies that the incident angle must be increased with increasing β' in order to enhance k_{xp} to the case of resonance given by $(k_{xp} - (\beta + \Delta\beta))^2 = 0$.

The reason to the broadening in both set of graphs in figure D.4 is depicted by considering the fraction term of (D.1). In the case of an increase in ε'_m the term $\beta + \Delta\beta$ becomes more dominant allowing a broader range of k_{xp} values and thereby θ values. A similar explanation is valid for the broadening of the reflection minima due to an increase in the imaginary part of the dielectric constant of the metal, but in this case the term $(\Gamma_i + \Gamma_{back})^2$ is increasingly dominant, since ε''_m is proportional to $\frac{\Gamma_i}{d}$.

Only the green graph in the right window of figure D.4 depicts total ATR, whereas the minima of the remaining are displaced upwards. Total ATR is possible only when the two conditions $\Gamma_i = \Gamma_{back}$ and $d = d_{min}$ are fulfilled. This is explained by the condition $\Gamma_i = \Gamma_{back}$, which occurs at a larger thickness if the ε''_m -value is small, and vice versa.

Reflection Curves for Total ATR

In order to conclude the issues just treated, the reflection curves of samples of silver and gold at the corresponding optimal thicknesses are shown in figure D.5. It is possible to evaluate the value of the half-width of these reflection curves by means of the following: ATR is based on destructive interference between the backscattered and reflected light, each having phase velocities β' and k_{xp} and thereby phase dependencies of $e^{i\beta'x+\pi}$ and $e^{ik_{xp}x}$ respectively. The SPPs are converted into backscattered light at a travelled distance of, on average, $L_{SPP,ATR}$. If the phase change of the backscattered and reflected light is exactly equal, the destructive interference is retained, even at the distance $L_{SPP,ATR}$.

Now suppose there is a small difference in phase velocity of the reflected beam due to a change in the angle of incidence, $\delta\theta$. If the change builds up along the propagation distance, constructive interference could be observed instead. The phase difference in this situation is then 0 expressed as

$$\delta\phi = \beta' 2L_{SPP,ATR} + \pi - k_{xp} 2L_{SPP,ATR} = 0. \quad (\text{D.4})$$

The factor of 2 is present since the interference effect depends on the amplitudes and not the intensities. The propagation length of the SPP in terms of the amplitude is then twice that of the intensity. This is seen by comparing the exponential decay in the expressions of the amplitude and intensity of the H field provided, respectively, by (A.15) and (A.18) on page 64. Since β' can be expressed in terms of $k_{xp} = k_0 n_p \sin \theta_0$ at the angle of total ATR, θ_0 , (D.4) reads

$$(k_0 n_p \sin \theta_0 - k_0 n_p \sin \theta) 2L_{SPP,ATR} = \pi.$$

This may be applied to deduce the value $\delta\theta = (\theta_0 - \theta)$ which is interpreted as the half-width of the reflection minimum

$$\begin{aligned} \delta\theta k_0 n_p \cos \theta &= \frac{\pi}{2L_{SPP,ATR}} \Rightarrow \\ \delta\theta &= \frac{\lambda_0}{4n_p \cos \theta L_{SPP,ATR}} \end{aligned}$$

For silver and gold this gives a values of approximately 0.8° and 2.4° respectively. This corresponds quite well to the half-widths of the reflection curves of figure D.5.

APPENDIX E

REFLECTIVITY FROM A THREE LAYER SYSTEM

The total reflection from a three layer system, such as a prism/metal/air system, is derived by considering the multiple reflections. The situation is sketched in figure E.1. One way to proceed is to consider the total reflection coefficient at the prism-metal interface as a sum of the coefficients of all individual light waves propagating in the prism away from the metal-prism interface. The phase difference between each reflection wave is clearly

$$\Delta\phi = 2k_{zm}d, \quad (\text{E.1})$$

since the path difference in the z-direction is twice the distance of the metal layer. This gives the following for the total reflection coefficient

$$\begin{aligned} r &= r_{pm} + t_{pm}r_{mair}t_{mp}e^{i\Delta\phi} + t_{pm}r_{mair}e^{i\Delta\phi}r_{mp}r_{mair}t_{mp}e^{i\Delta\phi} \\ &\quad + t_{pm}r_{mair}e^{i\Delta\phi}r_{mp}r_{mair}e^{i\Delta\phi}r_{mp}r_{mair}t_{mp}e^{i\Delta\phi} + \dots \\ &= r_{pm} + t_{pm}r_{mair}t_{mp}e^{i\Delta\phi}(1 + r_{mp}r_{mair}e^{i\Delta\phi} + (r_{mp}r_{mair}e^{i\Delta\phi})^2 + \dots). \end{aligned} \quad (\text{E.2})$$

Since $1 + x + x^2 + x^3 + \dots = \frac{1}{1-x}$ for $|x| < 1$, (E.2) is rewritten

$$r = r_{pm} + \frac{t_{pm}r_{mair}t_{mp}e^{i\Delta\phi}}{1 - r_{mp}r_{mair}e^{i\Delta\phi}}.$$

Knowing that $t_{pm}t_{mp} = 1 - r_{pm}^2$ and $r_{mp} = -r_{pm}$, the total reflection coefficient is expressed without the transmission coefficients

$$\begin{aligned} r &= \frac{r_{pm} - r_{pm}r_{mp}r_{mair}e^{i\Delta\phi} + r_{mair}e^{i\Delta\phi} + r_{pm}r_{mp}r_{mair}e^{i\Delta\phi}}{1 - r_{mp}r_{mair}e^{i\Delta\phi}} \\ &= \frac{r_{pm} + r_{mair}e^{i\Delta\phi}}{1 + r_{pm}r_{mair}e^{i\Delta\phi}}, \end{aligned}$$

and the reflectivity is expressed, including (E.1), as

$$R = |r|^2 = \left| \frac{r_{pm} + r_{mair}e^{i2k_{zm}d}}{1 + r_{pm}r_{mair}e^{i2k_{zm}d}} \right|^2.$$

BIBLIOGRAPHY

- [1] Victor Coello. *Elastic Scattering of Surface Plasmon Polaritons*. Institute of Physics (1999). ISBN 87-89195-17-5.
- [2] S. I. Bozhevolnyi, V. S. Volkov, K. Leosson and A. Boltasseva. *Surface plasmon polariton waveguiding in random surface nanostructures*. Journal of Microscopy **209** 209 (2003)
- [3] V. S. Volkov, S. I. Bozhevolnyi, K. Leosson and A. Boltasseva. *Experimental studies of surface plasmon polariton band gap effect*. Journal of Microscopy **210** 324 (2003)
- [4] Sergey I. Bozhevolnyi, Valentyn S. Volkov and K. Leosson. *Localization and waveguiding of surface plasmon polaritons in random nanostructures*. Phys. Rev. Lett. **89** 186801 (2002).
- [5] Katrin Kneipp, Yang Wang, Harald Kneipp, Lev T. Perelman, Irving Itzkan, Ramachandra R. Dasari and Michael S. Feld. *Single molecule detection using surface-enhanced Raman scattering (SERS)*. Phys. Rev. Lett. **78** 1667-1670 (1997).
- [6] William L. Barnes, Alain Dereux and Thomas W. Ebbesen. *Surface plasmon subwavelength optics*. Nature **424** (August 2003).
- [7] Valentyn S. Volkov. *Near-Field Microscopy of Photonic Band Gap Structures*. Institute of Physics (2003). ISBN 3-540-42331-1.
- [8] J. J. Greffet, A. Sentenac and R. Carminati. *Surface profile reconstruction using near field data*. Optics Communications **116** 20 (1995).
- [9] P. Dawson, A. F. Puygranier and J-P. Goudonnet. *Surface plasmon polariton propagation length: A direct comparison using photon scanning tunneling microscopy and attenuated total reflection*. Phys. Rev. B **63** 205410 (2001).
- [10] Sergey I. Bozhevolnyi and Valentyn S. Volkov. *Multiple-scattering dipole approach to modeling of surface plasmon polariton band gap structures*. Optics Communications **198** 241 (2001).
- [11] Marian Rusek and Arkadiusz Orłowski. *Analytical approach to localization of electromagnetic waves in two-dimensional random media*. Phys. Rev. E **51** R2763 (1995)
- [12] Edward D. Palik. *Handbook of Optical Constants of Solids*. Academic Press (1985). ISBN 0125444222.
- [13] F. Pincemin, A. A. Maradudin, A. D. Boardman and J.-J. Greffet. *Scattering of surface plasmon polariton by a surface defect*. Phys. Rev. B **50** 15261 (1994).
- [14] Sergey I. Bozhevolnyi and Victor Coello. *Elastic scattering of surface plasmon polaritons: Modeling and experiment*. Phys. Rev. B **58** 10899 (2002).

-
- [15] Sergey I. Bozhevolnyi and Fedor A. Pudonin. *Two-Dimensional Micro-Optics of Surface Plasmons*. Phys. Rev. Lett. **78** 2823 (1997).
- [16] P. J. Valle, E. M. Ortiz and J. M. Saiz. *Near field by subwavelength particles on metallic substrates with cylindrical plasmon excitation*. Optics Communications **137** 334 (1997).
- [17] A. V. Shchegrov, I. V. Novikov and A. A. Maradudin. *Scattering of Surface Plasmon Polaritons by a Circularly Symmetric Surface Defect*. Phys. Rev. Lett. **78** 4269 (1994).
- [18] H. Ditlbacher, J. R. Krenn, G. Snider, A. Leitner and F. R. Aussenegg. *Two-dimensional optics with surface plasmon polaritons*. App. Phys. Lett. **81** 1762 (2002).
- [19] Charles Kittel. *Introduction to Solid State Physics - Seventh Edition*. John Wiley & Sons (1996). ISBN 0-471-11181-3
- [20] Heinz Raether. *Surface Plasmons*. Springer Verlag (1988). ISBN 0-387-17363-3
- [21] I.S.P. Optics. <http://ispopitics.com/material.html>. Irvington, NY, USA. (december 2003).
- [22] Thomas Søndergaard and Sergey I. Bozhevolnyi. *Vectorial model for multiple scattering by surface nanoparticles via surface polariton-to-polariton interactions*. Phys. Rev. B **67** 165405 (2003).
- [23] Sergey I. Bozhevolnyi. *Student course in near-field optics*. Institute of Physics, Aalborg University, (2003).
- [24] Miles V. Klein and Thomas E. Furtak. *Optics*. John Wiley & Sons, (1986). ISBN 0-471-87297-0.
- [25] Frank L. Pedrotti, S.J. and Leno S. Pedrotti. *Introduction to Optics*. Prentice Hall International, (1993). ISBN 0-13-016973-0.
- [26] Richard Syms and John Cozens. *Optical Guided Waves and Devices*. McGraw-Hill Book Company, (1992). ISBN 0-07-707425-4.
- [27] V. M. Agranovich and D. L. Mills *Surface Polaritons*. North-Holland Publishing Company (1982). ISBN 0-444-86165-3